BIOCIDAL ACTIVITY OF Ag-PEG-CHITOSAN NANOCOMPOSITE FILM PREPARED USING *CANNABIS SATIVA* AQUEOUS LEAF EXTRACT BY SONICATION

Garima Ameta[a]* and Pinki B. Punjabi[a]

Keywords: Biosynthesis, crosslinking, nanocomposite, ultrasound, biocidal activity.

This study underscores the development of Ag-PEG-Ch nanocomposite film using the aqueous leaves extract of *Cannabis sativa* under the influence of ultrasound, as smart substrates for antimicrobial uses, via innovative in situ reactive and reduction pathways. Ag nanoparticles that are synthesized by using leaves extract and ultrasound as an energy source have emerged as nontoxic and ecofriendly. In this study, silver nitrate was used as a silver precursor and PEG and chitosan were used as the polymeric stabilizer and solid support, while cannabis sativa leaves extract acts as a green reducing agent. This polymer metal film was characterized by FT-IR, SEM, TEM, TGA, DSC and antimicrobial activities. XRD peaks clearly reveals that FCC Ag nanoparticles embedded in polymer matrix, very fine Ag nanoparticles (4-6 nm) can be synthesized through ultrasound has been proven by TEM images and TGA-DSC results show that this nanocomposite film is thermally stable. This nanocomposite film possesses synergistic biocidal activities also.

* Corresponding Authors
Tel: +918003180487
E-Mail: garima_ameta@yahoo.co.in
[a] Department of Chemistry, University College of Science, Mohanlal Sukhadia University, Udaipur - 313002 (Raj.) India

INTRODUCTION

Since ancient times, different forms of silver have been used as an antimicrobial agent against infections, before recognizing their nanometric dimension.[1] Chemical and physical factors associated with Ag nanoparticles such as size,[2,3] shape and surface charge[4] enhance their antimicrobial,[5] antibacterial,[6] anti-viral,[7] anti-cancer properties[8] and affect significantly the effective doses to inhibit the growth of microorganism. It is also useful in drug delivery system.[9]

Nevertheless, commercially available silver-based drugs have shown cytotoxic effects on various experimental models.[10,11] So, there is a growing need to develop an eco-friendly process, which does not use toxic chemicals in the synthesis protocols. In a green biosynthesis of nanoparticles, selection of a green reducing and stabilizing agents in an aqueous medium are the most important issues which must be considered. Green biosynthesis approaches include biopolymers, biological molecules, and green irradiation method which have advantages over conventional methods involving hazardous chemical agents. It also enhances the antimicrobial activities of Ag nanoparticles and to overcome the adverse cytotoxic effects of silver.

Polyethylene Glycol (PEG) is a water-soluble polymer and widely used in mechanical, pharmaceutical and cosmetic industries. PEG reduces $AgNO_3$ and stabilizes Ag nanoparticles.[12,13] Stabilization can be obtained due to the free polymer chains in solution, where aggregation is denied because of steric hindrance. PEG is easily permeable through membrane would facilitate the entry of nanoparticles carrying antibiotics across the membrane, enhance the binding of the delivered drug to the bacterial DNA and block drug efflux pumps.[14]

Chitosan is a natural polysaccharide obtained by the deacetylation of chitin.[15] It is a linear polyamine containing number of free amine groups that are readily available for crosslinking. This biopolymer shows unique chelating,[16,17] polycationic,[18] film forming[19] and antimicrobial properties[20] due to the presence of active amino and hydroxyl groups in polymeric matrix. Biocidal activity of chitosan has been studied against yeast,[21] fungi, mold[22,23] and bacteria.[24] Chitosan has significant advantages over others due to its low cytotoxicity towards mammalian cells.[25,26] PEG-Chitosan blend exhibited better physico-chemical properties comparable to chitosan or PEG alone.[27]

Silver nanoparticles have been prepared conventionally by chemical method using reducing agents,[28] which were later responsible for various biological hazards due to their cytotoxic effect. To cure this problem, green synthesis using biological molecule and the use of ultrasound as an energy source[29,30] exhibit superiority over chemical methods. Plant extracts have been demonstrated to be promising reducing and capping agents for the biosynthesis of silver nanoparticles, some of them are *Crocus sativus* L.,[31] *Alpinia katsumadai*,[32] *Kalopanax septemlobus*,[33] *Acalypha indica*,[34] *Citrus limon*,[35] *Alternanthera sessilis*,[36] *Aloe vera*,[37] *Lippia nodiflora*,[38] *Pedalium murex*,[39] etc. *Cannabis sativa* is an herbaceous flowering plant belonging to the family Cannabaceae, native of eastern Asia. The plant is known to contain more than 113 phyto cannabinoids,[40] which have pharmacological importance. It is widely used to treat schizophrenia,[41] neurophatic pain,[42] cancer pain,[43] chemotaxonomic purpose,[44] chronic inflammation,[45] dibetes,[46] multiple sclerosis,[47] as an antipsychotic[48] and analgesic drug.[49] To the best of our knowledge, there has been no report on the green synthesis of nanoparticles using *Cannabis sativa* leaves extract. Therefore, we have synthesized sonochemically and characterized Ag-PEG-Ch nanocomposite film using *Cannabis sativa* leaves extract

as a reducing agent to convert Ag^+ ion to Ag^0 particle. Antimicrobial activities of this synthesized compound have also been studied.

EXPERIMENTAL

PEG, chitosan (Himedia, India), silver nitrate, ethanol and acetic acid (Fisher Scientific, India) were used as received. Ultrasonic cleaner 392 (Systronics, India) was used for ultrasonic irradiation with a frequency of 40 kHz and a nominal power of 115 W.

FTIR spectra were recorded on a FT-IR Spectrometer (Perkin Elmer, India) Spectrum GX Range with a resolution of 0.15 cm^{-1}. Spectra were scanned between 400 and 4000 cm−1. Scan time was 20 scan s^{-1}. XRD pattern measurement [Table Top X-ray Diffraction System (Rigaku Miniflex, USA)] was employed using monochromatic Cu kα radiation (λ = 1.5406 Å) operated at 40 kV and 30 mA at a 2θ angle pattern to study the crystal structures of the nanocomposite. XRD data obtained were compared with the Joint Committee on Powder Diffraction Standards (JCPDS) library to account for the crystalline structure of the nanocomposite.

TEM images for polyethylene glycol-chitosan-silver ternary nanocomposite thin film were recorded using a Philips (Holland), Model: Tecnai 20, transmission electron microscope operating at an acceleration voltage of 200 kV. Electron source are W emitter and LaB6. This instrument uses electron beam optics to achieve very high magnifications of the order of 7,50,000x.

Thermal Analysis (DSC and TGA) – Perkin Elmer (India) Pyris-1 DSC, Pyris-1 TGA was used to analyze nanocomposite thin film. Temperature range for TGA was room temperature to 700ºC and for DSC, it was 40ºC to 400ºC. All observations were carried out under nitrogen atmosphere.

Preparation of *C. sativa* leaves extract

Fresh leaf extract of *C. sativa* was used to reduce Ag^+ ions to Ag^o. Fresh leaves of C. sativa were collected from Dakan Kotra, Girwa, Udaipur. They were cleaned with distilled water and dried at room temperature. About 10 g of finely cut leaves were placed in a beaker containing double distilled water (100 mL) and boiled for 10 min before decanting. Then the extract was cooled down and filtered through Whatman filter paper No.1 and stored at 4 °C for further use.

Synthesis of Ag-PEG-Ch nanocomposite thin film

All the reactions were carried out in an ultrasonic bath. 0.2 g of chitosan was dissolved in 100 mL of 2% aqueous acetic acid and irradiated with ultrasound for 20 min. to obtain clear solution. Reaction of PEG (0.01 M) with silver nitrate (0.01 M, in 5 mL of *C. sativa* aqueous leaf extract) was carried out for 2 h under the influence of ultrasound to give PEG dialdehyde with silver nanoparticles.Change in colour from light yellow to dark brown, indicated the formation of AgNPs. Chitosan solution was added dropwise in ethanol, and then added freshly prepared PEG dialdehyde with silver nanoparticles and few drops of HCl to crosslink the polymer. This solution was washed with DD water and ethanol then centrifuged. Glass slides were cut to 20 mm × 15 mm to fit the spin coater, cleaned by sonication in acetone, and allowed to dry. A total of 0.2 mL of the prepared nanocomposite solution was coated onto the glass slide by spin coating at 500 rpm for 120 s. The resulting films were allowed to dry in vacuum.

Assessment of antimicrobial assay

Synthesized Ag-PEG-Ch nanocomposite using leaves extract of *C. sativa* was analyzed for antimicrobial activity against two Gram positive bacterial strains such as *S. aureus (*MTCC 96) and *S. pyogenus (*MTCC 442), two Gram negative bacterial strains like *E. coli (*MTCC 443) and *P. aeruginosa (*MTCC 1688). Antifungal studies were also carried out on three fungal strains such as *C.albicans (*MTCC 227), *A.niger* (MTCC 282) and *A.clavatus (*MTCC 1323) at Microcare Laboratory, Surat, India.

The minimum inhibitory concentration (MIC) for the sample was evaluated using Broth dilution method to determine the antibacterial and antifungal activity against various bacterial and fungal strains.[50] The bacterial stock cultures were incubated for 24 h at 37 °C in Nutrient Agar media and while the fungal stock cultures were incubated for 72 h at 28 °C in potato dextrose agar media followed by refrigeration storage at 4 °C. The stock cultures were maintained at 4 °C.

RESULTS AND DISCUSSION

FTIR Spectrum of Ag-PEG-Ch thin film shows the combination of the IR absorption characteristic of PEG and chitosan (figure 1). Band appearing at 3429 cm^{-1} is due to the overlapping of O-H and N-H stretching, 2923 cm^{-1} is due to for C-H stretching, bands at 1631 cm^{-1} and 1524 cm^{-1} are due to the N-H bending. A medium band that appears at 1384 cm^{-1}, is a significant band that confirms the formation of metallopolymer (Ag-PEG-Ch).[51]

XRD patterns of Ag-PEG-Chnano composites are shown in figure 2. Two medium peaks appearing at 2θ values of 19.5 and 22.9 are confined to the polymeric chains (chitosan and PEG). The main peaks around 2θ values of 38.4, 44.2, 64.5 and 77.7 with 111, 200,220 and 311diffraction respectively are related to Face Centered Cubic (FCC) crystalline structure of silver in a polymeric matrix, which is supported by the JCPDS file no. 89-3722.. Therefore, this gives clear evidence for the presence of FCC Ag nanoparticles in Ag-PEG-Ch nanocomposite film.

The average particle size of the nanocomposite was calculated by the Debye-Scherrer equation and is estimated to be 6 nm, which clearly demonstrate that finer Ag nanoparticles can be synthesize by the use of ultrasound as compared to those by other methods.[52] In addition, some unassigned peaks might have resulted due to the capping agent stabilising the Ag nanoparticles, which may be due to the bioorganic compounds in a plant extract used.[53,54] These peaks are weaker than the peaks for Ag nanoparticles.

Topographical analysis

Transmission electron microscopy (TEM) studies of Chitosan-PEG-Ag nanocomposites were carried to study the particle size. TEM produces high resolution, black and white images from the interaction between energetic electrons and samples in the vacuum chamber. TEM provides morphological, topographical, compositional and crystalline information. A typical TEM, and histogram image of the nanocomposite is shown in figure 3. TEM image (Figure 3A) shows the dispersed homogeneous particles with diameters of around 13-14 nm. The dark part indicates Chitosan-PEG blend wrapped over Ag nanoparticles. TEM image (Figure 3B) shows the particles size of Ag is around 4-6 nm, which signify the use of ultrasound in the synthesis of nanoparticles over chemical method.[2]

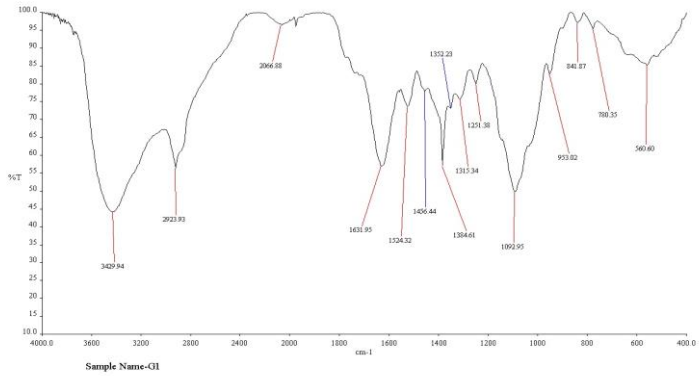

Figure 1. FTIR spectrum of Ag-PEG-Ch nanocomposite film.

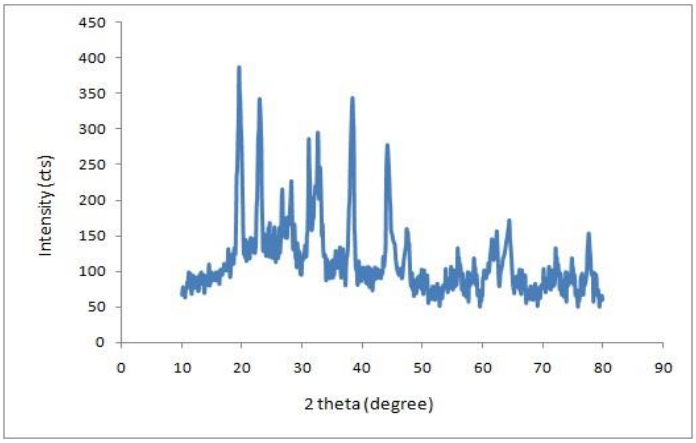

Figure 2. XRD of Ag-PEG-Ch nanocomposite film.

Thermal analysis

The TGA curve recorded the weight loss during heating and the DSC curve describes changes in the reaction enthalpy during the degradation process. The TG thermogram of Ag-PEG-Ch ternary nanocomposite analysis is depicted in Figure 4 A. This nanocomposite exhibits three-stage decomposition process.

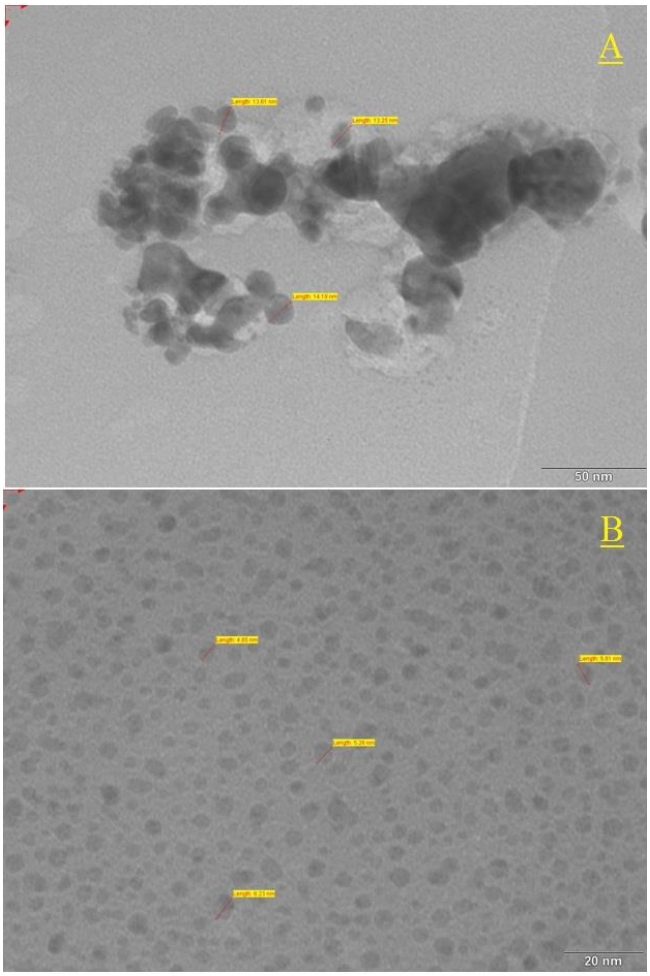

Figure 3. TEM images of Ag-PEG-Ch nanocomposite film.

The first stage (100-450 ^{o}C; weight loss 10.57%) decomposition may be due to expulsion of bound water molecules present in the PEG-Chitosan-Silver ternary nanocomposite. In the second stage, decomposition (451-650 ^{o}C; weight loss 43.34 %) corresponds to the loss of side group elimination attached to the aromatic nucleus, and final stage of decomposition (651-950 ^{o}C; weight loss 15.08 %) is probably due to main chain scission, which ultimately results in depolymerization into aromatic moieties. The ceramic yield of synthesized nanocomposite was found about 31.34 %. The result clearly reveals that PEG-Chitosan-Silver ternary nanocomposite exhibit synergistic effect in thermal stability.[55,56]

By contrast, in the DSC curve, only one thermal event, endothermic, is clearly distinguished up to 510 ^{o}C (Figure 4 B).In broad strokes, these thermal events are related to dehydration and thermal degradation processes, including the depolymerization degree at different stages as well as the secondary decomposition stage of pectin present in nanocomposite. According to the DSC curve, this broad endothermic event at 205.13 ^{o}C (with area swept in endotherm 189.436 mJ and enthalpy change 64.6732 J g^{-1}) can be identified. It is known that the higher melting points of nanocomposite are associated with many factors, including intramolecular interactions through hydrogen-bonded functional linkages and structural regularity and rigidity of macromolecules. This film is water soluble also.

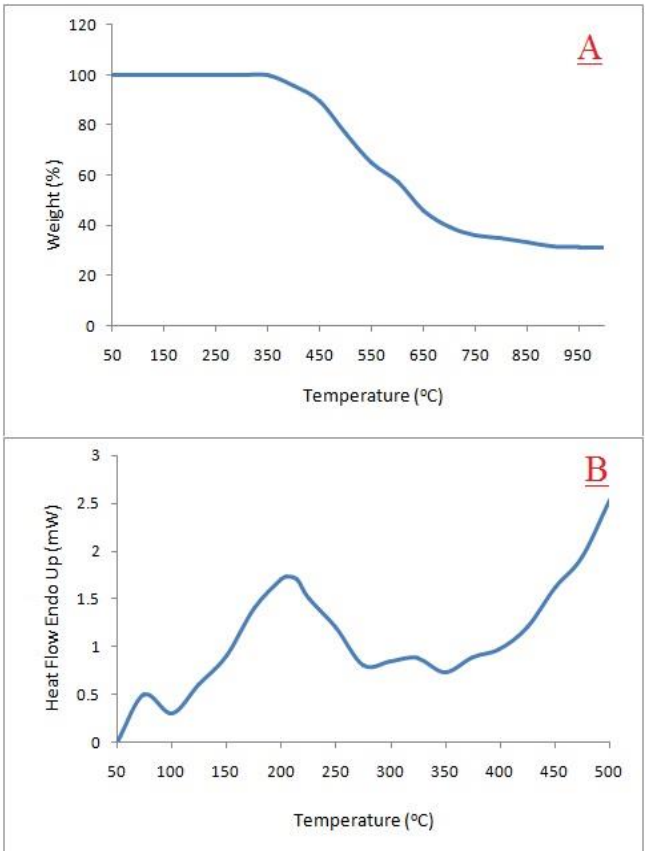

Figure 4 A and B. TGA and DSC curve of PEG-Ch_Ag nanocomposite film, respectively.

Antimicrobial Activities

The antimicrobial activity of Ag-PEG-Ch nanocompositeusing C. sativa leaves extract was studied against four pathogenic bacterial strains, two Gram positive (*S. aureus*MTCC 96 and*S. pyogenus* MTCC 442) and two Gram negative (*E. coli* MTCC 443 and*P. aeruginosa* MTCC 1688) and three fungal strains (*C. albicans* MTCC 227, *A.niger* MTCC 282 and *A.clavatus* MTCC 1323). Antimicrobial activity of the synthesizedAg-PEG-Ch nanocomposite was assessed in terms of minimum inhibitory concentration (MIC).[57] MIC is the lowest concentration of antibiotic in a culture media that will prevent growth. To find MIC, bacteria/fungi were grown on different concentration of antibiotic and obtained a concentration of antibiotic on which bacteria/fungi can grow:The lowest concentration that inhibited the growth of bacteria/fungi was considered as the MIC.The results of antibacterial and antifungal activity of nanocomposite are shown in Fig. 5 and Table 1.

Ag-PEG-Ch nanocomposite using *C. sativa* leaves extract shows most effective antibacterial and antifungal activity as compared to C. sativa leaves extract and Ag nanoparticles alone.

CONCLUSION

This study focuses on the green synthesis of silver nanoparticles without any reducing agent by the use of *cannabis sativa* leaves extract and stabilize them in a polyethylene glycol-chitosan matrix, which are biodegradable polymers. Ultrasound as an energy source has been used in whole process, so this entire process covers the principles of green chemistry. The structure, morphology and thermal stability of the Ag-PEG–Ch were studied by

FTIR, XRD, TEM, TGA and DSC. This supports the strong interaction of PEG with Chitosan molecules, which interferes with its crystalline structure and use of ultrasound in the synthesis of fine Ag nanoparticles (6 nm) with FCC sturcture. C. sativa aqueous leaves extract act as a bioreducing agent to produce silver nanoparticles. Nanocomposite based on chitosan, polyethylene glycol and silver nanoparticles exhibit better thermal stability as compare to Chitosan and PEG alone. This nanocomposite was synergistically active against different bacterial and fungal strains. Therefore, we believe that Ag-PEG-Ch nanocomposite can be used for various biomedical applications.

Table 1. Antibacterial and antifungal activity of Ag-PEG-Ch nanocomposite.

Antibacterial activity					**Antifungal activity**			
Compound	***E.coli***	***P.aeruginosa***	***S.aureus***	***S.pyogenus***	**Compound**	***C.albicans***	***A.niger***	***A.clavatus***
Plant extract	125	100	250	200	Plant extract	500	250	250
Ag nanoparticles	100	75	150	90	Ag nanoparticles	500	90	100
Ag-PEG-Ch*	62	30	60	42	Ag-PEG-Ch*	80	75	80
Ampicillin (μg mL^{-1})	100		250	100	Greseofulvin (μg mL^{-1})	500	100	100
Ciprofloxacin (μg mL^{-1})	25	25	50	50	Nystatin (μg mL^{-1})	100	100	100

*Ag-PEG-Ch nanocomposite in plant extract

REFERENCES

[1]Nowack, B., Krug, H. F., Height, M., 120 Years of Nanosilver History: Implications for Policy Makers, *Environ. Sci. Technol.*, **2011**, *45*, 1177-1183. DOI: 10.1021/es103316q

[2]Agnihotri, S., Mukherji, S., Mukherji, S., Size-controlled silver nanoparticles synthesized over the range 5–100 nm using the same protocol and their antibacterial efficacy, *RSC Adv.*, **2014**, *4*, 3974-3983. DOI: 10.1039/C3RA44507K

[3]Ayala-Núñez, N. V., Villegas, H. H. L., Turrent, Ld. C. I., Padilla, C. R., Silver Nanoparticles Toxicity and Bactericidal Effect Against Methicillin-Resistant *Staphylococcus aureus*: Nanoscale Does Matter, *Nanobiotech.*, **2009**, *5*, 2-9. DOI https://doi.org/10.1007/s12030-009-9029-1

[4]Abbaszadegan, A., Ghahramani, Y., Gholami, A., Hemmateenejad, B., Dorostkar, S., Nabavizadeh, M., Sharghi, H., The Effect of Charge at the Surface of Silver Nanoparticles on Antimicrobial Activity against Gram-Positive and Gram-Negative Bacteria: A Preliminary Study, *J. Nanomater.*, **2015**, 8 pages. ID 720654 http://dx.doi.org/10.1155/2015/720654

[5]Guo, Q., Zhao, Y., Dai, X., Zhang, T., Yu, Y., Zhang, X., Li, C., Functional Silver Nanocomposites as Broad-Spectrum Antimicrobial and Biofilm-Disrupting Agents, *ACS Appl. Mater. Interfaces*, **2017**, *9*, 16834-16847. DOI: 10.1021/acsami.7b02775

[6]Bandla, M., Abbavaram, B. R., Kokkarachedu, V., Sadiku, R. E., Silver nanoparticles incorporated within intercalated clay/polymer nanocomposite hydrogels for antibacterial studies, *Polym. Compos.*, **2017**, *38*, E16-E23. https://doi.org/10.1002/pc.23963

[7]Castro-Mayorgaa J. L., Randazzo, W., Fabra, M. J., Lagaron, J. M., Aznar, R., Sánchez, G., Antiviral properties of silver nanoparticles against norovirus surrogates and their efficacy in coated polyhydroxyalkanoates systems, *LWT - Food Sci. Tech.*, **2017**, *79*, 503-510. https://doi.org/10.1016/j.lwt.2017.01.065

[8]Salahuddin, N., Elbarbary, A. A., Alkabes, H. A., Antibacterial and anticancer activity of loaded quinazolinone polypyrrole/chitosan silver chloride nanocomposite, *Int. J. Polym. Mater. Polym. Biomater*, **2017**, *66*, 307-316. https://doi.org/10.1080/00914037.2016.1201831

[9]Benyettou, F., Rezgui, R., Ravaux, F., Jaber, T., Blumer, K., Jouiad, M., Motte, L., Olsen, J.-C., Platas-Iglesias, C., Magzoub, M., Trabolsi, A., Synthesis of silver nanoparticles for the dual delivery of doxorubicin and alendronate to cancer cells, *J. Mater. Chem. B*, **2015**, *3*, 7237-7245. DOI: 10.1039/C5TB00994D

[10]Prabhu, S., Poulose, E. K., Silver nanoparticles: mechanism of antimicrobial action, synthesis, medical applications, and toxicity effects, *Int. Nano Lett.*, **2012**, *2*, 1-10. doi: 10.1186/2228-5326-2-32

[11]Burd, A., Kwok, C. H., Hung, S.C., Chan, H. S., Gu, H., Lam, W. K., Huang, L., A comparative study of the cytotoxicity of silver-based dressings in monolayer cell, tissue explant, and animal models, *Wound Repair Regen.*, **2007**, *15*, 94-104. DOI:10.1111/j.1524-475X.2006.00190.x

[12]Liang, W., Wang, L., Zhu, Z., Qian, C., Sun, H., Yang, B., Li, A., In Situ Preparation of Polyethylene Glycol/ Silver Nanoparticles Composite Phase Change Materials with Enhanced Thermal Conductivity, *Chem. Select*, **2017**, *2*, 3428-3436. https://doi.org/10.1002/slct.201700381

[13]Fahmy, A., El-Zomrawy, A., Saeed, A. M., Sayed, A. Z., El-Arab, M. A. E., Shehata, H. A., One-step synthesis of silver nanoparticles embedded with polyethylene glycol as thin films, *J. Adhesion Sci. Tech.*, **2017**, 31, 1422-1440. https://doi.org/10.1080/01694243.2016.1259728

[14]Marslin, G., Revina, A. M., Khandelwal, V. K. M., Balakumar, K., Sheeba, C. J., Franklin, G., PEGylated ofloxacin nanoparticles render strong antibacterial activity against many clinically important human pathogens, *Coll. Surf. B: Biointerface*, **2015**, *132*, 62-70. DOI:10.1016/j.colsurfb.2015.04.050

[15]Guibal, E., Cambe, S., Bayle, S., Taulemesse, J.-M., Vincent, T., **Silver/chitosan/cellulose fibers foam composites: from synthesis to antibacterial properties,** *J. Coll. Interface Sci.*, **2013**, *393*, 411-420. DOI: 10.1016/j.jcis.2012.10.057

[16]Carpio-Perochena, A.-d., Bramante, C. M., Duarte, M. A. H., de Moura, M. R., Aouada, F. A., Kishen, A., Chelating and antibacterial properties of chitosan nanoparticles on dentin, *Restor. Dent. Endod.*, **2015**, *40*, 195-201. DOI:10.5395/rde.2015.40.3.195

[17]Budnyak, T. M., Pylypchuk, I. V., Tertykh, V. A., Yanovska, E. S., Kolodynska, D., Synthesis and adsorption properties of chitosan-silica nanocomposite prepared by sol-gel method, *Nanoscale Res. Lett.*, **2015**, *10*, 87. DOI https://doi.org/10.1186/s11671-014-0722-1

[18]Dragan, E. S., Cocarta, A. I., Composite Beads Based on Chitosan and a Synthetic Polycation with Sorption Properties Modulated by the Cross-Linking Strategy, *Macromol. Symp.*, **2015**, *352*, 33-37. https://doi.org/10.1002/masy.201400146

[19]Souza, V. G. L., Fernando, A. L., Afonso, Pires, J. R., Rodrigues, P. F., Lopes, A. A. S., Fernandes, F. M. B., Physical properties of chitosan films incorporated with natural antioxidants, *Ind. Crops Prod.*, **2017**, *107*, 565-572. https://doi.org/10.1016/j.indcrop.2017.04.056

[20]Kalaycıoğlu, Z., Torlak, E., Akın-Evingür, G., Özen, İ., Erim, F. B., Antimicrobial and physical properties of chitosan films incorporated with turmeric extract, *Int. J. Biol. Macromol.*, **2017**, *101*, 882-888. DOI: 10.1016/j.ijbiomac.2017.03.174

[21]Kiskó, G., Sharp, R., Roller, S., Chitosan inactivates spoilage yeasts but enhances survival of Escherichia coliO157:H7 in apple juice, *J. Appl. Microbiol.*, **2005**, *98*, 872-880. doi:10.1111/j.1365-2672.2004.02527.

[22]Nehra, P., Chauhan, R. P., Garg, N., Verma, K., Antibacterial and antifungal activity of chitosan coated iron oxide nanoparticles, *Brit. J. Biomed. Sci.*, **2018**, *75*, 13-18. DOI:10.1080/09674845.2017.1347362

[23]Sudarshan, N. R., Hoover, D. G., Knorr, D., Antibacterial action of chitosan, *Food Biotechnol.*, **1992**, *6*, 257-272. https://doi.org/10.1080/08905439209549838

[24]Manukumar, H. M., Umesha, S., Kumar, H. N. N., Promising biocidal activity of thymol loaded chitosan silver nanoparticles (T-C@AgNPs) as anti-infective agents against perilous pathogens, *Int. J. Biol. Macromol.*, **2017**, *102*, 1257-1265. DOI:10.1016/j.ijbiomac.2017.05.030

[25]Liu, X. F., Guan, Y. L., Yang, D. Z., Li, Z., Yao, K. D., Antibacterial action of chitosan and carboxymethylated chitosan, *J. Appl. Polym. Sci.*, **2001**, *79*, 1324-1335. https://doi.org/10.1002/1097-4628(20010214)79:7<1324::AID-APP210>3.0.CO;2-L

[26]Rabea, E. I., Badawy, M. E. T., Stevens, C. V., Smagghe, G., Steurbaut, W., Chitosan as Antimicrobial Agent: Applications and Mode of Action, *Biomacromol.*, **2003**, *4*, 1457-1465. DOI: 10.1021/bm034130m

[27]Li, X., Kong, X., Shi, S., Gu, Y., Yang, L., Guo, G., Luo, F., Zhao, X., Wei, Y., Qian, Z., Biodegradable MPEG-g-Chitosan and methoxy poly(ethylene glycol)-b-poly(ε-caprolactone) composite films: Part 1. Preparation and characterization, *Carbohyd. Polym.*, **2010**, *79*, 429-436. https://doi.org/10.1016/j.carbpol.2009.08.032

[28]Shameli, K., Ahmad, M. B., Zargar, M, Yunus, W. M. Z. W., Ibrahim, N. A., Shabanzadeh, P., Moghaddam, M. G., *Int. J. Nanomed.*, **2011**, *6*, 271-284.

[29]Freire, T. M., Dutra, L. M. U., Queiroz, D. C., Ricardo, N. M. P. S., Barreto, K., Denardin, J. C., Wurm, F. R., Sousa, C. P., Correia, A. N., Lima-Neto, P., Fechine, P. B. A., Fast ultrasound assisted synthesis of chitosan-based magnetite nanocomposites as a modified electrode sensor, *Carbohyd. Polym.*, **2016**, *151*, 760-769. DOI: 10.1016/j.carbpol.2016.05.095

[30]Vinoth, V., Wu, J. J., Asiri, A. M., Anandan, S., Sonochemical synthesis of silver nanoparticles anchored reduced graphene oxide nanosheets for selective and sensitive detection of glutathione, *Ultrason. Sonochem.*, **2017**, *39*, 363-373. DOI:10.1016/j.ultsonch.2017.04.035

[31]Bagherzade, G., Tavakoli, M. M., Namaei, M. H., Green synthesis of silver nanoparticles using aqueous extract of saffron (*Crocus sativus* L.) wastages and its antibacterial activity against six bacteria, *Asian Pac. J. Trop. Biomed.*, **2017**, *7*, 227-233. https://doi.org/10.1016/j.apjtb.2016.12.014

[32]He, Y., Wei, F., Ma, Z., Zhang, H., Yang, Q., Yao, B., Huang, Z., Li, J., Zeng, C., Zhang, Q., Green synthesis of silver nanoparticles using seed extract of *Alpinia katsumadai*, and their antioxidant, cytotoxicity, and antibacterial activities, *RSC Adv.*, **2017**, *7*, 39842-39851. DOI: 10.1039/C7RA05286C

[33]Salunke, B. K., Sawant, S. S., Kim, B. S., Potential of Kalopanax septemlobus leaf extract in synthesis of silver nanoparticles for selective inhibition of specific bacterial strain in mixed culture, *Appl. Biochem. Biotechnol.*, **2014**, *174*, 587-601. DOI:10.1007/s12010-014-1077-x

[34]Krishnaraj, C., Jagan, E. G., Rajasekar, S., Selvakumar, P., Kalaichelvan, P. T., Mohan, N., Synthesis of silver nanoparticles using Acalypha indica leaf extracts and its antibacterial activity against water borne pathogens, *Colloid Surf. B*, **2010**, *76*, 50-56. DOI:10.1016/j.colsurfb.2009.10.008

[35]Prathna, T. C., Chandrasekaran, N., Raichur, A. M., Mukherjee, A., Biomimetic synthesis of silver nanoparticles by Citrus limon (lemon) aqueous extract and theoretical prediction of particle size, *Colloids Surf. B*, **2011**, *82*, 152-159. DOI:10.1016/j.colsurfb.2010.08.036

[36]Niraimathi, K. L., Sudha, V., Lavanya, R., Brindha, P., Biosynthesis of silver nanoparticles using Alternanthera sessilis (Linn.) extract and their antimicrobial, antioxidant activities, *Coll. Surf. B*, **2013**, *102*, 288-291. DOI:10.1016/j.colsurfb.2012.08.041

[37]Medda, S., Hajra, A., Dey, U., Bose, P., Mondal, N. K., Biosynthesis of silver nanoparticles from *Aloe vera* leaf extract and antifungal activity against *Rhizopus* sp. and *Aspergillus* sp., *Appl. Nanosci.*, **2015**, *5*, 875-880. https://doi.org/10.1007/s13204-014-0387-1

[38]Johnson, I., Prabu, H. J., Green synthesis and characterization of silver nanoparticles by leaf extracts of *Cycas circinalis*, *Ficus amplissima*, *Commelina benghalensis* and *Lippia nodiflora*, *Int. Nano. Lett.*, **2015**, 5, 43-51. https://doi.org/10.1007/s40089-014-0136-1

[39]Anandalakshmi, K., Venugobal, J., Ramasamy, V., Characterization of silver nanoparticles by green synthesis method using *Pedalium murex* leaf extract and their antibacterial activity, *Appl. Nanosci.*, **2016**, *6*, 399-408. DOI https://doi.org/10.1007/s13204-015-0449-z

[40]Izzo, A. A., Borrelli, F., Capasso, R., Di Marzo, V., Mechoulam, R., Non-psychotropic plant cannabinoids: new therapeutic opportunities from an ancient herb., *Trends Pharmacol. Sci.*, **2009**, *30*, 515-527. DOI: 10.1016/j.tips.2009.07.006

[41]Ranganathan, M., D'souza, D. C., The acute effects of cannabinoids on memory in humans: a review, *Psychopharmacology*, **2006**, *188*, 425-444. DOI:10.1007/s00213-006-0508-y

[42]Ożarowski, M., Mikolajczak, P. Ł., Bogacz, A., Bartkowiak-Wieczorek, J., Kujawski, R., Majchrzycki, M., Wielgus, K., Seremak-Mrozikiewicz, A., Czerny, B., Progress in study of Cannabis sativa leaves extracts without psychotropic cannabinoids in animal model of neuropathic pain, *J. Med. Sci.*, **2014**, *83*, 328-335.

[43]Hazekamp, A., Grotenhermen, F., Review on clinical studies with cannabis and cannabinoids, *Cannabinoids*, **2010**, 5, 1-21.

[44]Fischedick, J. T., Hazekamp, A., Erkelens, T., Choi, Y. H., Verpoorte, R., Metabolic fingerprinting of Cannabis sativa L., cannabinoids and terpenoids for chemotaxonomic and drug standardization purposes**,** *Phytochem.*, **2010**, *71*, 2058-2073. DOI: 10.1016/j.phytochem.2010.10.001

[45]Costa, B., Trovato, A. E., Comelli, F., Giagnoni, G., Colleoni, M., The non-psychoactive cannabis constituent cannabidiol is an orally effective therapeutic agent in rat chronic inflammatory and neuropathic pain, *Eur. J. Pharmacol.*, **2007**, 556, 75-83. DOI:10.1016/j.ejphar.2006.11.006

[46]Weiss, L., Zeira, M., Reich, S., Har-Noy, M., Mechoulam, R., Slavin, S., Gallily, R., Cannabidiol lowers incidence of diabetes in non-obese diabetic mice, *Autoimmunity*, **2006**, *39*, 143-151. DOI:10.1080/08916930500356674

[47]Zajicek, J. P., Apostu, V., Role of cannabinoids in multiple sclerosis, *CNS Drugs*, **2011**, 25, 187-201. DOI:10.2165/11539000-000000000-00000

[48]Zuardi, A. W., Crippa, J. A. S., Hallak, J. E. C., Moreira, F. A., Guimarães, F. S., Cannabidiol, a Cannabis sativa constituent, as an antipsychotic drug, *Braz. J. Med. Biol. Res.*, **2006**, *39*, 421-429. DOI:/S0100-879X2006000400001

[49]Klauke, A. L., Racz, I., Pradier, B., Markert, A., Zimmera, A. M., Gertsch, J., Zimmer, A., *E* The cannabinoid CB_2 receptor-selective phytocannabinoid beta-caryophyllene exerts analgesic effects in mouse models of inflammatory and neuropathic pain, *Eur. Neuropsychopharmacol.*, **2014**, *24*, 608-620. DOI: 10.1016/j.euroneuro.2013.10.008

[50]Wayne, P. A., *Clinical and Laboratory Standard Institute (CLSI) Performance Standards for Antimicrobial Susceptibility Testing; Twenty-Third Informational Supplement CLSI Document*, **2013**, M100-S23.

[51]Ahmad, M. B., Tay, M. Y., Shameli, K., Hussein, M. Z., Lim, J. J., Green Synthesis and Characterization of Silver/Chitosan/Polyethylene Glycol Nanocomposites without any Reducing Agent, *Int. J. Mol. Sci.*, **2011**, *12*, 4872-4884. https://doi.org/10.3390/ijms12084872

Received: 16.10.2018.
Accepted: 03.11.2018.

SYNTHESIS OF SOME NEW HETEROARYLBISAZO DYES DERIVED FROM p-AMINOAZOBENZENE

Taha A. Ameen[a,b] * and A.A. Fadda[c]

Keywords: : *p*-Aminoazobenzene, malononitrile, acetylacetone, pyrazolo[1,5-*a*]pyrimidine, hydroxyl amine.

Several novel arylbisazopyrazolo[1,5-*a*]pyrimidines were synthesized from diazotization of 4-aminoazobenzene and coupling with malononitrile and then refluxed with hydrazine hydrate to give 3,5-diamino-4-arylbisazo-1*H*-pyrazole.The later compound was diazotized and coupled with bifunctional reagents to produce novel heteroarylbisazo dyestuffs. Structural characterization of these novel dyes was carried out using IR, ^{1}H NMR, and mass spectroscopy.

* Corresponding Authors
Fax:
E-Mail: drtaha7447@yahoo.com
[a] Chemistry Department, Faculty of Science, Zagazig University, Zagazig, Egypt
[b] Chemistry Department, Faculty of Science, Jazan, University,jazan, Saudi Arabia
[c] Chemistry Department, Faculty of Science, Mansoura University, Mansoura, Egypt

Introduction

It has been known for many years that the azo compounds are the most widely used class of dyes due to their versatile applications in various fields such as dyeing of textile fibers, coloring of different materials, biological medical studies and advanced applications in organic synthesis.[1,2] Azo dyes with heterocyclic diazo components have been intensively investigated to produce bright and strong colour shades ranging from red to greenish blue on synthetic fabrics.[3,4]

5-Aminopyrazoles are very important class of heterocycles due to their biological and pharmacological activities.[5,6] These compounds often exhibit anti-inflammatory, herbicidal, fungicidal, bactericidal, and antipyretic activities.[6-12] The aminopyrazole compounds have been easily obtained by the reaction of nitrile derivatives with hydrazine, and are very useful as precursors for the synthesis of fused heterocyclic ring systems.[13,14] Reactions of aminopyrazoles with electrophilic reagents give rise to various fused annulated heterocyclic systems, including pyrazolo[1,5-*a*]pyrimidines which are synthetic analogs of purines. These compounds exhibit a wide spectrum of biological activity, in particular enzymatic, antibacterial, antiphlogistic and antiparasitic activities.[15,16] They are also used as intermediates in the dyestuff industry.[17-19]

In continuation of these studies, we report here the synthesis of some new bisazopyrazolo[1,5-*a*]pyrimidine, pyridazin, isoxazol, and 1,3,5-triazine thione dyes starting with *p*-aminoazobenzene.

Results and Discussion

The dye intermediate 2-[4-phenylazo-phenylhydrazono]-malononitrile (**1**) was prepared by the general route[20] involving diazotization of the *p*-aminoazobenzene and coupling of its diazonium salt with malononitrile. 2-[4-Phenylazo-phenylhydrazono]- malononitrile (**1**) was reacted with hydrazine hydrate and phenyl hydrazine yielding the corresponding pyrazole derivatives (**2a, b**) (Scheme 1).

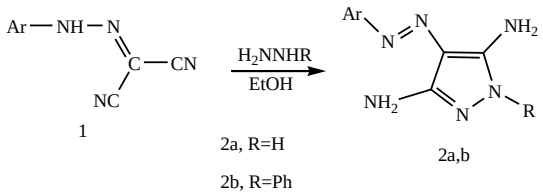

Scheme 1. Synthesis of pyrazole derivatives.

The treatment of compound **2a** with benzoyl isothiocyanate furnished the pyrazol-5-yl-thiourea (**3**). Compound **3** was converted into pyrazolo[3,4-e]as-triazines (**4**) on treatment with acetic acid- hydrochloric acid mixture. Structures of both **3** and **4** were proposed for this reaction product on the basis of analytical and spectral data. Moreover, the reaction of **2a** with acrylonitrile was investigated as a possible route for the synthesis of pyrazolo[1,5-*a*]pyrimidines. Compound **2a,** treated with acrylonitrile in boiling pyridine, afforded directly the iminopyrazolo[1,5-*a*]pyrimidine (**6**) and not the cyano ethylation product (**5**). Compound **6** could be readily converted to the corresponding 5-ketopyrazolo[1,5-*a*]pyrimidine derivative (**7**) by refluxing it in a mixture of acetic acid–hydrochloric acid or by heating with conc. sulfuric acid. On the other hand, the reaction of compound **2a** with ethyl acetoacetate afforded the condensation product **9** not **8**. The *m/z* fragmentation showed the base beak at 360 (M^+-72) due to the cleavage of amide bond The first step of the mechanism involves the condensation of the NH group of the pyrazole ring with the carbonyl group, followed by dehydration, subsequent nucleophilic cyclization, with the loss of ethanol molecule.

Similarly, compound **2a** reacted with acetylacetone to furnish pyrazolo[1,5-*a*]pyrimidine derivative (**10**), which was confirmed from analytical and spectral data. In a similar manner, aminopyrazole **2a** also reacted with 2-[4-phenylazo-phenylhydrazono]-malononitrile **1** in boiling DMF to furnish pyrazolo[1,5-*a*]pyrimidine (**11**). The ^{1}H NMR spectrum of structure **11** showed three singlets at δ = 2.75, 2.85 and 6.92 ppm corresponding to the three NH_2 groups. IR spectrum showed peaks at 3411, 3275 and 3150 cm^{-1} for the NH_2 and MS (*m/z* 581, M^+) (Scheme 2).

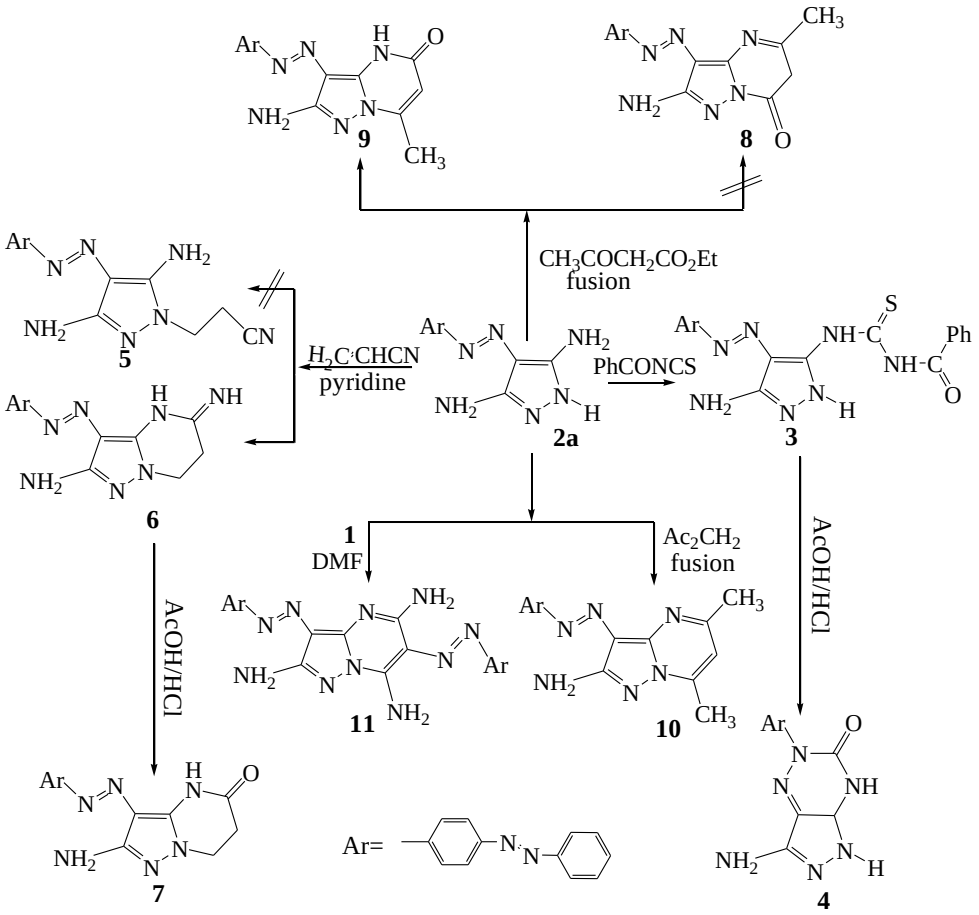

Scheme 2. Reactions of compound (**2a**).

Compound **1** reacted with malononitrile to yield compound **12**. The analytical and spectral data confirmed that the reaction product was compound **12** not **13**. In order to establish the structure of compound **12**, 2-amino-1,1,3-tricyanopropene was coupled with the diazonium salt of *p*-aminoazobezene to afford a product which was considered to have the structure of compound **13**. When compound **13** was boiled for a short period of time in DMF, a product was obtained that was identical in all respects with the product of the reaction of compound **1** with malononitrile, thus establishing structure **12** for the latter product.[21] The IR spectrum of compound **12** revealed a broad CN absorption in the region 2180–2200 cm^{-1}. This large frequency shift may be attributed to the presence of amino and imino groups adjacent to the cyano function. Baldwin and co-workers[22] reported CN absorption for o-aminonitriles in the range 2160–2200 cm^{-1} (Scheme 3).

Compound **14** was synthesized via coupling of cyanoacethydrazide with the diazonium salt of p-aminoazobezene. Compound **14** reacted with hydroxylamine hydrochloride in cold in the presence of sodium acetate to afford 3-amino-4-[4-phenylazophenylhydrazono]-2-isoxazolin-5-one (**15**). The cyano group of compound **14** was condensed with malononitrile in refluxing DMF to yield a product which was considered to have the structure of compound **16**. Structures **14-16** were established on the basis of analytical and spectral data (Scheme 4).

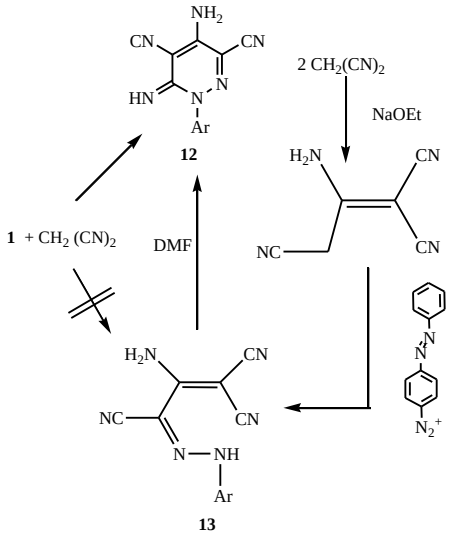

Scheme 3. Synthesis of compounds (**12**) and (**13**).

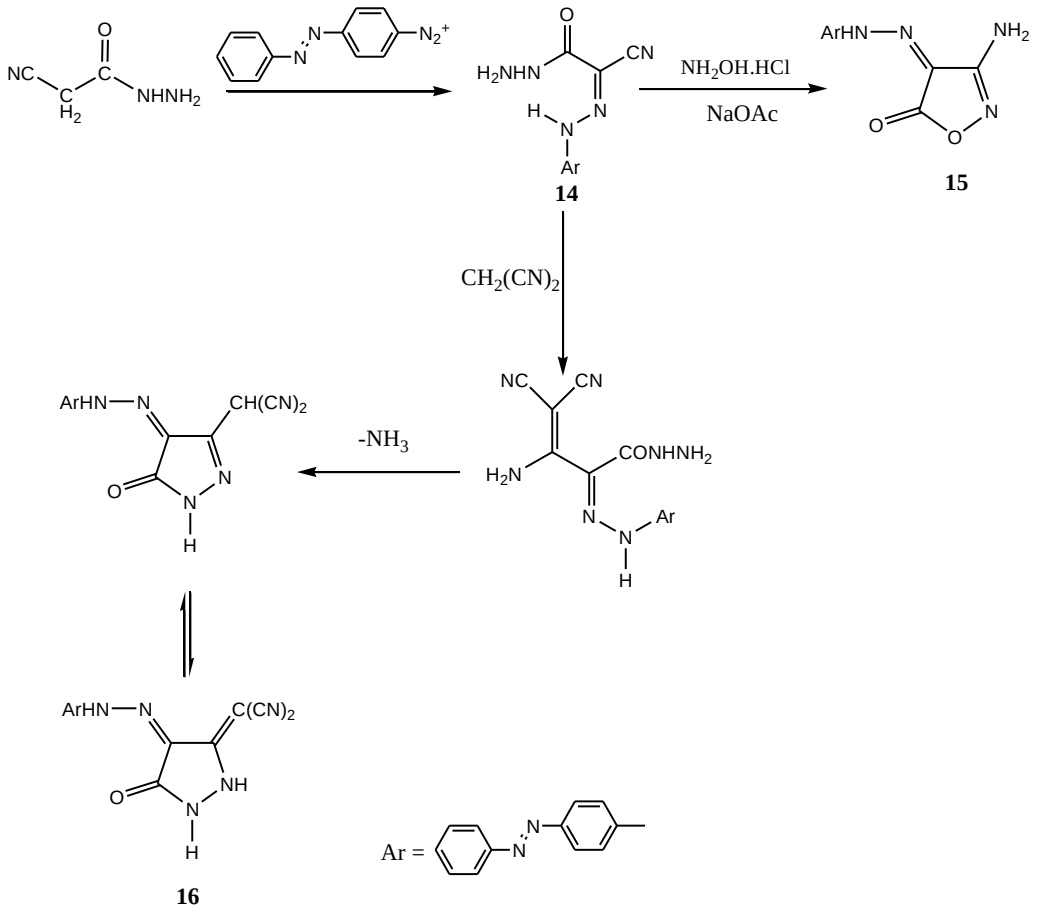

Scheme 4. Synthesis of compounds (**14**) – (**16**).

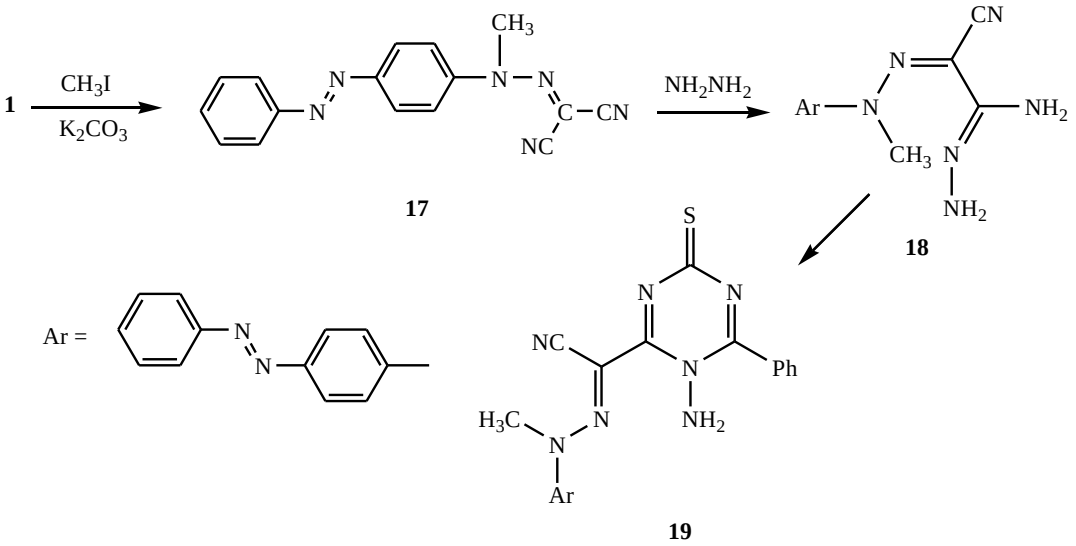

Scheme 5. Synthesis of compounds (**18**) and (**19**).

Compound **18** could be obtained via the action of hydrazine hydrate on N-methylphenylazo-phenylhydrazono-malononitrile (**17**), the latter was synthesized via the action of methyl iodide on **1**. The IR spectra of compound **18** showed the strong absorption band at3440-3340 $cm^{-1}$for the amino group (NH_2), at 2210 cm^{-1} for the cyano group (CN), and 1600 cm^{-1} for (N=N). ^1H NMR spectrum of structure **18** revealed a singlet at δ 3.8 (s, 3H) assigned to methyl group, and (s, 4H) assigned for the 2-amino groups, and at δ 7.1-7.7, (m, 9H) for aromatic protons. The reaction of comound **18** with benzoyl isothiocynate, in refluxing acetone gives the corresponding aminotriazine derivative **19**. The IR spectra of compound **19** showed the strong absorption band at 3190-3000 $cm^{-1}$for the amino group (NH_2), at 2200 cm^{-1} for the cyano group (CN) and MS (*m/z* 420, M^+-45) (Scheme 5).

Experimental

General

All melting points were determined using Gallenkamp electric melting point apparatus and were uncorrected. The IR spectra cm^{-1} (KBr) were recorded on Perkin Elmer Infrared Spectrophotometer Model 157, Grating. The ^1H NMR spectra were recordedon a Varian Spectrophotometer at 200 MHz. using DMSO as a solvent and TMS as internal standard (chemical shift in δppm). The mass spectra (EI) and purity were recorded on 70 eV with Kratos MS equipment and/or a Varian MAT 311 ASpectrometer. The chemicals used were of laboratory grade.

Synthesis of the dyes

2-(4-Phenylazophenylhydrazono)malononitrile (1).

To a solution of malononitrile (6.606 g, 0.1 mol) in ethanol (100 mL), 5.0 g of anhydrous sodium acetate was added. The solution was then treated with diazonium salt of *p*-aminoazobenzene (prepared from p-aminoazobenzene (19.724 g, 0.1 mol) and the appropriate quantities of acetic acid and sodium nitrite). The reaction mixture was stirred for 1 h and the resulting solid was filtered off, washed with H_2O and recrystallized from ethanol. Yield 80 %, m.p. 155 ºC. IR (KBr/m) 3100 (NH), 2220 (conjugated CN), 1620 (C=N) and 1600, 1590 (N=N) cm^{-1}. Anal. Calcd for $C_{15}H_{10}N_6$ (274.28): C, 65.7; H, 3.70; N, 30.6. Found: C, 65.2; H, 4.00; N, 30.5.

3,5-Diamino-4-(4-phenylazophenylazo)-1H-pyrazole (2).

A mixture of **1** (2.743 g, 0.01 mol) and hydrazine hydrate 98 % (0.501 g, 0.01 mol) was heated on a boiling water bath for 1 h. The reaction mixture was then triturated with ethanol and the resulting solid product was filtered off and recrystallized from acetic acid. Yield 90 %, m.p. 245 ºC. IR (KBr/m) 3350–3380 (NH_2), 3280 (NH) and 1600–1550 (N=N) cm^{-1}. MS *m/z* 307 (M^+), 306, 201, 156, 125 and 91. Anal. Calcd for $C_{15}H_{14}N_8$ (306.33): C, 58.8; H, 4.60; N, 36.9. Found: C, 59.0; H, 4.8; N, 37.0.

3,5-diamino-4-(4-phenylazophenylazo)pyrazol-3-yl-benzoylthiourea(3)

To a solution of benzoyl isothiocyanate in acetone (50 mL), **(2)** (30.63 g, 0.1 mol) was added. The reaction mixture was refluxed for 2 h and then poured into water, the resulting solid product was filtered off and recrystallized from ethanol. Yield 70 %, M.p. 190 ºC. IR (KBr/m) 3350–3380 (NH2), 3280, 3330 (NH), 1680 (CO) and 1300 (C=S) cm^{-1}. ^1H NMR (DMSO, 200 MHz) δ = 5.1 (s,2H, NH2), 7.3–8.0 (m, 14H, Ar-H), 8.4 (s, 1H, NH), 9.0 (s, 1H, NH) and 9.3 (s, 1H, NH). Anal. Calcd for $C_{23}H_{19}N_9$ (421.4): C, 65.7; H,4.50; N, 29.9. Found: C, 65.4; H, 4.0; N, 29.8.

7-Amino-2-(4-phenylazophenylazo)-2,3-dihydro-3-oxo-4H-pyrazolo[3,4-*e*]-*as*-triazine (4)

To a suspension of **3** (4.695 g, 0.01 mol) in acetic acid (20 mL), concentrated HCl (2 mL) was added. The reaction mixture was refluxed for 30 min., and then poured into water. The solid product was collected by filtration and crystallization from acetic acid. Yield 60 %, m.p. 175 ºC. IR (KBr/m) 3450 (NH_2), 3320 (NH), 1700 (CO) and 1600 (N=N) cm^{-1}. ^1H NMR (DMSO, 200 MHz) δ = 5.2 (s, 2H, NH_2), 7.3–8.0 (m, 9H, Ar-H) and 9.0 (s, 1H, NH). MS *m/z* 335 (M+), 329, 323, 271, 237, 208, 167 and 57. Anal. Calcd for $C_{16}H_{13}N_8O$ (333.33): C, 57.8; H, 3.90; N, 33.7. Found: C, 58.0; H, 3.4; N, 33.8.

2-Amino-5-imino-4,5,6,7-tetrahydro-3-(4-phenylazophenylazo)-pyrazolo[1,5-*a*]pyrimidine (6)

A solution of **2a** (30.63 g, 0.1 mol), in pyridine (40 mL) and water (10 mL), was treated with ethyl acrylate (10.01 g, 0.1 mol). The mixture was refluxed for 4 h. The reaction mixture was then poured into water and the solid product was collected by filtration and recrystallized from ethanol. Yield 90 %, m.p. 240 ºC. IR (KBr/m) 3390– 3330 (NH_2), 3120 (NH) and 1600 (N=N) cm^{-1}. ^1H NMR (DMSO, 200 MHz) δ = 2.1 (t, 2H, CH_2), 2.7 (t, 2H, CH_2), 5.1 (s, 2H, NH_2), 7.1–8.0 (m, 9H, Ar-H) and 8.8 (s, 1H, NH). Anal. Calcd for $C_{18}H_{17}N_9$ (359.4): C, 60.2; H, 4.80; N, 35.1. Found: C, 60.3; H, 5.0; N, 35.4.

2-Amino-4,5,6,7-tetrahydro-3-(4-phenylazophenylazo)-pyrazolo[1,5-*a*]pyrimidin-5-one (7)

To a suspension of **6** (35.94 g, 0.1 mol) in acetic acid (30 mL) conc. HCl (5 mL, 37.5%) was added. The reaction mixture was refluxed for 2 h and then poured into water. The product was filtered off and recrystallized from ethanol. Yield 80 %, Mp: 210 ºC. IR (KBr/m) 3390, 3330 (NH_2), 3120 (NH), 1670 (ring CO) and 1600 (N=N) cm^{-1}. ^1H NMR (DMSO, 200 MHz) δ = 2.5 (t, 2H, CH_2), 2.9 (t, 2H, CH_2), 4.9 (s, 2H, NH2), 7.1–8.0 (m, 9H, Ar-H) and 8.4 (s, 1H, NH). MS *m/z* 360 (M^+), 306, 255, 217, 197, 167, 92 and 77. Anal. Calcd for $C_{18}H_{16}N_8O$ (360.4): C, 60.0; H, 4.50; N, 31.1. Found: C, 59.9; H, 4.2; N, 31.0.

General procedure for the synthesis of (9) and (10)

Equimolar amounts of **2a** (3.063 g, 0.01 mol) and ethyl acetoacetate (1.301 g, 0.01 mol) or acetylacetone (1.001 g, 0.01 mol) were heated at 160 °C (bath temperature) for 8 h. The solid product was filtered and crystallized from the proper solvent.

Compound **9:** Yield 80 %, m.p. >300 °C. IR (KBr/m) 3400 (NH_2), 3330 (NH) and 1700(CO) cm^{-1}. ^1H NMR (DMSO, 200 MHz) δ = 2.5 (s, 3H, CH_3), 5.6 (s, 1H, CH ring), 7.0–8.0 (m, 9H, Ar-H) and 11.1 (s, 1H, NH). Anal. Calcd for $C_{19}H_{16}N_8O$ (372.4): C, 61.3; H, 4.30; N, 30.1. Found: C, 61.1; H, 4.2; N, 30.0.

Compound **10**: Yield 70 %, m.p. 220 °C. IR (KBr/m) 3420, 3380 (NH_2), 3310 d (NH), 1600 (N=N) and 1580 (C=C) cm^{-1}. ^1H NMR (DMSO, 200 MHz) δ = 2.2 (s, 3H, CH_3), 2.3 (s, 3H, CH_3), 5.5 (s, 1H, H6-ring), 5.7 (s, 2H, NH_2), 7.1–8.0 (m, 9H, Ar-H). Anal. Calcd for$C_{20}H_{18}N_8$ (370.4): C, 64.8; H, 4.90; N, 30.3. Found: C, 65.0; H, 4.6;N, 30.6.

3,6-Bis(4-phenylazophenylazo)-2,5,7-triaminopyrazolo[1,5-*a*]-pyrimidine (11)

A mixture of **2a** (30.63 g, 0.1 mol) and **1** (27.43 g, 0.1 mol) was refluxed in DMF for 1 h. The reaction mixture was then poured into water, the solid product was collected by filtration and recrystallized from DMF/H_2O mixture. Yield 60 %, m.p. >300 °C. IR (KBr/m) 3411, 3275, 3150 (NH_2, NH), and 1600–1550 (N=N) cm^{-1}. ^1H NMR (DMSO, 200 MHz) δ = 2.75 (s, 2H, NH_2), 2.85 (s,2H, NH_2), 6.92 (s, 2H, NH_2), 7.4–8.1 (m, 18H, Ar-H). MS *m/z* 581(M^+), 522, 391, 337, 256, 201, 128 and 77. Anal. Calcd for$C_{30}H_{24}N_{14}$ (580.6): C, 62.1; H, 4.20; N, 33.8. Found: C, 62.4; H,4.0; N, 33.5.

4-Amino-3,5-dicyano-6-imino-1-(4-phenylazophenyl)pyridazine (12)

A solution of **1** (2.743 g, 0.01 mol) and malononitrile (0.661 g, 0.01 mol) in pyridine (30 mL) was refluxed for 10 h. It was then cooled and poured into water. The solid product so formed was collected by filtration and crystallized from DMFYield 80 %, m.p. >300 °C. IR (KBr/m): 3340–3000 (NH_2, NH), 2180, 2220 (CN), 1600 and 1550 (N=N) cm^{-1}. MS *m/z* 340 (M^+), 159. Anal. Calcd for $C_{18}H_{12}N_8$ (340.3): C, 63.5; H, 3.60; N, 32.9. Found: C, 63.2; H, 3.8; N, 33.0. Compound **12** was also obtained in 70 % yield via cyclization of **13** by refluxing in DMF for 10 min and working up the reaction mixture.

2-Amino-1,1,3-tricyano-3-(4-phenylazophenylhydrazono)propene (13)

To a solution of 2-amino-1,1,3-tricyanopropene (prepared by dimerization of malononitrile by the reported method[23]) (0.1 mol) in ethanol (100 mL), (5.0 g) of anhydrous sodium acetate was added. The solution was then treated with a solution of diazonium salt of 4-aminoazobenzene (prepared from (19.724 g, 0.1 mol) *p*-aminoazobenzene, acetic acid and the appropriate quantities of sodium nitrite). The reaction mixture was stirred for1 h. The resulting solid product was collected by filtration, washed several times with water and recrystallized from ethanol. Yield 82 %, m.p. >300 °C. IR (KBr/m) 3380–3066 (NH_2, NH-bands, broad), 2216, 2203 (two conjugated CN group), 1641 (C=N) and 1534(N=N) cm^{-1}. Anal. Calcd for $C_{18}H_{12}N_8$ (340.3): C, 63.5; H, 3.6; N, 32.9.Found: C, 63.8; H, 3.3; N, 33.1.

Phenylazophenylhydrazonocyanoacethydrazide (14)

To a solution of (2.09 g, 0.01 mol) diazonium salt of p-aminoazobenzene, a solution of (0.89 g, 0.01 mol), acethydrazide containing 2 g sodium acetate was added. The solid product so formed was collected by filtration and crystallized from etanol. Yield 90 %, m.p. 137 °C. IR (KBr/m) 3340–3000 (NH_2, NH), 2180, 2220 (CN), 1678 (CO) and 1550 (N=N) cm^{-1}. Anal. Calcd for $C_{15}H_{13}N_7O$ (307.3): C, 58.6; H, 4.3; N, 31.9. Found: C, 58.4; H, 4.0; N, 32.1.

5-Amino-4-(4-phenylazophenylazo)-3-isoxazolone (15)

A solution of **14** (3.07g, 0.01 mol) in ethanol (50 mL) was treated with hydroxylamine hydrochloride (0.71g, 0.01 mol) and 2 g sodium acetate. The reaction mixture was stirred for 4 h. The resulting solid product was collected by filteration and recrystallized from methanol**.** Yield 50 %, m.p. 190 °C. IR (KBr/m) 3340–3000 (NH_2, NH-band, broad), 1690 (CO) and 1600 (N=N) cm^{-1}. ^1H NMR (DMSO, 200 MHz) δ = 6.75 (s, 2H, NH_2), 8.4 (s, 1H, NH), 7.4–8.1 (m, 9H, Ar-H). Anal. Calcd for $C_{15}H_{12}N_6O_2$ (308.3): C, 58.4; H, 3.9; N, 27.3. Found: C, 58.5; H, 4.0; N, 27.5.

4-(4-Phenylazophenylazo)-5-oxo-2-pyrazolin-3-ylmalononitrile (16)

A solution of (3.07g, 0.01 mol) of **14** in 50 mL DMF was treated with (0.56g, 0.01 mol) of malononitrile. The reaction mixture was stirred for 30 min and then poured into water. The resulting solid product was collected by filtration and recrystallized from methanol-water mixture**.** Yield 70 %, m.p. 295 °C. IR (KBr/m) 3250–3000 (NH-band, broad), 2200 (CN), 1680 (CO) and 1500 (N=N) cm^{-1}. MS *m/z* 356 (M^+). Anal. Calcd for $C_{18}H_{12}N_8O_2$ (372.3): C, 58.1; H, 3.2; N, 30.1. Found: C, 58.4; H, 3.5; N, 30.6.

N-Methylphenylazophenylhydrazonomalononitrile (17)

To a solution of (2.74g, 0.01 mol) phenylazo-phenylhydrazono malononitrile in acetone (50 mL), methyliodide (1.42g, 0.01 mol) and 2 g of anhydrous potassium carbonate was added. The reaction mixture was refluxed for 90 min, the solvent was evaporated, the solid product was collected by filtration and recrystallized from methanol. Yield 70 %, m.p. 145 °C. IR (KBr/m) 3440–3340 (NH-band, broad), 2200 (CN), and 1500 (N=N) $cm^{-1.}$ ^1H NMR (DMSO, 200 MHz) δ = 3.8 (s, 3H, CH_3), δ 5.5, 5.3 (s, 4H, $2NH_2$), 7.7–8.1 (m, 9H, Ar-H). Anal. Calcd for $C_{16}H_{12}N_6$ (288.3): C, 66.7; H, 4.2; N, 29.2. Found: C, 66.4; H, 4.0; N, 30.2.

N-Methylphenylazophenylhydrazonocyanoacetamidrazone (18)

A solution of (2.9g, 0.01 mol) of **17** in ethanol (50 mL) was treated with 98 % hydrazine hydrate (0.501 g, 0.01 mol). The reaction mixture was refluxed for 90 min, then the solvent was evaporated, the solid product was collected by filtration and recrystallized from ethanol. Yield 70 %, m.p. 172 °C. IR (KBr/m) 3440–3340 (NH_2, broad), 2216 (CN), 1680 (CO), and 1550 (N=N) cm^{-1}. Anal. Calcd for $C_{16}H_{16}N_8$ (320.4): C, 60.0; H, 5.0; N, 35.0. Found: C, 60.2; H, 4.8; N, 35.2.

Reaction of (18) with benzoylisothiocyanate

To a solution of benzoylisothiocyanate (1.31g, 0.01 mol) in acetone, **18** (3.2g, 0.01 mol) was added. The reaction mixture was refluxed for 2 h., the solvent was evaporated, the solid product was collected by filtration and recrystallized from DMF-water mixture to give 1-amino-1,3,5-triazine derivative (**19**). Yield 40%, m.p. 145 °C. IR (KBr/m) 3190–3000 (NH_2), 220 (CN), and 1570 (N=N) cm^{-1}. MS *m/z* 420 (M^+- 59). Anal. Calcd for $C_{24}H_{19}N_9S$ (465.5): C, 61.9; H, 4.1; N, 27.1 S, 6.9. Found: C, 61.4; H, 3.9; N, 28.5.S, 6.68

Conclusions

In this work, a series of bisazopyrazolo[1,5-*a*]pyrimidine, pyridazine, isoxazole, and triazine dyes have been synthesized. IR, ^{1}H NMR, and mass spectroscopy for the prepared compounds are in good agreement with the proposed structures.

References

[1]Bareini, Z., Synthesis and characterisation of some new arylazopyridone dyes, *Pigm. Resin Technol*., **2009**, *5*, 298. https://doi.org/10.1108/03699420910988778

[2]Karipcin, F., Dede, B., Percin-Ozkorucuklu, S., Mn(II), Co(II) and Ni(II) complexes of 4-(2-thiazolylazo)resorcinol: Syntheses, characterization, catalase-like activity, thermal and electrochemical behaviour, *Dyes Pigm*., **2010**, *84*, 14. https://doi.org/10.1016/j.dyepig.2009.06.010

[3]Dickey, J. B., Towne, E. B., Bloom, M. S., Moore, W. H., Hill, H. M., Heynemann, H., Hedberg, D. G., Sievers, D. C., Otis, M.V., Azo Dyes from Substituted 2-Aminothiazoles**,** *J. Org. Chem*., **1959**, *24*, 187-196. **DOI:** 10.1021/jo01084a010

[4]Annen, O., Egli, R., Hasler, R., Hen B., Jakob, H., Matzinger, P., Replacement of disperse anthraquinonedye, *Rev. Prog. Color*., **1987**, *17*, 72–85.

[5]Tsai, P. C., Wang, I. J., Synthesis and solvatochromic properties of some disazo dyes derived from pyrazolo[1,5-*a*]pyrimidine derivatives, *Dyes Pigm*., **2005**, *64*, 259. https://doi.org/10.1016/j.dyepig.2004.05.013

[6]Yang, B., Yuan, L., Chao-Jun, C., Jian-Ping, C., Meng-Shen, C., The synthesis of 5-amino-4-arylazo-3-methyl-1*H*-pyrazoles and 5-aryl-3-methylpyrazole[3,4-e][1,2,3,4]tetrazines, *Dyes Pigm*., **2009**, *83*, 144. https://doi.org/10.1016/j.dyepig.2008.12.011

[7]Kumar, V., Aggarwal, R., Tyagi, P., Singh, S., Synthesis and antibacterial activity of some new 1-heteroaryl-5-amino-4-phenyl-3-trifluoromethylpyrazoles, *Eur. J. Med. Chem*., **2005**, *40*, 922. DOI: 10.1016/j.ejmech.2005.03.021

[8]Jung, J. C., Walkins, E. B., Avery, M. A., Synthesis of 3-substituted and 3,4-disubstituted pyrazolin-5-ones, *Tetrahedron*, **2002**, *58(18)*, 3639-3646.

[9]Gudmundsson, K. S., Johns, B. A., Wang, Z., Turner, E. M., Allen, S. H., Freeman, G. A., Lesleboyd, F., Sexton, C. D., Sellseth, D. W., Moniri, K. R., Greeh, K. L., Synthesis of novel substituted 2-phenylpyrazolopyridines with potent activity against herpesviruses, *Bioorg. Med. Chem*., **2005**, *13*, 5346. https://doi.org/10.1016/j.bmc.2005.05.043

[10]Hwang, S. H., Wagner, K. M., Morisseau, C., Liu, J.-Y., Dong, H., Wecksler, A. T., Hammock, B. D., Synthesis and Structure−Activity Relationship Studies of Urea-Containing Pyrazoles as Dual Inhibitors of Cyclooxygenase-2 and Soluble Epoxide Hydrolase, *J. Med. Chem*., **2011**, *54*, 3037. **DOI:** 10.1021/jm2001376

[11]Szabo, Gy., Fischer, J., Gyires, K., New Celecoxib Derivatives as Anti-Inflammatory Agents, *J. Med. Chem*., **2008**, *51*, 142; **DOI:** 10.1021/jm070821f; Hiremith, S .P., Rudresh, K., Saundan, A. R. I., Synthesis and biological activities of new 5-hydrazino-10-substituted-7 *H*-indolo[2, 3-*c*]isoquinolines and 1-(10-substituted-7*H*-indolo[2,3-*c*]isoquinolin-5-yl)-3, 5-disubstituted pyrazoles, -3-methyl pyrazol-5-ones and -3, 5-disubstituted pyrazolines, *Indian J. Chem*., **2002**, *41B* (*2*), 394. http://hdl.handle.net/123456789/21824

[12]Chimichi, S., Boccalini, M., Hassan, M. M. M., Viola, G., DallAcqua, F., Curini, M., Synthesis, structural determination and photo-antiproliferative activity of new 3-pyrazolyl or -isoxazolyl substituted 4-hydroxy-2(1*H*)-quinolinones, *Tetrahedron*, **2006**, *62*, 90. https://doi.org/10.1016/j.tet.2005.09.135

[13]Elnagdi, M. H., Kandeel, E. M., Zayed, E. M., Kandeel, Z. E., Pyrimidine derivatives and related compounds VI. A novel synthesis of 3,5-diacetamidopyrazole and of 2-aminopyrazolo [1,5-α] pyrimidines, *J. Heterocycl. Chem*., **1977**, *14*, 155. https://doi.org/10.1002/jhet.5570140132

[14]Elnagdi, M. H., Fahmy, S. M., Hafez, E. A. Z., Elmoghayar, M. R. H., Amer, S. A. R., Pyrimidine derivatives and related compounds. A novel synthesis of pyrimidines, pyrazolo[4,3-*d*]pyrimidines and isoxazolo[4,3-*d*] pyrimidine, *J. Heterocycl. Chem*., **1979**, *16*, 1109. https://doi.org/10.1002/jhet.5570160606

[15]Alexandre, V. I., Dmitri, E.D. Elena, S.G. Elena, S.D. Madina, G.K. Angela, G.K. Volodymyr, M.K. Oleg, D.M. Sergey, E.T. Ilya, M.O. Anton, A.V., Synthesis of cycloalkane-annelated 3-phenylsulfonyl-pyrazolo[1,5-*a*]pyrimidines and their evaluation as 5-HT_6 receptor antagonists, *Bioorg. Med. Chem. Lett.*, **2010**, *20*, 2133. https://doi.org/10.1016/j.bmcl.2010.02.046

[16]Kim, I., Song, J. H., Park, C. M., Jeong, J. W., Kim, H. R., Ha, J. R., No, Z., Hyun, J. L., Cho, Y. S., Sook Akng, N., Jeon? D. J., Design, synthesis, and evaluation of 2-aryl-7-(3',4'-dialkoxyphenyl)-pyrazolo[1,5-a]pyrimidines as novel PDE-4 inhibitors, *Bioorg. Med. Chem. Lett*., **2010**, *20*, 922. DOI:10.1016/j.bmcl.2009.12.070

[17]Helal, M. H., Elgemeie, G. H., Masoud, D. M., Preparation and characterisation of novel methylsulfanylpyrazolopyrimidines as heterocyclic dyes from ketene dithioacetals, *Pigm. Resin Technol*., **2007**, *36*, 306. https://doi.org/10.1108/03699420710820423

[18]Ho, Y. W., Synthesis of some new azo pyrazolo[1,5-*a*]pyrimidine-thieno[2,3-*b*]pyridine derivatives and their application as disperse dyes, *Dyes Pigm*., **2005**, *64*, 223. https://doi.org/10.1016/j.dyepig.2004.06.007

[19]Karcı, F., Demircalı, A., Synthesis of disazo pyrazolo[1,5-*a*]pyrimidines, *Dyes Pigm*., **2007**, *74*, 288. https://doi.org/10.1016/j.dyepig.2006.02.007

[20]Fadda, A. A., Refaat, H. M., Zaki, M. E. A., Monir, E., Reaction of isatoic anhydride with bifunctional reagents: synthesis of some new quinazoline fused heterocycles, 2-substituted anilinoheterocyclic derivatives and other related compounds, *Synt. Commun*., **2001**, *31*, 3537. https://doi.org/10.1081/SCC-100106216

[21]Taylor, E. C., McKillop, A., *Advances in Organic Chemistry*, Wiley and Sons, New York, **1970**, vol. 7.

[22]Baldwin, S. Infrared and Ultraviolet Absorption Spectra of Enaminonitriles, *J. Org. Chem*., **1961**, *26*, 3288. **DOI:** 10.1021/jo01067a061

[23]Taylor, E. C., Hartke, K. S., The Reaction of Malononitrile with Substituted Hydrazines: New Routes to 4-Aminopyrazolo[3,4-d]pyrimidines, *J. Am. Chem. Soc*., **1959**, *81*, 2454. **DOI:** 10.1021/ja01519a045

Received: 29.09.2018.
Accepted: 03.11.2018.

ENERGY CRITERIA IN BIOSYSTEMS

G. A. Korablev[a]*

Keywords: Potential gradient; corpuscular-wave dualism; Spatial-energy parameter; biosystems; stationary and pathological states.

An analysis of the orientation of structural interactions was carried out on the basis of the first law of thermodynamics. In the systems in which the interaction proceeds along the potential gradient (positive work), the resultant potential energy is found based on the principle of adding reciprocals of corresponding energies of subsystems - there is a corpuscular mechanism. In the systems in which the interactions proceed against the potential gradient (negative performance) the algebraic addition of their masses, as well as the corresponding energies of subsystems is performed - there is a wave mechanism. Act of quantum action expressed via Plank's constant is narrowed to the energy equilibrium-exchange redistribution between the corpuscular and wave processes, which is demonstrated via the angular vector of such motion. Energy characteristics of functional states of bio-systems are defined basically by P-parameter values of atom first valence electron. The principles of stationary biosystem formation are similar to the conditions of wave processes in the phase. Under the condition of the minimum of such interactions, the pathological (but not stationary) biostructures containing the molecular hydrogen can be formed.

* Corresponding Authors
E-Mail: korablevga@mail.ru
[a] Izhevsk State Agricultural Academy, Izvhessk? Russian Federation

Introduction

To obtain the dependence between energy parameters of free atoms and degree of structural interactions in simple and complex systems is one of the strategic tasks in physical chemistry. Classical physics and quantum mechanics widely use Coulomb interactions and their variations for this.

Thus in Van der Waals treatment, [1] orientation and charge-dipole interactions are referred to electron-conformation interactions in bio-systems and as a particular case, exchange-resonance transfer of energy. But biological and many cluster systems are electroneutral in structural basis. Therefore non-Coulomb equilibrium-exchange spatial-energy interactions, i.e. non-charge electrostatic processes, are mainly important for them.

The structural interactions of summed electron densities of valence orbitals of corresponding conformation centres take place, that is processes of equilibrium flow of electron densities, due to overlapping of their wave functions.

Heisenberg and Dirac[2] proposed the exchange Hamiltonian assuming a direct overlapping of wave functions of interacting centres, $\bar{H} = -I_0 S_1 S_2$, where: $\bar{H}$ = spin operator of isotropic exchange interaction for pair of atoms, I_0 is the exchange constant, S_1 and S_2 are the overlapping integrals of wave functions. In this model electrostatic interactions are modelled by effective Hamiltonian exchange acting in the space of spin functions. In particular, such approach is applied to the analysis of structural interactions in cluster systems. It was demonstrated in Anderson's works[3] that in compounds of transition elements when the distance between paramagnetic ions considerably exceeds the total of their covalent radii, "superexchange" processes of overlapping cation orbitals take place through the anion between them.

In this work similar equilibrium-exchange processes are evaluated through the notion of spatial-energy parameter, the P-parameter.

Principles of adding energy characteristics of interactions

The analysis of kinetics of various physical and chemical processes shows that in many cases the reciprocals of velocities, kinetic or energy characteristics of the corresponding interactions are added. It is also known from classical mechanics that the relative motion of two particles with the interaction energy U(r) takes place as the motion of material point with the reduced mass μ (eqn. 1), in the field of central force U(r), and general translational motion, as a free motion of material point with the mass (eqn.2). Such relationships are known in quantum mechanics as well.[4]

$$\frac{1}{\mu} = \frac{1}{m_1} + \frac{1}{m_2} \qquad (1)$$

$$m = m_1 + m_2 \qquad (2)$$

For moving thermodynamic systems, the first rule of thermodynamics is given by eqn. (3), where δE = amount of energy transferred to the system, $d(U + mv^2/2)$ characterizes the changes in internal and kinetic energies of the system, $+\delta A$ is the work performed by the system and $-\delta A$ is the work performed with the system.

$$\delta E = d\left(U + \frac{mv^2}{2}\right) \pm \delta A \qquad (3)$$

As the work value numerically equals the change in the potential energy, then

$$+\delta A = -\Delta U \qquad (4)$$

and

$$-\delta A = +\Delta U \qquad (5)$$

The character of the change in the potential energy value (ΔU) was analyzed by its sign for various potential fields and the results are given in Table 1. From the Table 1 it can be seen that the values $-\Delta U$ and accordingly $+\delta A$ (positive work) correspond to the interactions taking place along the potential gradient, and ΔU and $-\delta A$ (negative work) occur during the interactions against the potential gradient.

The solution of the interaction of two material points with masses m_1 and m_2 obtained under the condition of the absence of external forces, corresponds to the interactions flowing along the gradient, the positive work is performed by the system (similar to the attraction process in the gravitation field).

Table 1. Direction of the interaction processes.

No.	Systems	Type of potential field	Process	U	r_2/r_1; x_2/x_1	U_2/U_1	Sign ΔU	Sign δA	Direction of potential field
1	opposite electrical charges	electrostatic	attraction	$-k\frac{q_1q_2}{r}$	$r_2 < r_1$	$U_2 > U_1$	-	+	along the gradient
			repulsion	$-k\frac{q_1q_2}{r}$	$r_2 > r_1$	$U_2 < U_1$	+	-	against the gradient
2	similar electrical charges	electrostatic	attraction	$k\frac{q_1q_2}{r}$	$r_2 < r_1$	$U_2 > U_1$	+	-	against the gradient
			repulsion	$k\frac{q_1q_2}{r}$	$r_2 > r_1$	$U_2 < U_1$	-	+	along the gradient
3	elementary masses m_1 and m_2	gravitational	attraction	$-\gamma\frac{m_1m_2}{r}$	$r_2 < r_1$	$U_2 > U_1$	-	+	along the gradient
			repulsion	$-\gamma\frac{m_1m_2}{r}$	$r_2 > r_1$	$U_2 < U_1$	+	-	against the gradient
4	spring deformation	field of elastic forces	compression	$k\frac{\Delta x^2}{2}$	$x_2 < x_1$	$U_2 > U_1$	+	-	against the gradient
			extension	$k\frac{\Delta x^2}{2}$	$x_2 > x_1$	$U_2 > U_1$	+	-	against the gradient
5	photoeffect	electrostatic	repulsion	$k\frac{q_1q_2}{r}$	$r_2 > r_1$	$U_2 < U_1$	-	+	along the gradient

Table 2. P-parameters of atoms calculated via the electron bond energy.

Atom	Valence electrons	W, eV	r_i, Å	q_0^2, eVÅ	P_0, eVÅ	R, Å	$P_E = P_0/R$, eV
H	$1S^1$	13.595	0.5292	14.394	4.7969	0.5292	9.0644
						0.375	12.792
						0.28	17.132
C	$2P^1$	11.792	0.596	35.395	5.8680	0.77	7.6208
						0.67	8.7582
						0.60	9.780
	$2P^2$	11.792	0.596	35.395	10.061	0.77	13.066
						0.67	15.016
						0.60	16.769
	$2P^3{}_r$				13.213	0.77	17.160
	$2S^1$	19.201	0.620	37.240	9.0209	0.77	11.715
	$2S^2$				14.524	0.77	18.862
	$2S^1+2P^3{}_r$				22.234	0.77	28.875
	$2S^1+2P^1{}_r$				13.425	0.77	17.435
	$2S^2+2P^2$				24.585	0.77	31.929
					24.585	0.67	36.694
						0.60	40.975

N	$2P^1$	15.445	0.4875	52.912	6.5916	0.70	9.4166
						0.55	11.985
	$2P^2$				11.723	0.70	16.747
						0.63	18.608
	$2P^3$				15.830	0.70	22.614
						0.55	28.782
	$2S^2$	25.724	0.521	53.283	17.833	0.70	25.476
	$2S^2+2P^3$				33.663	0.70	48.090
O	$2P^1$	17.195	0.4135	71.383	6.4663	0.66	9.7979
	$2P^1$					0.55	11.757
	$2P^2$	17.195	0.4135	71.383	11.858	0.66	17.967
						0.59	20.048
	$2P^4$	17.195	0.4135	71.383	20.338	0.66	30.815
						0.59	34.471
	$2S^2$	33.859	0.450	72.620	21.466	0.66	32.524
	$2S^2+2P^4$				41.804	0.66	63.339
						0.59	70.854

The solution of this equation via the reduced mass (μ) is the Lagrangian equation for the relative motion of the isolated system of two interacting material points with masses m_1 and m_2, which in coordinate x is as follows.

$$\mu \cdot x'' = -\frac{\partial U}{\partial x} \qquad (6)$$

Here U is the mutual potential energy of material points, μ is reduced mass. At the same time, $x'' = a$ (feature of the system acceleration). For initial portions of the interactions Δx can be taken as follows.

$$\frac{\partial U}{\partial x} \approx \frac{\Delta U}{\Delta x} \qquad (7a)$$

that is

$$\mu a \Delta x = -\Delta U \qquad (7b)$$

then

$$\frac{1}{1/(a\Delta x)} \times \frac{1}{(1/m_1+1/m_2)} \approx -\Delta U \qquad (7c)$$

and

$$\frac{1}{1/(m_1 a\Delta x)+1/(m_2 a\Delta x)} \approx -\Delta U \qquad (8)$$

or

$$\frac{1}{\Delta U} \approx \frac{1}{\Delta U_1} + \frac{1}{\Delta U_2} \qquad (9)$$

where ΔU_1 and ΔU_2 are potential energies of material points on the elementary portion of interactions and ΔU is the resulting (mutual) potential energy of these interactions. Therefore:

1. In the systems in which the interactions proceed along the potential gradient (positive performance), the resulting potential energy is found based on the principle of adding reciprocals of the corresponding energies of subsystems.[5] Similarly, the reduced mass for the relative motion of two-particle system is calculated.

2. In the systems in which the interactions proceed against the potential gradient (negative performance), the algebraic addition of their masses, as well as the corresponding energies of subsystems, is performed (by the analogy with Hamiltonian).

Spatial-energy parameter (P-parameter)

From the Eqn. (9) it is seen that the resulting energy characteristic of the system of two material points interaction is based on the principle of adding reciprocals of initial energies of interacting subsystems.

Electron with mass m moving near the proton with mass M is equivalent to the particle with mass as given in eqn. (10).[6]

$$\mu = \frac{mM}{m+M} \qquad (10)$$

Therefore, when modifying the eqn. (6), we can assume that the energy of atom valence orbitals (responsible for interatomic interactions) can be calculated[5] by the principle of adding reciprocals of some initial energy components based on the following equations.

$$\frac{1}{q^2/r_i} + \frac{1}{W_i n_i} = \frac{1}{P_E} \qquad (11)$$

$$\frac{1}{P_0} = \frac{1}{q^2} + \frac{1}{(Wrn)_i} \qquad (12)$$

$$P_E = \frac{P_0}{r_i} \qquad (13)$$

Here W_i is the electron orbital energy,[7] r_i is orbital radius of i–orbital,[8] $q=Z^*/n^*$,[9] n_i is the number of electrons of the given orbital, Z^* and n^* are nucleus effective charge and effective main quantum number and r is the bond dimensional characteristics.

P_0 was called spatial-energy parameter (*SEP*), and P_E – effective *P*–parameter (effective *SEP*). Effective *SEP* has physical sense of some averaged energy of valence electrons in the atom and is measured in energy units, e.g. electron-volts (eV). The values of P_0-parameter are tabulated constants for the electrons of the given atom orbital. For dimensionality, SEP can be written down as eqn. (14).

$$[P_0] = [q^2] = [E] \times [r] = [h] \times [v] = \frac{kg \times m^3}{s^2} = J \times m \quad (14)$$

where $[E]$, $[h]$ and $[v]$ are dimensions of energy, Planck's constant and velocity, respectively. Thus *P*-parameter corresponds to the processes going along the potential gradient.

The introduction of *P*-parameter should be considered as further development of quasi-classical notions using quantum-mechanical data on atom structure to obtain the criteria of energy conditions of phase-formation. At the same time, for the systems of similarly charged homogeneous systems (e.g., orbitals of the given atom) the principle of algebraic addition of such parameters is preserved.

$$\sum P_E = \sum (P_0/r) \quad (15)$$

or

$$r \sum P_E = \sum P_0 \quad (16)$$

The *P*-parameters of valence orbitals of all the atoms are given in Table 2.

According to the established rule[5] about addition of *P*-parameters of similarly charged or homogeneous systems for two orbitals in the given atom with different quantum characteristics and also according to the energy conservation rule we have eqn. (17), where $E_k = mv^2/2$ and is electron kinetic energy.

$$\frac{d^2P_0}{dx^2} + \frac{8\pi^2 m}{h^2} P_0 E_k = 0 \quad (17)$$

Schrodinger equation for the stationery state in coordinate *x* is given in eqn. (18).

$$\frac{d^2\psi}{dx^2} + \frac{8\pi^2 m}{h^2} \psi E_k = 0 \quad (18)$$

By comparing these two equations, we see that P_0-parameter correlates numerically with the values of ψ -function i.e., $P_0 \approx \psi$, and is generally proportional to it or $P_0 \sim \psi$. Taking into account the broad practical opportunities of applying the P-parameter methodology, we can consider this parameter as the materialized analog of ψ-function. Since P_0-parameters like ψ-functions have wave properties, the superposition principles should be fulfilled for them also, defining the linear character of the equations of adding and changing *P*-parameters.

Structural exchange spatial-energy interactions

In the process of solid solution formation and other structural equilibrium-exchange interactions the single electron density should be set in the points of atom-component contact. This process is accompanied by the redistribution of electron density between the valence areas of both particles and transition of the part of electrons from some external spheres into the neighbouring ones. Apparently, the frame atom electrons do not take part in such exchange.

Obviously, when electron densities in free atom-components are similar, the transfer processes between boundary atoms of particles are minimal. This will be favourable for the formation of a new structure. Thus, the evaluation of the degree of structural interactions in many cases means the comparative assessment of the electron density of valence electrons in free atoms (on averaged orbitals) participating in the process, which can be correlated with the help of P-parameter model.

The less is the difference $(P'_0/r'_i - P''_0/r''_i)$, the more favourable is the formation of a new structure or solid solution from the energy point of view.

In this regard, the maximum total solubility, evaluated via the coefficient of structural interaction α, is determined by the condition of minimum α value, which represents the relative difference of effective energies of external orbitals of interacting subsystems (eqns. 19 and 20), where P_S, the structural parameter is found by the eqn. (21), where N_1 and N_2 are the number of homogeneous atoms in subsystems. (Table 3).

$$\alpha = \frac{P'_o/r'_i - P''_o/r''_i}{(P'_o/r'_i - P''_o/r''_i)/2} 100\% \quad (19)$$

$$\alpha = \frac{P'_c - P''_c}{P'_c + P''_c} 200\% \quad (20)$$

$$\frac{1}{P_c} = \frac{1}{N_1 P'_E} + \frac{1}{N_2 P''_E} + \cdots \quad (21)$$

Table 3. Structural P_C-parameters calculated via the electron bond energy.

Radicals, molecule fragments	P_E', eV	P_E'', eV	P_G, eV	Orbitals
OH	9.7979	9.0644	4.7084	O ($2P^1$)
	30.815	17.132	11.011	O ($2P^4$)
	17.967	17.132	8.7710	O ($2P^2$)
H_2O	2·9.0644	17.967	9.0237	O ($2P^2$)
	2·17.132	17.967	11.786	O ($2P^2$)
CH_2	17.160	2·9.0644	8.8156	C ($2S^12P^3{}_r$)
	31.929	2·17.132	16.528	C ($2S^22P^2$)
	36.694	2·9.0644	12.134	C ($2S^12P^3{}_r$)
CH_3	31.929	3·17.132	19.694	C ($2S^22P^2$)
	15.016	3·9.0644	9.6740	C ($2P^2$)
CH	36.694	17.132	11.679	C ($2S^22P^2$)
	17.435	17.132	8.6423	C ($2S^22P^2$)
NH	16.747	17.132	8.4687	N($2P^2$)
	48.090	17.132	12.632	N($2S^22P^3$)
NH_2	18.608	2·9.0644	9.1827	N($2P^2$)
	16.747	2·17.132	12.631	N($2P^2$)
	28.782	2·17.132	18.450	N($2P^3$)
C_2H_5	2·31.929	5·17.132	36.585	C ($2S^22P^2$)
NO	18.608	17.967	9.1410	N($2P^2$)
	28.782	20.048	11.817	N($2P^3$)
CH_2	31.929	2·9.0644	11.563	C ($2S^22P^2$)

CH_3	16.769	3·17.132	12.640	C ($2P^2$)
CH_3	17.160	3·17.132	12.865	C ($2P^3_r$)
CO–OH	8.4405	8.7710	4.3013	C ($2P^2$)
CO	31.929	20.048	12.315	C ($2S^22P^2$)
C=O	15.016	20.048	8.4405	C ($2P^2$)
C=O	31.929	34.471	16.576	O ($2P^4$)
CO=O	36.694	34.471	17.775	O ($2P^4$)
C–CH_3	31.929	19.694	12.181	C ($2S^22P^2$)
C–CH_3	17.435	19.694	9.2479	C ($2S^12P^1$)
C–NH_2	31.929	18.450	11.693	C ($2S^22P^2$)
C–NH_2	17.435	18.450	8.8844	C ($2S^12P^1$)
C–OH	8.7572	8.7710	4.3821	

Applying the reliable experimental data we obtain the nomogram of structural interaction degree dependence (ρ) on coefficient α, for a wide range of structures (Figure 1).

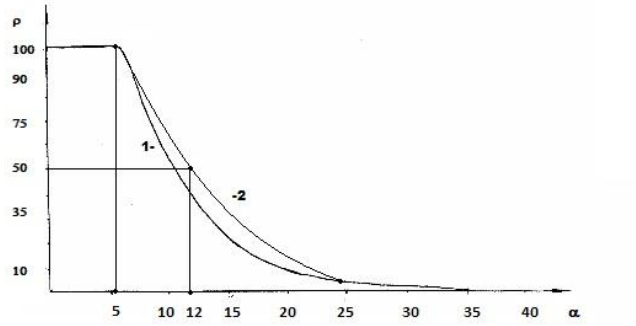

Figure 1. Nomogram of structural interaction degree dependence (ρ) on coefficient α. The curve 2 is for biosystems.

This approach gives the possibility to evaluate the degree and direction of the structural interactions of phase formation, isomorphism and solubility processes in multiple systems, including molecular ones.

Corpuscular-wave mechanism

The formalism of the Eqns. (11), (12) and (21) is not principally new. Already in 1924 the following equation was obtained based on Compton's effect.

$$\frac{1}{h\nu'} = \frac{1}{h\nu} + \frac{1-\cos\theta}{mc^2} \qquad (22)$$

Here, $h\nu'$ the energy of scattered photon, $h\nu$ is energy of incident photon, mc^2 is the own energy of electron and θ is the scattering angle. At the same time, the energy of photons decreases by the value additionally obtained by the electron. In this way the act of quantum action takes place, resulting in the energy redistribution between the corpuscular and wave properties of the interacting systems. In this process, the same as in photo effect, the interaction proceeds along the potential gradient and the work is positive.

During the quantum transitions in the atom, similarly charged particles (electrons) interact by irradiation, i.e., by the wave process. At the same time, for dissimilarly charged particles (electrons and nucleus of atoms) the process goes along the potential gradient, i.e., by corpuscular mechanism. It is known that a particle can have three main motions, translational, rotational and oscillatory. But quantum mechanics does not consider the issue of electron trajectory as we can speak only of the possibility of its location in the given point in space. But an electron also moves if this translational motion goes along the potential gradient, then it corresponds to corpuscular process, and rotational motion to wave one. Electric current is the motion of electrons along the potential gradient.

If we assume that the magnetic field generated by it is a wave process, there has to be a ratio between the electric and magnetic constants. The difference of phases of electric and magnetic oscillations in electromagnetic wave is π/2. Having introduced the coefficient $(2/\pi)^2$, we have the equation for Plank's constant with the accuracy close to the initial data themselves.

$$h = (4/\pi^2 + a)Pe\varepsilon/\mu \qquad (23)$$

Here a = 0.0023293 and is defined as experimental quantum correction to spin g_s-factor of the electron, ε is the electric constant, μ = magnetic constant and h is Plank's constant. For a free electron $P_e = Wr$, where W = 0.510034 MeV = 0.81872×10^{-13} J. The value of classical radius of electron r = 2.81794×10^{-15} m was used as the dimensional characteristic and, therefore, $P_e = 2.30712 \times 10^{-28}$ Jm.

The proportionality coefficient in the eqn. (23) has the velocity dimensionality (m s^{-1}) for the ratio (F/H_n), i.e. in such way the rate of energy redistribution in the system "particle-wave" is characterized. Therefore, the act of quantum action expressed via Planck's constant is narrowed to the energy equilibrium-exchange redistribution between the corpuscular and wave processes.

Generalizing the formalism of the eqns. (11), (12) and (21) onto all other interactions flowing along the potential gradient, we can make the conclusion that corpuscular processes take place in these cases, and wave dualism corresponds to the interactions against the potential gradient.

Corner angles

Let us consider some macro processes important in this case. The silkworm winds the natural (organic) silk thread only at a definite rotation angle. In cosmonautics the cellulose-viscose thread is wound around the metal cylinder of the spaceship following the special technology, and, what is important, at the same winding angle as the silkworm. The spaceship becomes most durable, more technologically high-quality and lighter.[11-13] We can also speak of other examples of such phenomenon. This angle (mainly as applicable to organic systems) was called the geodesic angle: φ_g = 54.73° = 54°44'.

The notions of breaking stress in the process of plastics stretching by its winding pitch has been reported in literature,[12,13] where σ_α = axial and σ_β = circumferential stress, which are replaced by the value N_α = axial effort and N_β = circumferential effort proportional to them. At the same time, the following equation is fulfilled.

$$\frac{\sigma_\beta}{\sigma_\alpha} = \frac{N_\beta}{N_\alpha} = \mathrm{tg}^2\varphi_g = 2 \qquad (24)$$

This condition allows the formation of equally tensioned system of threads with the minimal item weight.[13] Thus, the rotation angle numerically determines the ratio of two legs of the triangle, whose values characterize energy and dependencies in the system with quantum and wave processes through axial and circumferential stresses.

All this is broadly demonstrated in macro- and micro-processes. Below are some examples.

(1) Characteristic of spin-orbital interaction – constant of fine structure $\alpha = r/\lambda$, where r = classical radius of electron, λ = its Compton wavelength.

(2) Formally, but similarly: the interaction force of two long conductors with current is proportional to the ratio $l/2\pi r$, where l = length of conductors and r is the distance between them.

(3) π equals the ratio of circumference length to its diameter.

(4) In quantum mechanics the ratio of magnetic moment to its mechanical moment is called the magnetomechanic ratio, g. At the same time, $g_s = 2$, if the magnetic moment of an electron is conditioned only by the spin component, and g = 1, if it is produced by the orbital motion of electrons. Their ratio $g_s/g = 2$, the same as $tg^2\varphi_g = 2$, which characterizes the existing corpuscular-wave dependencies.

In these examples, as in many others, such approach allows evaluation of structural interactions based on corpuscular and wave dependencies in each action act, e.g., in the equation of dependence of rotational and orbital motion of planets.[14] Using the algorithm in the ratio ρ/α to obtain the linear dependence with the rotation angle φ and in accordance with the Eqn. (24) we have:

$$\ln(\rho/\alpha) = \mathrm{tg}\varphi \qquad (25)$$

In homogeneous systems with the closeness of values of their P-parameters (wave process) if $\alpha \to 0$, then $tg\varphi \to \infty$ and $\varphi = 90°$. In the corpuscular mechanism of interaction if $\alpha \to \infty$, then $tg\alpha \to 0$, and $\varphi = 0$. In general case, in the system "particle-wave" the rotation angle φ changes from 0° (at ρ = 0 %) up to 90° (at ρ = 100 %). It can be assumed that equally strained system is obtained under the condition of approximate equality of corpuscular and wave parameters, i.e. at the geodesic angle ρ = 50 %. Then the calculation of the coefficient α by the eqn. (25) gives 12.16 %, approximately corresponding to the coordinates obtained in nomogram in figure 1. Similar types by this nomogram and its reverse-reading variants are the graphic characteristics of many phenomena and processes in nature, engineering and economy. Therefore, such *S*-curves have been called "Lines of life".

Bio-structural energy criteria of functional states

Isomorphism as a phenomenon is usually considered as applicable to crystal structures. But, obviously, similar processes can also flow between molecular compounds, where the bond energy can be evaluated via the relative difference of electron densities of valence orbitals of interacting atoms. Therefore, the molecular electronegativity is quite easily calculated via the values of the corresponding *P*-parameters. Since *P*-parameter possesses wave properties (similar to φ-function), mainly the regularities in the interference of the corresponding waves should be fulfilled. The minimum interference, oscillation weakening (in anti-phase), takes place if the difference in wave move (Δ) equals the odd number of semi-waves (eqn. 26).

$$\Delta = (2n+1)\frac{\lambda}{2} = \lambda\left(n+\frac{1}{2}\right) \quad \text{where } n = 0, 1, 2, 3 \qquad (26)$$

The difference in wave move (Δ) for P-parameters can be evaluated via their relative value.

$$\ldots \qquad \gamma = \frac{P_2}{P_1} = \left(n+\frac{1}{2}\right) = \frac{3}{2}, \frac{5}{2} \qquad (27)$$

Maximum interference, oscillation enhancing (in phase), takes place if the difference in wave move equals an even number of semi-waves.

$$\Delta = 2n\frac{\gamma}{2} = \gamma n \text{ or } \Delta = \gamma(n+1) \qquad (28)$$

As applicable to *P*-parameters, the maximum enhancement in interaction in the phase corresponds to the interactions of similarly charged systems or systems homogeneous by their properties and functions (e.g. between the fragments or blocks of complex organic structures, such as CH_2 and NNO_2). And then

$$\gamma = \frac{P_2}{P_1} = (n+1) \qquad (29)$$

It has been shown[15] that the molecular negativity is numerically equal to the *P*-parameter of the first valence electron divided by 3. Hydrogen atom, element No 1 with orbital $1S^1$ defines the main energy criteria of structural interactions (their "ancestor").

Table 1 shows its three P_E-parameters corresponding to three different characteristics of the atom.

R_1 = 0.5292 Å, the orbital radius, a quantum-mechanical characteristic gives the initial main value of P_E-parameter equal to 9.0644 eV. R_2 = 0.375 Å, a distance equal to the half of the bond energy in H_2 molecule. But if hydrogen atom is bound with other atoms, its covalent radius is ≈ 0.28 Å.

In accordance with equation (23) $P_2 = P_1(n+1)$, therefore $P_1 \approx$ 9.0644 eV, $P_2 \approx$ 18.129 eV. These are the values of possible energy criteria of stable (stationary) structures. The dimensional characteristic 0.375 Å does not satisfy them, therefore, there is a transition onto to the covalence radius ≈ 0.28 Å, which provides the value of *P*-parameter approximately equal to P_2.

It was shown earlier[5] that the condition for the formation of stable structures is an approximate equality of the *P*-parameter of the subsystems. From a big number of different combinations of interactions, we can obtain series with approximately equal values of *P*-parameters of atoms (or radicals). Such series, by initial values of hydrogen atom, are given in Table 4 (at $\alpha < 7.5$ %).

First series for P_E = 9.0644 eV, the initial satge, where H, C, O, N atoms have P_E-parameters only of the first electron and interactions proceed in the phase.

Second series for P'_E = 12.792 eV is the non-rational and pathological as it more corresponds to the interactions in anti-phase by eqn. (27) and P''_E = 13.596 eV. Coefficient α between the parameters P'_E and P''_E equals 6.1 %, thus defining the possibility of forming "false" biostructures containing the molecular hydrogen. Coefficient α between series I and II is 34.1 %, thus confirming the irrationality of series II.

Third series for P'_E = 17.132 eV and is stationary as the interactions are in the phase. By eqn. (27) P''_E = 18.129 eV (α= 5.5 %).

Table 4. Biostructural spatial-energy parameters (eV).

Series No.	H	C	N	O	CH	CO	NH	C–NH_2	C–CH_3	<P_E>	α
I	9.0644 ($1S^1$)	8.7582 ($2P^1$) 9.780 ($2P^1$)	9.4166 ($2P^1$)	9.7979 ($2P^1$)	9.1330 ($2S^22P^2$–$1S^1$)	8.4405 ($2P^2$–$2P^2$)	8.4687 ($2P^2$–$1S^1$) 9.1281 ($2P^2$–$1S^1$)	8.8844 $2S^12P^1{}_r$– ($2P^3$–$1S^1$)	9.2479 $2S^12P^1{}_r$– ($2S^2$ $2P^2$–$1S^1$)	9.1018	0.34–7.54
II	12.792 ($1S^1$)	13.066 ($2P^2$) 11.715 ($1S^1$)	11.985 ($2P^1$)	11.757 ($2P^1$)	11.679 ($2S^22P^2$–$1S^1$) 12.081 ($2S^22P^2$–$1S^1$)	12.315 ($2S^22P^2$–$2P^2$)	12.632 ($2S^22P^3$–$1S^1$)	11.693 $2S^22P^2$– ($2P^3$–$1S^1$)	12.181 $2S^22P^2$– ($2S^22P^2$–$1S^1$)	12.173	0.07–7.08
III	17.132 ($1S^1$)	16.769 ($2P^2$) 17.435 ($2S^12P^1$)	16.747 ($2P^2$)	17.967 ($2P^2$)	C and H blocks	16.576 ($2S^22P^2$–$2P^4$)	Nand H blocks	C and NH_2 blocks	C and NH_2 blocks	17.104	0.16–4.92

Effect of specific local energy (electromagnetic fields, radiation, etc.) upon structural conformations can increasingly follow the pathological series II. It may be one of the reasons of normal functioning failure in biosystems, e.g., in oncological diseases. If so, some practical recommendations can be done, which come down to the necessity of converting the molecular hydrogen into the atomic one, e.g., through the interaction with hydroxyl OH group.

From Table 4 it is seen that the majority of atoms and radicals, depending on the bond types and bond lengths, have P_E-parameters of different series. When introducing the stem cells, it is important for the molecular hydrogen should not be present in their structures. Otherwise atoms and radicals can transfer into the series II and disturb the vital functions of the main first system.

Conclusion

1. It is demonstrated that corpuscular interactions flow along the potential gradient (principle of adding reciprocals of energies), and wave processes flow against the potential gradient (principle of algebraic addition of energies).

2. *P*-parameters of the first valence electron of atoms define the energy characteristics of stationary states (in normal state) under the condition of the maximum of wave processes.

3. Under the condition of the minimum of such interactions, the pathological (but not stationary) biostructures containing the molecular hydrogen can be formed.

References

[1]Rubin A. B., *Biophysics*, Book 1, *Theoretical biophysics*, Vysshaya shkola, Moscow, **1987**, 319.

[2]Dirac, P. A., *Quantum Mechanics*, Oxford University Press, London, **1935**.

[3]Anderson, P. W., in *Magnetism*, Vol. 1, Academic Press, New York, **1963**, 25.

[4]Blokhintsev, D. I., *Basics of quantum mechanics*, Vysshaya shkola, **1961**, 512.

[5]Korablev, G. A., *Spatial-Energy Principles of Complex Structures Formation*, Brill Academic Publishers and VSP, Netherlands, **2005**, 426.

[6]Eyring, G., Walter, J., Kimball, G., *Quantum chemistry*, Wiley and Sons, New York, London, **1948**, 528.

[7]Fischer C. F., Average-energy-of-configuration Hartree-Fock results for the atoms helium to radon, *Atomic Data and Nuclear Tables*, **1972**, *4*, 301-399. https://doi.org/10.1016/S0092-640X(72)80008-1

[8]Waber, J. T., Cromer, D. T., Orbital Radii of Atoms and Ions, *J. Chem. Phys.*, **1965**, *42*, 4116-4123. https://doi.org/10.1063/1.1695904

[9]Clementi, E., Raimondi, D. L., Atomic Screening Constants from SCF Functions, *J. Chem. Phys.*, **1963**, *38*, 2686-2689. https://doi.org/10.1063/1.1733573

[10]Korablev, G. A., Kodolov, V. I., Lipanov, A. M., Analog comparison of Lagrange and Hamilton Functions with a spatial and energy parameter, Khim. Fiz. Mezoshkopiya, (*Chem. Phys. Mesoscopy)*, **2004**, *6*, 5-18.

[11]Pidgainy, Yu. M., Morozova, V. M., Dudko, V. A., *Mechanics of Polymers*, **1967**, 1096-1104.

[12]Ayushev, T. Yu., *Geometric aspects of adaptive technology of producing structures by winding from fibrous composite materials*, BNC SO RAS Publishers, Ulan-Ude, **2005**, 212.

[13]Kodolov, V. I., *Polymeric composites and technology of producing aircraft engines from them*, Izhevsk Mechanical Institute, **1992**, 200.

[14]Korablev, G. A., Dynamics of rotational motions in macro- and microsystems, *Eur. Chem. Bull*., **2017**, *6(2)*, 79-82. DOI: 10.17628/ecb.2017.6.79-82.

[15]Korablev, G. A., *Spatial-energy parameter and its application in research*, LAP LAMBERT Academic Publishing, Germany, **2016**. 1-65.

Received: 10.04.2018.
Accepted: 10.11.2018.

EVALUATION OF MULTIPLEX PCR TECHNIQUES FOR KLEBSIELLA PRODUCING AMPC-β LACTAMASES IN CLINICALLY SIGNIFICANT *KLEBSILLA* ISOLATES

Iman M. A. El-Kholy[a], M. H. Abul-Aziz[b], Atef M. Diab[b] and Mona A. Rezk[a]*

Keywords: Multiplex PCR, cefoxitin resistant Klebsiella-AmpC β-lactamase.

Multiplex PCR for the detection of AmpC genes has proved useful as a rapid screening tool to distinguish cefoxitin resistant non-AmpC producers from cefoxitin resistant AmpC producers. In addition to AmpC gene detection, the data generated from the multiplex PCR method can distinguish which family of AmpC gene is present in the resistant organism thereby distinguishing possible inducible AmpC producers from non-inducible producers of AmpC. The present study was designed to evaluate these issues among cephalosporin-resistant isolates of *Klebsiella spp.* and to assess the performance characteristics of phenotypic tests, using different inhibitors, compared to the PCR, for their rapid and accurate detection. Fifty eight out of 100 isolates were AmpC producers by PCR. Fifty six out of 58 isolates that were positive by PCR test were resistant to FOX. Thirty out of 58 AmpC producers were ESBL positive by E- test and MDDST in detection of ESBL in the presence of AmpC. While 23 /58 were positive by DDST for detection of ESBL in presence of Amp. This study reveals high prevalence of pAmpC and ESBL enzymes among bacterial isolates from our hospital. ESBL production may mask the phenotypic detection of pAmpC enzymes. Modified 3 dimensional(M3D) is a simple and reliable method for detection of pAmpCs. MDDST serve as reliable confirmatory tests for detection of ESBLs in AmpC-positive isolates.

* Corresponding Authors
Fax:
E-Mail: monarezq24@yahoo.com
[a] Ain Shams University Hospital
[b] Suez Canal University, Faculty of Science

Introduction

Extended-spectrum beta-lactamases (ESBLs) and AmpC beta-lactamases (AmpCs) are important mechanisms of resistance among Enterobacteriaceae. Infections caused by ESBL and /or AmpC- positive bacteria are of particular clinical and epidemiological importance and cause higher patient morbidity and mortality.[1,2]

ESBLs are typically plasmid-mediated, clavulanate susceptible enzymes that hydrolyze penicillins, extended-spectrum cephalosporins and aztreonam. AmpCs are cephalosporinases that are poorly inhibited by clavulanic acid. They can be differentiated from ESBLs by their ability to hydrolyze cephamycins as well as other extended-spectrum cephalosporins. AmpCs were presumed to be chromosomally mediated but since the late 1980s they have disseminated on plasmids and now represent a substantial clinical threat. The emergence and spread of pAmpCs in Enterobacteriaceae has made their detection clinically relevant, particularly in bacterial species naturally lacking chromosomal cephalosporinase namely in *E.coli*, *Klebsiella* spp. and Proteus mirabilis. Detection a pAmpC in a strain with a coexisting ESBL is even more challenging.[3]. Moreover, AmpCs can interfere with ESBL detection particularly when using the current CLSI ESBL confirmatory tests. Resulting failures to detect ESBLs can endanger patients because false susceptibility to cephalosporins may be reported.[4] This warrants the need foran alternative ESBL confirmatory test of greater accuracy for AmpC-producing isolates.[5] At present, there are no guidelines or standardized phenotypic methods recommended for detection of AmpCs, though several methods have been described, including disc synergy assays using Amp-C inhibitors, a specific E test format for AmpC testing and a three-dimensional test. However, these methods are expensive, tedious and have not been systematically compared.[6,7] This prospective study was designed and conducted at in the Central Microbiology Laboratory of Ain Shams University Hospital in Egypt to (a) determine the prevalence of ESBLs and AmpC-producers among bacterial isolates with reduced susceptibility to extended spectrum cephalosporines and cephamycins of *Klebsiellae*, (b) to evaluate the efficacy of the modified double disc synergy test (MDDST) as confirmatory ESBL tests in AmpC–positive isolates and (c) to assess the performance characteristics of phenotypic tests compared to the PCR as a gold standard test for the rapid and accurate detection ofAmpCs in ESBL-positive and ESBL-negative isolates.

Experimental

Bacterial isolates

This study was done on 100 clinical isolates of *Klebsiella spp.* isolated from different clinical specimens referred to Microbiology Central Laboratory of Ain Shams University Hospitals Cairo, Egypt, for routine culture and sensitivity, from ICU, during a period of 3 months, from September to December 2015.

All Isolates have been subjected to the following tests: To screen for ESBLs production by disc diffusion method,[8] the antibiotic discs of CAZ (30 µg), CTX (30 µg), FEP (30 µg) and CPD (10 µg) were allowed to diffuse into the medium and interact in a plate freshly seeded with the test organisms

creating zones of inhibition that have been measured and interpreted according to Ref.[8] interpretive criteria for screening of ESBL.

Formation of zone diameters of CPD ≤17, CAZ ≤ 22 and CTX ≤27 mm indicates ESBL production that is positive screening for ESBL. However, FEP disc is not included by CLSI for ESBL screening and the FEP zone of diameter ≤14 mm indicates resistance which we consider as presumptive ESBL. To perform double disc synergy test using amoxicillin/ clavulanate (20/10 µg) and 3rd generation cephalosporin that is ceftazidime, cefotaxime, cefopodixime and cefepime,[9] a disc of AMC (20 µg amoxicillin + 10 µg clavulanic acid) and discs of CAZ, CTX, FEP and CPD were placed around AMC disc with a distance of 20 mm. Clear extension of the edge of the inhibition zone of cephalosporin toward the AMC disc shows positive result and interpreted as positive for ESBL production (Figure ESI 1). Negative result showed that no synergy is present (Figure ESI 2). To detect production of ESBLs by modified double disc synergy using FEP disc and piperacillin/tazobactam disc[10] a disc of TZP (piperacillin /tazobactam) (100/10 µg) was placed from FEP (30 µg) disc at a distance of 20 mm from it (centre to centre). Clear extension of the edge of the inhibition zone of FEP disc toward the TZP disc indicates a positive result and was interpreted as positive for ESBL production **(**Figure ESI3). Negative results showed that there is no synergy (Figure ESI4).

CLSI method using ceftazidime/ ceftazidime-clavulanate (CAZ-CLA) E-test ESBL strips.[8] The E-test ESBL strip is a plastic drug-impregnated strip, one end of which generates a stable concentration gradient of ceftazidime (MIC test range, 0.5-32 mg L^{-1}) and the remaining end of which generates a gradient of ceftazidime (MIC test range, 0.064-4 mg L^{-1}) plus 4 mg L^{-1} clavulanic acid. The MIC value was read from the scale in terms of µg mL^{-1} where the ellipse edge intersects the strip. ESBL production is inferred if the MIC ratio for cephalosporin alone/cephalosporin plus clavulanate MIC is ≥ 8 (Figure ESI5). ESBL production was also identified by the presence of a phantom zone or a deformation of the CAZ inhibition zone independent of the MIC ratios (Figure 1.) A MIC ratio of <8 is indicative of non ESBL production (Figure 2).

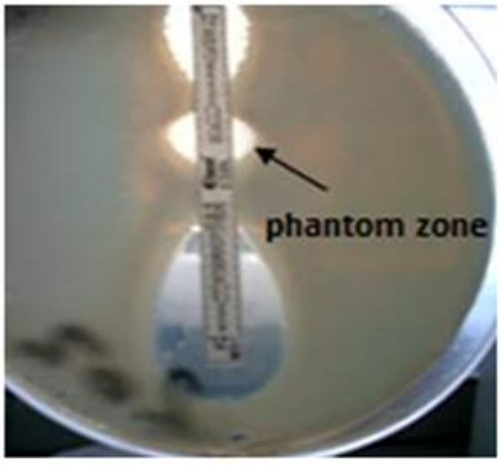

Figure 61. TZ = 32, TZL = 0.25 so TZ/TZL = 128, the ratio≥ 8 indicates a clear cut ESBL positive.

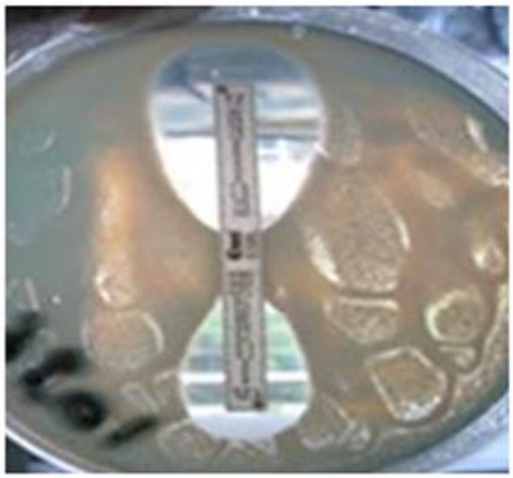

Figure 2. TZ = 0.5, TZL = 0.125 so TZ/TZL = 4, the ratio< 8 indicates aclear cut ESBL negative.

When MIC values were above the test device range, interpretation was 'non-determinable'.Screening for AmpC production by resistance to cefoxitin disc (30 µg).[9]

The antibiotic disc used FOX (30 µg) was allowed to diffuse into the medium and interact in a plate freshly seeded with the test organisms making zones of inhibition that have been measured and interpreted according to CLSI[8] interpretive criteria for screening of AmpC. Isolates showing diameter zone of inhibition ≤ 14mm were considered resistant (Figure ESI6.[11] Isolates showing diameter zone of inhibition > 14mm were considered sensitive (Figure ESI7).

Confirmation of production of AmpC was done by modified three-dimensional test.[12] This test detects the tested isolate which produce AmpC β-lactamase enzyme that isresistant to cefoxitin resulting in distortion of zone of inhibition of cefoxitin which is formed by *E. coli* ATCC 25922. Enhanced growth of the surface of the organism at the point where the slit intersected the zone of inhibition means a a positive result and is interpreted as evidence for the presence of AmpC β-lactamase (Figure ESI8. Isolates with no distortion are viewed as negative result and are recorded as non-AmpC producers (Figure ESI9).

Real-time PCR

DNA extraction

Cells were harvested in a microcentrifuge tube by centrifuging for 10 min at 5000 x g (7500 rpm). The supernatant liquid was discarded. Washing was done twice with Tris-EDTA buffer by centrifugation at 8000 rpm for 10 min. 20 µL proteinase K and 200 µL Buffer AL were added. Mixing was done thoroughly by vortexing and incubation was done at 56 °C for 20 min. 200 µL ethanol (96-100%) was added. Mixing was done thoroughly by vortexing. The mixture (including any precipitate) was pipetted into the DNA Mini spin column placed in a 2 mL collection tube. Centrifugation was done at ≥ 6000 x g (8000 rpm) for 1 min. Flow-through and collection tube were discarded. The DNA Mini spin column was placed in a new 2 mL collection tube. 500 µL Buffer AW1 was added and centrifugation was done

for 1 min at ≥ 6000 x g (8000 rpm). Flow-through and collection tube were discarded. The DNA Mini spin column was placed in a new 2 mL collection tube. 500 µL Buffer AW2 was added followed by centrifugation for 3 min at 20,000xg (14,000 rpm) to dry the DNA membrane. Flow-through and collection tube were discarded. The DNA Mini spin column was placed in a clean 1.5 or 2 mL micro centrifuge tube, and 100 µL Buffer AE was pipetted directly onto the DNA membrane. Incubation was done at room temperature for 1 min, and then centrifugation for 1min at ≥ 6000 x g (8000 rpm) to elute.

DNA amplification and detection

Reaction set-up

All solutions after thawing were gently vortexed and briefly centrifuged. A reaction master mix was prepared by adding the following components for each 25 µL reaction to a tube at room temperature (Table 1).

Table 1. Components of reaction master mix for each 25 uL reaction.

Reaction component	Volume µL	Concentration
Maxima® SYBR Green qPCR Master Mix (2X), no ROX	12.5	-
Forward Primer	0.75 (1:10)	0.3 µM
Reverse Primer	0.75 (1:10)	0.3 µM
Template DNA	5 (1:10)	-
Water, nuclease-free	6	-
Total reaction volume		-

The primers used were:

FOXMF: 5′AAC ATG GGG TAT CAG GGA GAT G 3′.

FOXMR: 5′CAA AGC GCG TAA CCG GAT TGG 3′.[13]

The master mix was mixed thoroughly and the appropriate volumes were dispensed into PCR tubes. The template DNA (≤ 500 ng/reaction) was added to the individual PCR tubes containing the master mix. Then the reaction mixture was mixed gently without creating bubbles (not to be vortexed) then centrifuged briefly (bubbles will interfere with fluorescence detection).

Table 2, Three-step cycling protocol

Step	Temperature, °C	Time	No. of cycles
Initial	95	10	1
Denaturation	95	15 s	40
Annealing	60	30 s	40
Extension	72	30 s	40

The thermal cycler was programmed according to the recommendations below, then the samples were placed in the cycler and we started the program. Data was taken during the extension step. Thermal cycling conditions are given Table 2.[14] The amplification program was followed immediately by a melt program consisting of 1 min at 95 °C, 30 sec at 55 °C then again to 95 °C for 30 s.

The greenish horizontal line in the graph (Figure 3) is the threshold line at which the fluorescence begins to be detected (The point at which the amplification plot crosses the threshold is the cycle threshold = *Ct*).[15] The T_m of samples which were identical or close to that of positive control were considered the gene of target as shown in Figure 4.

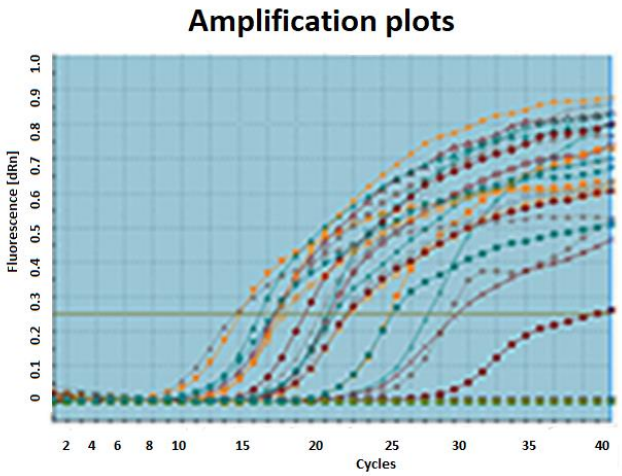

Figure 3. Results of Syber Green real-time PCR in amplification plot with cycles number on x axis and fluorescence on y axis.

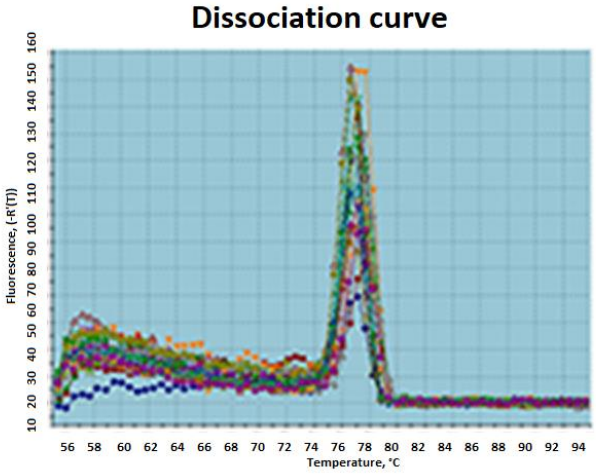

Figure 4. Results of melting curve, average T_m = 77.13 °C - 77.72 °C.

Results

Fifty eight out of 100 isolates were AmpC producers by PCR (golden standard test). Fifty six out of 58 isolates that were positive by PCR test were resistant to FOX with a sensitivity of 96.6 % and specificity of 52.4 % for detection of AmpC production with positive predictive value and negative predictive value of (73.7 % and 91.7 %) respectively. There was moderate agreement between the results of both tests (Table 3).

Table 3. Comparison between Cefoxitin screening test and PCR test for AmpC detection.

		Fox screening test		
		R	***S***	**Total**
PCR	Positive	56 (96. 6%)	2 (3.4 %)	58
	Negative	20 (47.6 %)	22 (52.4 %)	42
Total		76	24	100

Thirty out of 58 AmpC producers were ESBL positive by E-test and MDDST with a sensitivity and specificity of 100 % in detection of ESBL in the presence of AmpC (Table 4). While 23/58 were positive by DDST showing 76.7 % sensitivity and 100 % specificity for detection of ESBL in presence of AmpC with positive predictive value and negative predictive value of (100 % and 80 %) respectively (Table 5). There was substantial agreement between results of both the tests.

Table 4. Comparison between MDDST and E-test when PCR test is positive.

PCR positive		**MDDST**		
		Positive	**Negative**	**Total**
E-test	Positive	30 (100%)	0 (0%)	30
	Negative	0 (0%)	28 (100%)	28
Total		30	28	58

Table 5. Comparison between DDST and E-test or MDDST when PCR test is positive.

PCR Positive		**DDST**		
		Positive	**Negative**	**Total**
E-test or MDDST	Positive	23 (76.7 %)	7 (23.3 %)	30
	Negative	0 (0%)	28 (100 %)	28
Total		23	35	58

Forty-two out of 100 isolates were negative Ampc by PCR test. Thirty two out of 42 clinical isolates were positive ESBL by both E-test and MDDST showing (100 %) sensitivity and specificity in detection of ESBL in absence of AmpC (Table 6). While, 29/42 (69.05 %) were positive by DDST showing 90.6 % sensitivity and 100% specificity of detection of ESBL in absence of AmpC. The positive predictive value and negative predictive value was (100 % and 76.9 %) respectively (Table 7). There is a substantial agreement between results of both the tests.

Table 6. Comparison between MDDST and E-test when PCR test is negative.

PCR Negative		**MDDST**		
		Positive	**Negative**	**Total**
E-test	Positive	32 (100 %)	0 (0 %)	32
	Negative	0 (0 %)	10 (100 %)	10
Total		32	10	42

Discussion

The importance of detecting AmpC-producing isolates is highlighted by data showing high clinical failure rates when AmpC-producing strains of *K. pneumoniae* are treated with cephalosporin agents or the subsequent development of antibiotic resistance in such strains.[16] By antibiotic susceptibility testing it might be difficult to distinguish ESBL-producing organisms from plasmid AmpC-producing organisms because of their similar resistance. Distinguishing between AmpC- and ESBLproducing organisms has epidemiological significance and has therapeutic importance as well.[17]

Table 7. Comparison between DDST and E-test or MDDST when PCR test is negative.

PCR Negative		**DDST**		
		Positive	**Negative**	**Total**
E-test or MDDST	Positive	29 (90.6 %)	3 (9.4 %)	32
	Negative	0 (0 %)	10 (100 %)	10
Total		29	13	42

In Egypt, one study assessed AmpC production among *Enterobacteriaceae*,[18] however, molecular techniques were not attempted. So, little is known about the genetic background of AmpC-producing isolates in Egypt.

Results of the present study showed that the prevalence of *ampC* genes in 58/100 isolates of the selected species was 30/58(51.7%) whereas ESBL-producers were detected. AmpC prevalence was lower than that reported by El-Hefnawy[18] from Egypt (34 % in 50 *K. pneumoniae* and *E. coli* isolates), but it was equivocal with another study from Singapore (26 % in 255 clinical isolates of *E. coli*, *Klebsiella* spp. and *P. mirabilis*). In the first study, molecular techniques were not attempted and they used one phenotypic test, the three dimensional test (TDT), while in the second study both TDT and the multiplex PCR were used.[19] These results were much higher than those reported in other parts of the world; in Spain (0.43%),[20] in China (2.79 %)[21] and in USA (3.3 %).[22] This may be due to the differences in the study population and the epidemiological differences in various geographic regions.

The high prevalence of AmpC producers in our study could be explained by 2 points: First, the prevalence of ESBL-production was high (62 %) and many of our *ampC*-positive isolates were also ESBLproducers30/58 (51.7 %). Previous Egyptian studies have also reported the high prevalence of ESBLs in Egypt;38 %,[23] 61 %[24] and 65.8 %.[25] It has been recently found that infection with pAmpCproduceris frequently associated with a high copresencerate of ESBLs.[17] Second, our specimens were collected from patients admitted to ICU, it could be expected that they have been exposed to previous cephalosporin therapy whether empirically or according to the hospital antibiotic policy or due to unjustified courses as reported in a previous Egyptian study by El-Kholy.[23] Knowing that selective-pressure produced by the extensive use of oxyimino-cephalosporins are among the driving forces of increasing the prevalence of AmpC- production,[17] the high rate of AmpC production could be anticipated.

In our study 30/58 (51.7%) of the isolates were both AmpC and ESBL-positive by molecular detection methods. This rate was higher than that reported from western parts of the world: 7/117 (6%) in Spain,[20] 4/81 (4.9 %) in Minnesota in USA.[26] Interestingly, 58/62 (93.5 %) of our ESBL-positive *Klebsiella* spp. was Amp*C*-positive. This rate is comparable with that reported in India as Vandana and Honnavar[27] detected AmpC in 39/52 (75 %) of ESBL-producing isolates of *K.pneumoniae.* As both ESBL and AmpC β-lactamases may coexist, therefore their detection is difficult because they mask each other. In the present study, all 30 ESBLproducers in AmpC-positive isolates were successfully identified by using the MDDST, in which FEP and TZP were utilized in approximation, implying that the use of this phenotypic method could overcome the masking effect of AmpC on phenotypicdetection of ESBLs. Similar observation has been reported by Khan[9] and Fam and El-Damarawy.[25]

Use of a cefoxitin disk is useful in screening for AmpC but it is non-specific. In our study only 58/64 of cefoxitin-resistant isolates had *ampC* genes. Several factors may explain resistance to cefoxitin in the AmpC-negative isolates: First, it may arise due to porin channel alterations and mutations as previously reported in *Klebsiella* spp. isolates.[3,16] Second, cefoxitin-resistance phenotype in *Klebsiella* spp. can result from over expression of the chromosomal *ampC* gene due to mutations in the promoter or/and attenuator regions resulting in alterations in the permeability of the cell to cefoxitin or a combination of all thesefactors.[26] Third, cefoxitin has been demostrated as a substrate to active efflux pump in clinical isolates.[27]

In conclusion, this study has revealed the occurrence of plasmid mediated AmpC beta-lactamase producing strains in clinically important bacterial isolates for the first time in our region. ESBL production may mask the phenotypic detection of pAmpC enzymes. MDDST is a simple and reliable method serve as reliable confirmatory tests for detection of ESBLs in AmpC positive isolates. Occurrence of a large percentage of multidrug resistant strains has been observed. As AmpC beta-lactamase production is frequently accompanied by multidrug resistance, so conjugative dissemination of this AmpC beta -lactamase encoding plasmids may facilitate the spread of resistance against a wide range of antibiotics among different members of *Enterobacteriaceae.* Imipenem is superior to other antibiotics for the treatment of serious infections due to AmpC beta-lactamase-producing enterobacteria.

References

[1]Livermore D. M., Current Epidemiology and Growing Resistance of Gram-negative Pathogens, K*orean J. Int. Med.*, **2012,** *27*, 128-142. doi:10.3904/kjim.2012.27.2.128

[2]Maina D., Revathi G., Kariuki S., Ozwara, H**.,** Genotypes and cephalosporin susceptibility in extended-spectrum β-lactamase producing Enterobacteriaceae in the community. *J. Infect. Dev. Ctries*, **2012,** *6(6)*, 470-477.DOI:10.7243/2052-6180-1-5

[3]Philippon A., Arlet, G., Jacoby, G. A.,Plasmid-determined AmpC-type β-lactamases. *Antimicrob. Agents Chemother.*, **2002,** 46(1), 1–11. doi: 10.1128/AAC.46.1.1-11.2002

[4]Thomson K. S. Controversies about extended-spectrum and AmpC β-lactamases. *Emerg. Inf. Dis.*, **2001,** *7(2),* 333-336.

[5]Munier G. K., Johnson C. L., Snyder J. W. Moland, E. S., Hanson, N: D., Thomson, K. S., Positive extended-spectrum-β-lactamase (ESBL) screening results may be due to AmpC β-lactamases more often than to ESBLs. *J. Clin. Microbiol.* **2010,** 48, 1019-1025. doi: 10.1128/JCM.01544-09

[6]Kanamori, H., Yano, H., Hirakata, Y., Endo, S., Araim K., Ogawa, M., Shimojima, M., Aoyagi, T., Hatta, M., Yamada, M., Nishimaki, K., Kitagawa, M., Kunishima, H., Kaku, M., Molecular Characteristics of Extended-Spectrum β-Lactamases and qnr Determinants in Enterobacter Species from Japan. *PLoSONE* **2012,** *7(6),* e37967. DOI: 10.1093/jac/dkr283

[7]Sabia, C., Gargiulo, R., Sarti, M., Evaluation of a Double Synergy Differential Test (DSDT) for differential detection of ESBL and AmpC-type β-lactamases in Escherichiac oli, Klebsiella pneumoniae and Proteus mirabilis, *New Microbiol.*, **2012,** *35*, 221-225.

[8]CLSI: Clinical laboratory standards institute. Performance standards for antimicrobial susceptibility testing; nineteenth information supplement. M100–S19. **2009,** *9(3),* Wayne, Pennsylvania (USA). doi: 10.1371/journal.pone.0079130

[9]Khan, M. K., Thukral, S. S. and Gaind, R., Evaluation of a modified double disc synergy test for detection of extended spectrum β-lactamases in AmpC β-lactamase-producing P*roteus mirabilis. Indian J. Med. Microbiol.;***2008,** *26*, 58-61.

[10]Pitout J. D., Reisbig, M. D., Venter, E. C., Church, D. L. and Hanson, N. D. Modification of the double disc test for detection of *Enterobacteriaceae* producing extended spectrum and AmpC β-lactamases. *J. Clin. Microbiol.*, **2003,** *41*, 33-39.

[11]Clinical and Laboratory Standards Institute (CLSI,): Performance standards for antimicrobial susceptibility testing, twenty-second informational supplement. CLSI document M100-S22. Wayne, PA: Clinical and Laboratory Standards Institute. **2012**

[12]Shahid, M., Malik, A., Agrawal, M. and Singhal S., Phenotypic detection of extended-spectrum and AmpC β-lactamases by a new spot-inoculation method and modified three-dimensional extract test: comparison with the conventional three-dimensional extract test. *J. Antimicrob. Chemother*. **2004,** *54*, 684-687. DOI:10.1093/jac/dkh389

[13]Péréz-Péréz, F. J., Hanson, N. D., Detection of plasmid mediated AmpC β-lactamase genes in clinical isolates by using multiplex PCR. *J. Clin. Microbiol.*, **2002,** *40(6),* 2153-2162.doi:10.1128/JCM.40.6.2153-2162.2002

[14]Ergin, A., Koseoglu, Eser, Ö. K., Hascelik, G., Erythromycin and penicillin resistance mechanisms among viridans group *streptococci* isolated from blood cultures of adult patients with underlying diseases. *New Microbiol.*, **2011,** *34*, 187-193.

[15]Muldrew K. L., Molecular diagnostics of infectious diseases. *Current Opinion Pediat.*; **2009,** 21, 102–111. doi:10.1097/MOP.0b013e328320d87e

[16]Jacoby G. A., AmpC β-lactamases. *Clin. Microbiol. Rev.*, **2009,** 22(1), 161-182. doi: 10.1128/CMR.00036-08

[17]Park, Y. S., Yoo, S., Seo M., Kim, J. Y., Cho, Y. K., Pai, H., Risk factors and clinical features of infections caused by plasmid-mediated AmpC β-lactamase producing *Enterobactriacae. Int. J. Antimicrob. Agents*, **2009,** 34, 38-43. doi: 10.1016/j.ijantimicag.2009.01.009

[18]El-Hefnawy N. N., Phenotypic detectionof AmpC β-lactamase in Gram-negative bacteria. Thesis submitted for partial fulfillment of Master degree in Clinical and Chemistry Pathology, Faculty of Medicine, Ain Shams University.**2008.**

[19]Tan T. Y., Ng, S. Y., Teo L., Koh, Y., Teok, C. H., Detection of plasmid-mediated AmpC in *Escherichia coli, Klebsiella pneumoniae* and *Proteus mirabilis*. *J. Clin. Path.*, **2008,** 61, 642-644. DOI: 10.1136/jcp.2007.053470

[20]Mata C., Miro, E., Rivera, A., Mirelis, B., Coll, P., Navarro, F., Prevalence of acquired AmpC β-lactamases in *Enterobacteriacae* lacking inducible chromosomal *ampC* genes at a Spanish hospital from 1999 to 2007. *Clin. Microbiol. Infect.*, **2009,** *16(5),* 472-476**.** doi.org/10.1111/j.1469-0691.2009.02864.x

[21]Li Y., Li Q., Du Y. Jiang, X., Tang, J., Wang, J., Li? G., Jiang, Y., Prevalence of plasmid-mediated AmpC β-lactamases in a Chinese university hospital from 2003 to 2005: first report of CMY-2-type AmpC β-lactamase resistance in *China. J. Clin. Microbiol*. **2008,** 46, 1317–1321. doi: 10.1128/JCM.00073-07

[22]Moland E. S., Hanson N. D, Black J. A., Hossain, A., Song, W., Thomson, K. S., Prevalence of newer β-lactamases in Gram-negative clinical isolates collected in the United States from 2001 to 2002. *J Clin Microbiol*., **2006,** 44(9), 3318-3324. DOI:10.1128/JCM.00756-06

[23]El-Kholy A., Baseem, H., Hall, G. S., Procop, G. W., Longworth, D. L., Antimicrobial resistance in Cairo, Egypt 1999-2000::*a survey of five hospitals. J. Antimicrob. Chemother*., **2003,** 51, 625-630. PMID: 12615864

[24]Al-Agamy M. H., Ashour M. S., Wiegand I. I., First description of CTX-M β-lactamase-producing clinical *Escherichia coli* isolates from Egypt. *Int. J. Antimicrob. Agents*, **2006, 27,** 545-548. doi: 10.1186/1471-2334-9-84

[25]Fam N.S. and El-Damarawy M. M., CTX-M-15 extended spectrum β-lactamases detected from intensive care unit of an Egyptian medical research institute. *Res. J. Med. Sci*., **2008,** *3(1),* 84-91. doi:10.4172/2329-8731.1000156

[26]Kohner P. C., Robberts, F. J., Cockerill, III F. R., Patel, R., Cephalosporin MIC distribution of extended-spectrum-β-lactamase and pAmpC-producing *Escherichia coli and Klebsiella species. J. Clin. Microbiol*, .**2009,** *47(8),* 2419-2425.doi: 10.1128/JCM.00508-09

[27]Vandana K E, Honnavar P., AmpC b-Lactamases among ESBL Producing *Escherichia Coli* and *Klebsiella Pneumoniae*-if you don't look, you won't find. J. Clin. Diagn. Res., **2009,** 8(3), 1653-1656.

[26]Mulvey, M. R., Bryce, E., Boyd, D. A. Ofner-Agostini, M., Land, A. M., Simor, A. E., Paton, S., Molecular Characterization of Cefoxitin-Resistant *Escherichia coli* from Canadian Hospitals. Antimicrob Agents Chemother. **2005,** *49(1),* 358-365. DOI:10.1128/AAC.49.1.358-365.2005

[27]Pages, J-M., Lavigne, J-P., Leflon-Guibout, V., Marcon? E., Bert, F., Noussair, L., Nicolas-Chanoine, M.-H., Efflux Pump, the masked side of ß-lactam resistance in *Klebsiella pneumonia* clinical isolates. PLoS ONE **2009,** 4(3), e4817.doi.org/10.1371/journal.pone.0004817

Received: 30.04.2018.
Accepted: 10.12.2018.

SUCCESSFUL LANDFILL LEACHATE WASTEWATER TREATMENT USING THE SEQUENCE OF OZONATION, ADSORPTION ON CHARCOAL AND PHOTO-OZONOLYSIS

Franco Cataldo[a]*

Keywords: landfill leachate; ozone; adsorption; activated carbon; photo-ozonolysis; pilot plant

Landfill leachate derived from the landfilling practice of the municipal wastes is a problem affecting all countries and continents. Even after the shutdown of a landfill site, the leachate production continues for decades. In this work a solution for the landfill leachate treatment has been proposed based on three fundamental steps: the pre-ozonolysis of the leachate, the passage of the ozonized leachate through a fixed bed of activated carbon and the final step consisting in a photo-ozonolysis stage involving the simultaneous action of ozone and UV light. A distinction between the chemical structure and chemical behaviour of young and mature leachate was evidenced by thermal analysis of the soluble organic matter (SOM) obtained from these substrates. Furthermore, a distinction between young and mature leachate was also evidenced in terms of their different reactivity toward ozone as illustrated by the COD abatement and by FTIR spectroscopy on pristine and ozonized SOM. A modular pilot plant for the treatment of different landfill leachates was presented and proposed.

* Corresponding Authors
E-Mail: franco.cataldo@fastwebnet.it
[a] Actinium Chemical Research Institute, Via Casilina 1626A, 00133 Rome, Italy

Introduction

Landfilling of municipal wastes is a usual disposal practice common throughout the entire world[1-5] One of the main problems linked to the municipal waste landfilling is the production of landfill leachate, a problem which persists for several years even after the landfill site is shut down.[1-5] The landfill leachate derives from the fermentation of the organic matter present in the municipal wastes which lead to decomposition products which are washed out and diluted by the meteoric precipitations. The landfill leachate does not have a stable chemical composition but undergoes a gradual composition evolution also affected by the local environmental and weather circumstances.[1-5] The young leachate is characterized by a mixture of organic matter with low molecular weight, it is in large part biodegradable and it is the result of the initial rapid aerobic fermentation with the liberation of CO_2, H_2 and the production of free carboxylic acids so that all locally available oxygen is consumed.[1-5] The end of the aerobic fermentation can be evidenced by a peak in COD and BOD level and the accumulation of ammonia/ammonium ion and chlorides. Then the anaerobic fermentation prevails, a stage which is also called methanogenesis due to the production and release of methane accompanied by CO_2 .[1-5] A slow gradual decline in COD and BOD level can be observed toward limiting values. Aged leachate is characterized by stabilized values of COD and by alkalinity in contrast with the acidic properties of the young leachate. The most interesting feature of aged or mature leachate is the fact that its soluble organic matter is recalcitrant any to biological-based oxidation process and it is necessary to proceed with strong oxidation processes to get rid of it. On the other hand the young landfill leachate presents the advantage of being more easily degradable either by biological oxidation-based processes as well as by chemical processes.[1-5] The toxicity of landfill leachate is certainly due to the high ammonia level and chlorides but moreover by the richness of the dissolved transition metals whose origins derive from the corrosive nature of landfill leachate which slowly dissolves metals from the soil mixed with the wastes and from any metallic debris present in the landfilled wastes.[6] Additional undesired components found in landfill leachate are the so-called xenobiotics, i.e. substances originating from household or industrial chemicals and present in relatively low concentrations. Despite the transition metals ions and the xenobiotics, the leachate is anyway toxic because it is a broth of bacteria and nutrients and of course any adventitious pathogen can survive and reproduce in such a medium.[6] Thus, the basic idea of the pre-ozonation treatment presents many benefits. Among the solutions for the treatment of landfill leachate, the ozone treatment was proposed by numerous authors.[7-18] Initially it was mainly proposed as the stabilizer of the leachate properties,[13] but later it was recognized the benefits of ozonation (or other oxidation processes) to facilitate the biological treatment.[8] The fact that landfill leachate is composed by refractory organic matter led the researchers to apply a series of advanced oxidation processes in its treatment.[9] However the benefits of the ozone pre-treatment of the landfill leachate became evident already several years ago and in more recent years the efficiency of such pre-treatment process was brought to the highest level so that about 3 mg O_3 per mg of COD were necessary to reduce by 50% to starting COD level of a landfill leachate.[9-12] Concrete benefits were also obtained by landfill leachate pre-ozonation with a drastic cut of the COD, followed by

activated carbon adsorption.[13] With this approach the adsorption efficiency of the activated carbon is considerably enhanced thanks to the pre-ozonation of the leachate.[14] Furthermore, the leachate biodegradability is enhanced by the pre-ozonation and the perozonation[14] but also the reverse approach was studied with the biological digestion of the leachate, followed by ozonation.[16] The latest trends involve the use of catalytic ozonation of the leachate in the presence of suitable oxides.[16,17,18] In this paper, after a brief review of the organic matter present in the landfill leachate with a clear distinction between young and old landfill leachate, and an analysis of certain properties, we will focus on the results regarding the landfill leachate treatment with ozone followed by activated carbon and completed by a photo-ozonolysis.[19,20,21]

Experimental

Materials

Young and old landfill leachate were collected with the aid of the plant manager of the municipal landfill site located at about 70 km south of Rome. The young and old landfill leachate samples were analyzed immediately after transportation to the Actinium laboratory. Table 1 shows the analytical results.

Table 1. Analytical results on pristine samples of young and old landfill leachate samples.

	Young leachate	Old leachate 1	Old leachate 2
COD mg L^{-1}	9200	1850	3135
Fe^{2+}, mg L^{-1}	11.7	13.3	9.79
NH_4^+, mg L^{-1}	132	214	171
Cl^-, mg L^{-1}	2140	2530	2400
pH	6.2	9.0	8.8

Methods

Isolation of the soluble organic matter (SOM) from young leachate and its TGA and FT-IR

Young leachate (500 ml) was distilled in a spherical flask under reduced pressure in a water bath kept at 95°C. The distillation residue is bituminous, sticky and viscous solid which stinks terribly. The distillation residue was sampled and submitted to a thermogravimetric analysis with simultaneous differential thermal analysis at a heating rate of 10°C/min under air flow in a Linseis apparatus model L81.

Another sample was analyzed at the FT-IR spectrometer Nicolet 6700 from Thermo-Fischer. The spectra were collected in reflectance mode on ZnSe plate and transformed in normal absorbance spectra through the spectrometer's Omnic software.

Isolation of the soluble organic matter (SOM) from young leachate and its TGA and FT-IR

The same procedures described in the above paragraph for the young leachate were also performed on old leachate 1 sample.

Ozonation of the young leachate

A series of experiments were performed by treating the young leachate batch-wise in a 2 L round-bottomed flask which was filled with 500 ml of the leachate, evacuated and filled with O_3/O_2 mixture to reach a ratio mg O_3/mg COD = 0.22. After shaking and suitable contact time the COD dropped from the initial value of 9200 mg L^{-1} to 7830 mg L^{-1}. After the ozone treatment, all the water of the ozonized leachate was distilled off under reduced pressure in a water bath at 95°C leaving a dry residue which was collected for the FTIR analysis. In another experiment performed in conditions similar to those just described a mg O_3/mg COD = 0.35 ratio was reached after a suitable contact time and the COD dropped from the initial value of 9200 mg L^{-1} to 4205 mg L^{-1}.
In another experiment, a tubular reactor with a fritted glass porous septum was loaded with 300 ml of young leachate acidified to pH = 5. Ozone produced at a rate of 5g/h was bubbled through the liquid at a flow rate of 4.5 L min^{-1} for 19 min. This condition corresponds to mg O_3/mg COD = 0.58 and after this treatment the COD dropped to 1360 mg L^{-1}.

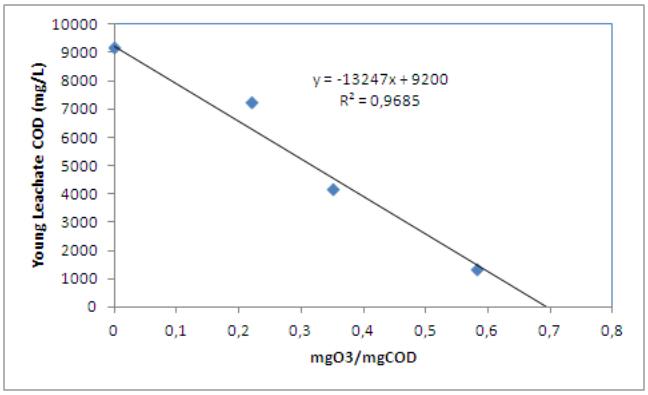

Figure 1. Pre-ozonization of young landfill leachate. The residual COD is a function of the ozone dose expressed as (Leachate COD) = -13247 (mg O_3/mg COD)+9200

The data in Fig. 1 are a summary of these results. From the graph of Fig. 1, it is possible to extrapolate that with mg O_3/mg COD $\geq$ 0.70 ratio one could get rid of the SOM in the young leachate.

Ozonation of the old leachate

Also for the old leachate, a series of experiments of pre-ozonation were performed either batchwise or through the tubular reactor in a continuous ozone flow, as described in

the above section for the young leachate. The ozone dose is expressed as in the previous section as mgO_3/mgCOD. The mg COD refers to the starting COD level. The refractory nature of the old leachate is immediately evident in Fig. 2: even with mg O_3/mg COD > 1 the COD abatement is unsatisfactory. It is also worth a comparison between the slope of Fig.1 with that of Fig. 2. The slope of the former is more than 12 times more steeply than that of the latter. Fig. 2 also shows the results of the old leachate ozonation in the presence of 10% by weight of neutral activated alumina, type 507C Brockmann-I having a particle size below 150 mesh and pore diameter of 5.8 nm.

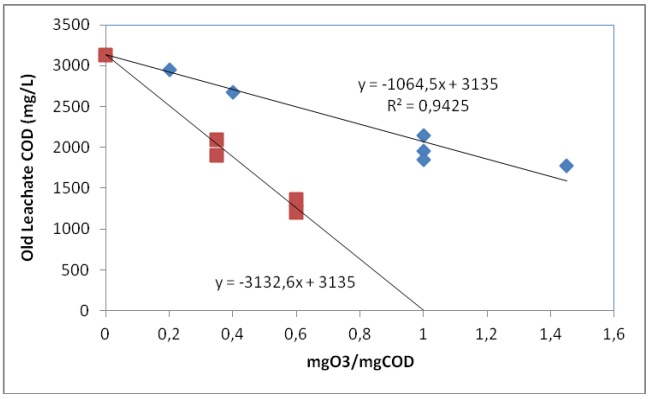

Figure 2. Pre-ozonization of old landfill leachate. The residual COD is a function of the ozone dose expressed as (leachate COD) = -1064 (mg O_3/mg COD)+3135 (blue diamonds); The leachate ozonation in the presence of activated Al_2O_3 gives a threefold acceleration in the COD abatement (red squares).

The results are quite interesting, although it should be noted that even without ozonation alumina is able to reduce the COD of the old leachate from the initial 3135 mg L^{-1} to 2100 mg L^{-1} by simple adsorption process. Fig. 2 shows that 10% alumina with an ozone dose of 0.6 mg O_3/mg of COD gives a decisive advantage. As shown in Fig. 2, the extrapolation of these data suggests that at mg O_3/mg of COD ≥ 1.0 the total initial COD of the old leachate could be removed, although further work is needed to verify this extrapolation.

Adsorption through an activated carbon bed

Once pre-ozonized, especially the old leachate needs further treatments which cannot be limited only to the ozonization. As detailed in the patents,[19,20,21] the pre-ozonized old leachate is passed through a fixed bed of granular activated carbon to reduce further the COD and make the leachate transparent to UV light and hence suitable for the photo-ozonolysis step of the final process.

Photo-ozonolysis

The photo-ozonolysis step is the final step process in the leachate treatment, when it is completely transparent to UV light. In this process complete sterilization is also achieved. Furthermore, the COD is further reduced within the desired law limits for the discharge in the sewage or ponds or the surface waters. The detail of the process can be found in ref.[19,20,21]

Results and Discussion

The key problem of the landfill leachate treatment is represented by the soluble organic matter which has been fractionated into three main components, i.e. humic and fulvic acids as well as the hydrophilic fraction.[1] The chemical structure of humic and fulvic acids from landfill leachate is rather complex and not univocal.[22,23,24] It must be described by model structures because its complexity, exactly in the same way as for the humic and fulvic acids extracted from soils and lake sediments.[25,26] In other words, it is completely reasonable to assume for the humic and fulvic matter from landfill leachate a structural analogy with that extracted from soil and other fluvial or lake sediments. This assumption is anyway substantiated by a series of experimental data.[1-5,22-24,25,26]

In this context, it is particularly interesting a comparison of the soluble organic matter (SOM) derived from young landfill leachate against aged or mature leachate. Many authors have insisted on this specific point regarding the biodegradability of the former and the refractoriness toward oxidation of the latter as well as the H/C, O/C and N/C ratios and the BOD/COD ratios, showing that by passing from young to mature leachate it is increased the aromatic content, the molecular weight, the carbon content and BOD/COD → 0. Indeed, the refractoriness toward oxidation of mature leachate is underlined by our studies on the radiolysis of the landfill leachate, which were surprisingly unsuccessful in terms of COD abatement.[27,28]

We have had the opportunity to isolate the SOM of a young and old leachate samples in a landfill located at about 70 km south of Rome. Fig. 3 shows the thermogravimetric analysis (TGA) of these two SOM performed in air flow. The SOM from young landfill leachate when heated in air shows a linear weight loss up to 328°C (-10% by weight). Above that temperature the differential thermal analysis (DTA) performed simultaneously to the TGA shows a strong exothermal peak due to partial combustion of the SOM (compare Fig.3 with Fig.4). The DTA peak in Fig. 4, occurs at 416°C accompanied by a secondary feature at 428°C. At the end of the combustion process, i.e. above 600°C the total weight loss undergone by the SOM of the young leachate is -37.8% measured at 600°C. At 580°C the DTA registers an endothermal transition due to the melting or thermal decomposition of a mineral component.

As shown in Fig. 3 and 4, the thermal behavior of a SOM from mature, old leachate heated in the air is completely different than that of young leachate without any abrupt weight loss. In fact, the SOM from old leachate shows a general and gradual trend to weight loss with a total weight loss of -28.5% at 750°C. However, the corresponding DTA reported in Fig. 4 is richer in transitions than those observed in the case of the young leachate. In fact, the SOM from old leachate shows two endotherms already at 86°C and at 154°C partially associated with trapped water evaporation. Then two main exothermal peaks are observed at 253°C and at 524°C and two much smaller exothermal transitions are

detected at 280°C and at 334°C. However, these DTA exothermal transitions have a limited impact on the TGA curve. For example, to the exothermal peak at 253°C corresponds a weight loss on only 4.4% and to the other exothermal peak at 524°C, it corresponds a local weight loss of 3.2%. Thus, at these temperatures are volatilized or burned really small amounts of the SOM fractions from old leachate.

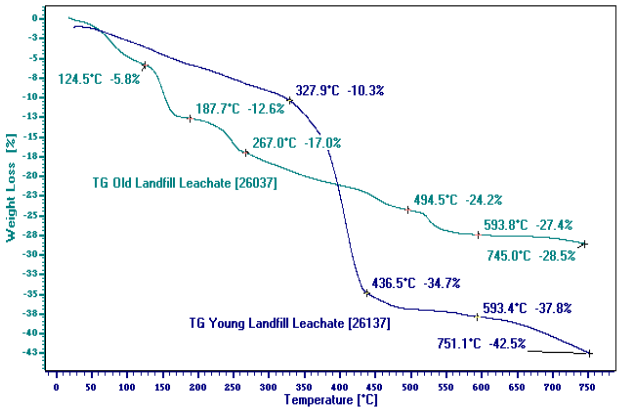

Figure 3. TGA in the airflow of the organic matter from young leachate (dark blue line) and from old leachate (light blue line).

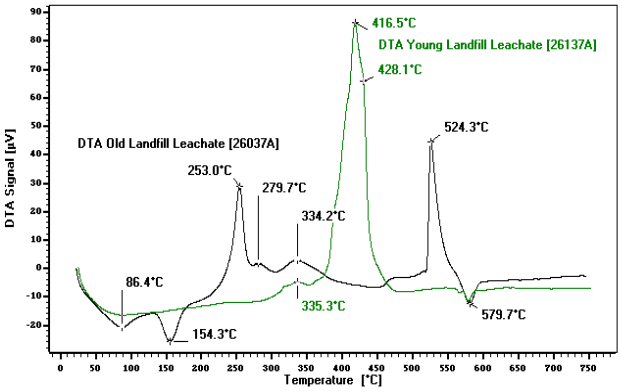

Figure 4. DTA in the airflow of the organic matter from young leachate (green line) and from old leachate (black line).

In summary, in Fig. 3 is shown very clearly the differences between the SOM from a young and old leachate. The former indicates an abrupt weight loss above 327 °C and the total weight loss at 750 °C is -42.5 % against -28.5 % at the same temperature of the SOM from old leachate. From these results a clear difference in the thermal behaviour and oxidation, also emerges the radical chemical difference between SOM from young and old leachate, with the latter being much less volatile due to the higher molecular weight and much less oxidizable than the former.

It is also interesting to discuss shortly the changes in the FT-IR spectra observed in the SOM from a young and old leachate. The young leachate is much reactive with ozone than the old leachate. Fig. 5 shows that the ozonation removes almost completely the infrared band at 1563 cm^{-1} which is one of the most intense bands in the pristine spectrum of young leachate. In fact, after ozonation the original band at 1563 cm^{-1} is reduced to a small shoulder at 1550 cm^{-1}. The infrared absorption band at 1563 cm^{-1} could be due to aromatic rings, to carboxylic acid salts or to unsaturated diketones and similar structures which give rise to the keto-enol tautomerism, i.e. the –CO-CH_2-CO- type of structures.[29]

Because of the fast and effective reaction with ozone, in the young leachate the band at 1563 cm^{-1} can almost certainly assign to highly substituted aromatic rings and/or to unsaturated diketones, since neither ketones and aldehydes, nor the carboxylic acid salts show a so special reactivity toward ozone.

On the other hand, Fig. 6 shows the FTIR spectrum of SOM from old landfill leachate. The spectral difference with the young leachate, at least limited to the samples we have studied, are relatively small. However, the SOM from old leachate shows a prominent infrared band at 1570 cm^{-1} with two shoulders at 1589 and 1668 cm^{-1}. In the case of mature leachate the ozone treatment does not affect significantly the band at 1570 cm^{-1}. Consequently, in a mature leachate this infrared band belongs mainly to non-oxidizable aromatic rings. This time the results of ozonation is the growth of the bands at 1665 and 1715 cm^{-1}, a clear sign of the slow oxidation which leads to ketone and carboxylic groups. Furthermore, the band originally at 1570 cm^{-1} and relatively sharp, broadens and is shifted at 1583 cm^{-1}.

The results of the infrared study matches perfectly with the COD abatement by leachate pre-ozonation. More in detail, the young leachate responds very well to the pre-ozonolysis as shown in Fig. 1, even with a relatively small ozone dose it is possible to reduce drastically the COD content of a young leachate. Fig. 1 suggests also that an opportunely calibrated ozonation could remove completely the COD of a young leachate. It is only a matter of costs and practical convenience to decide to which level the pre-ozonation of a young leachate should be pushed and then followed eventually by activated carbon adsorption and finished by a short photo-ozonolysis step to reach the limiting COD level required by law to discharge the treated water.

The infrared study has shown that the old leachate is oxidized but not mineralized by the ozonation as it happens for a young leachate. Indeed, Fig. 2 shows that the pre-ozonolysis of the old leachate is at least more than 12 times less effective in COD abatement than the case of a young leachate. This is indeed due to the presence of refractory SOM in the old leachate. Some evident benefit is offered by the pre-ozonation of the old leachate in presence of activated alumina. Alumina is able to adsorb the SOM of old leachate, but the combined alumina and ozone action on old leachate presents clear merits as shown in Fig. 2 and deserves further investigations. Probably, ozone oxidizes the SOM adsorbed on the alumina surface with higher efficiency than the direct ozone treatment of the old leachate without alumina catalyst. It is plausible to think that on alumina surface in presence of water, ozone decomposes into OH free radicals and this may justify the observed higher efficiency of ozone in the degradation of the SOM from old leachate. Even in the hypothesis that the surface of alumina will be saturated at a certain stage by the SOM of the old leachate, the alumina regeneration could be achieved by heating the spent alumina in air at a suitably high temperature to burn the adsorbed deposit an re-utilize it without any special precaution. Precautions are instead needed by the regeneration of the spent activated carbon, to avoid an excessive consumption of it at each regeneration stage.

Especially for the old leachate, the pre-ozonation is desirable to reduce the COD level and to prolong the life of

the activated carbon. In other words, the direct passage of the raw old leachate through an activated carbon bed will accelerate it saturation much more the case of a pre-ozonized leachate, which has already undergone a COD reduction by the ozone treatment.

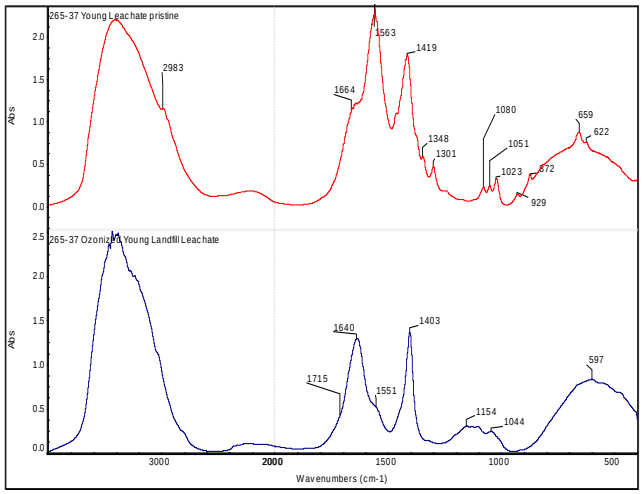

Figure 5. FTIR of pristine SOM from a young leachate (upper trace in red) and after ozonization of the same SOM (lower trace in dark blue).

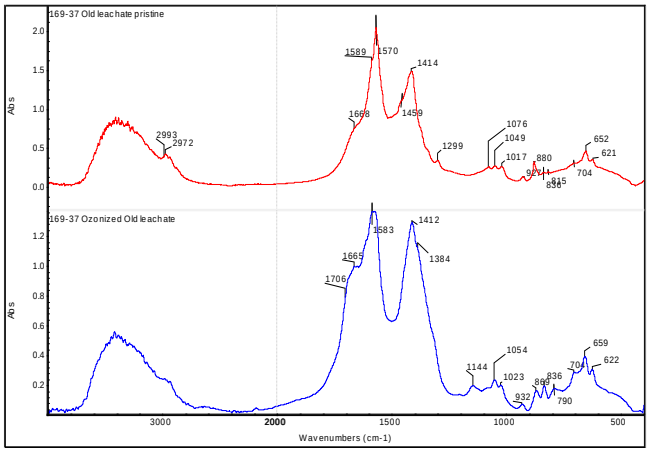

Figure 6. FTIR of pristine SOM from a old leachate (upper trace in red) and after ozonization of the same SOM (lower trace in blue).

Furthermore, the pre-ozonization of the old leachate leads to SOM oxidation as shown by FTIR spectroscopy (Fig.6) and this will be a further aid for the adsorption of the oxidized SOM on the surface oxygen-bearing functional groups present in the activated carbon. Indeed, the patented process[19-21] proposes the passage of the pre-ozonized leachate through a granular activated carbon bed. Norit type activated charcoal was found as one of the activated carbons more effective in the absorption of the pre-ozonized leachate. It is thought that the simultaneous action of ozone and activated carbon on old leachate could further reduce the COD because the free radical mechanism is also activated by the carbon surface.

When a mature leachate having COD = 3135 mg L^{-1} is passed through a column of activated charcoal, the COD drops to 650 mg L^{-1} but the bacterial load remains very high. Furthermore, with such treatment the activated carbon saturates very quickly (see Fig.7). The proposed and patented process[19-21] instead is based on a pre-ozonolysis step which clarifies the leachate and reduces the COD to 2253 mg L^{-1}. The resulting oxidized leachate is easily adsorbed on activated carbon so that the COD drops to 270 mg L^{-1}. As final step, the removal of the residual refractory soluble organic matter and the water sterilization is achieved with a photo-ozonolysis treatment reaching a residual COD of 62 mg L^{-1}, a value well inside the Italian law limits for the discharge in surface waters, in the ground or in the sewage (see Fig. 7).

It is worth reminding here that until the leachate is dark in color the photo-ozonolysis is impossible since the UV light is adsorbed and scattered. It is absolutely necessary, before proceeding with the photo-ozonolysis to clarify the leachate. This task is accomplished by the pre-ozonolysis followed by the passage through an activated carbon bed. The residual COD is finally removed by the combined action of ozone and UV light (photo-ozonolysis). The final photo-ozonolysis stage is also a grant for the sterilization of the treated water.

There are other two main critical points in a landfill leachate: the need to remove the free ammonia content and the necessity to remove the transition metals. As already reported in literature,[1-5] large part of the ammonia can be removed by air bubbling through the leachate. This can be accomplished just before the pre-ozonolysis stage. The pH adjustment of a leachate, especially an old leachate is often necessary in order achieve better results in the pre-ozonolysis stage. In our experience it is better to bring the old leachate pH below 7 and preferably between 5 and 6.

Regarding the transition metals present in the leachate, a complete analysis can be found elsewhere.[6] In our studies on the transition metals removal from the leachate we have monitored essentially the iron and manganese content. Our studies have evidenced that the passage through the activated carbon bed is a very effective tool in the removal of the transition metals bringing their level within the law limits.[19-21] Consequently, the leachate passage through an activated carbon bed after the pre-ozonolysis is a crucial step in this context.

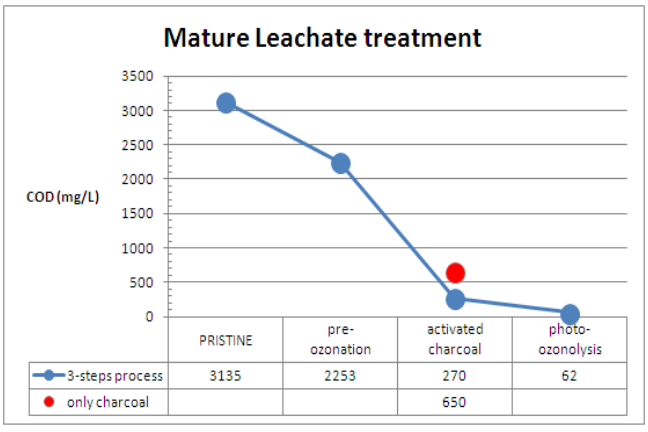

Figure 7. COD changes after the treatment of a mature (old) leachate with the treatment pre-ozonolysis adsorption on activated charcoal and photo-ozonolysis (blue traces). The red bullet shows the COD reduction produced by a straight absorption of the leachate on activated charcoal which however is swiftly saturated in contrast with the pre-ozonolysis leachate treatment which prolongs the life of the activated charcoal.

It is also worth reminding here that ozone is able to oxidize the transition metals to their highest oxidation stage. In general the transition metals at the highest oxidation stage present a much lower solubility in water with respect to their solubility at the lower oxidation stage. Thus, the pre-ozonolysis stage could be considered of key aid in the reduction of the transition metals content in the leachate.

Fig. 1 has shown that a young leachate could be treated with ozone only for the COD removal. However, in Fig. 8 are reported the typical results derived from the train pre-ozonation, passage through a fixed bed of activated carbon and photo-ozonolysis. The results in Fig. 8 are really impressive in the treatment of a young landfill leachate with a starting value of 9200 mg L^{-1}. The direct adsorption of raw young leachate on activated charcoal causes a COD reduction down to 5520 mg L^{-1} and a saturation of the activated charcoal. Instead, the pre-ozonolysis is particularly effective on the young landfill leachate reducing the COD in a single step from 9100 to 1360 mg L^{-1}. The oxidized leachate is then passed through activated charcoal so that the COD is further brought down to 328 mg L^{-1}. The final COD abatement and sterilization is achieved by the photo-ozonolysis step reaching a COD of 107 mg L^{-1}, inside the limits of the Italian law for the discharge in surface waters (see Fig. 8).

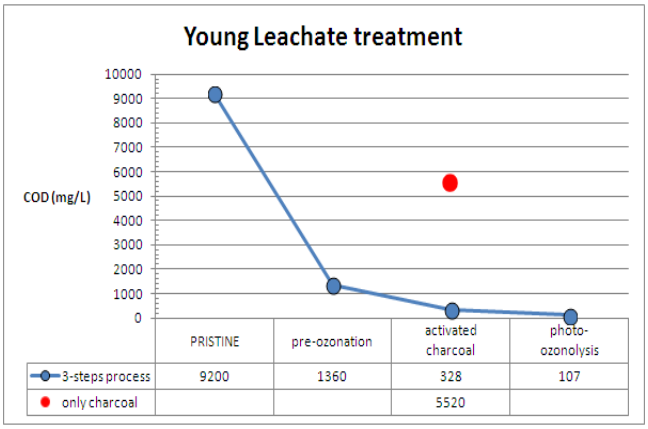

Figure 8. COD changes after the treatment of a young landfill leachate with the sequential treatment pre-ozonolysis adsorption on activated charcoal and photo-ozonolysis (blue traces). The red bullet shows the COD reduction produced by a straight absorption of the leachate on activated charcoal.

Pilot Plant Description

The above (and other) experimental results were translated into patents[19-21] and a pilot plant for the landfill leachate treatment was build. The layout of the pilot plant is shown in Fig. 9. The pilot plant was designed in a modular way so that it is possible to proceed directly and exclusively with the pre-ozonation of the leachate keeping excluded the activated carbon bed and the UV lamps. Afterwards the valves can be arranged in a way that the pre-ozonized leachate passes through the activated carbon bed. It is also possible to ozonize the leachate and inject it directly into the activated carbon column. Finally, the activated carbon column can be excluded and the treated leachate is sent through the UV lamps and continuously charged with the ozone to accomplish the photo-ozonolysis conditions. The installed lamps have a total power of 440 W and the ozone generator is able to produce 50 g O_3 per hour at a flow rate of 16-20 L min^{-1}. The corona discharge ozone generator is coupled with an oxygen generator starting from air and using pressure swing adsorption (PSA) process through a dedicated zeolite bed.

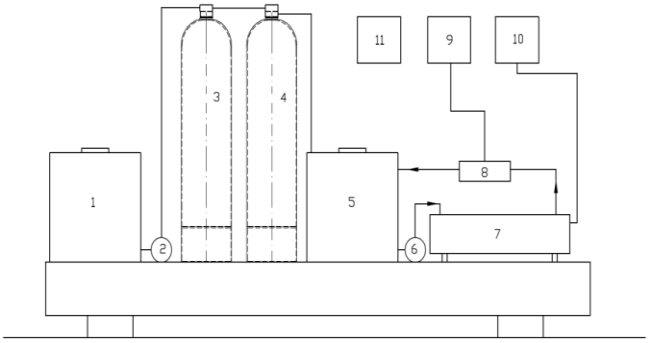

Figure 9. Photo-ozonolysis pilot plant layout. (1) Tank for the pristine leachate, (2) pump, (3) sand filter, (4) activated charcoal column, (5) batch with recirculation reactor, (6) pump, (7) horizontal UV lamps total power 440W, (8) venture injector, (9) ozone generator 50 g/h, water-cooled corona discharge coupled with PSA oxygen generator working at 16-20 L min^{-1} (10) electrical controls for ozonizer and lamps, (11) electrical controls for pumps

Conclusions

The young and old or mature leachate are two completely different wastes not only in terms of COD level, pH, BOD/COD ratio and other analytical chemical parameters but especially on the chemical structure of the soluble organic matter (SOM) present in the leachate. In fact, the SOM isolated from a young leachate is more volatile and oxidizable at the TGA in air than the SOM isolated from an old leachate. This is due not only to significant differences in molecular weight between the two SOM but also to a different degree of chemical structural evolution. In fact, the SOM from young leachate is easily oxidizable and responds well the ozonation with impressive drop in the very high initial COD even with moderate ozone doses. The FT-IR analysis of ozonized SOM from a young leachate versus a reference pristine SOM shows that the ozone attack is directed toward unsaturated ketones and specifically to unsaturated diketones and triketones which present the keto-enol tautomerism phenomenon. Aromatic sites are probably highly alkyl substituted and hence easily degradable by the ozone attack.

On the other hand the old leachate is less sensitive to direct ozonation and the SOM from the old leachate after ozonation shows only limited evidences of oxidation. It was shown that the ozonation of old leachate could be enhanced in terms of COD abatement if conducted in presence of activated alumina. However, the refractory nature toward oxidation by an old leachate becomes immediately evident also in a simple ozonation stage.

Following the patents,[19-21] an effective approach to get rid of the old leachate and to reduce its COD within the law limits involves a pre-ozonation of the leachate followed by a passage through a bed of activated carbon followed in its

turn by a final stage of photo-ozonolysis when the leachate is a clear transparent solution suitable to be irradiated in presence of dissolved ozone. It was shown that with these three stages treatment the law limits for the discharge in sewage or even in surface waters can be achieved.

Since the young leachate is so sensitive to oxidation it is recommended to oxidize it for example by ozone and then treat it with activated charcoal and eventually with photo-ozonolysis in the final stage, at a considerably lower costs than and old, mature leachate.

A pilot plant was designed and build to demonstrate the effectiveness of the proposed process in a larger scale. The pilot plant layout has been disclosed in this paper.

References

[1]Christensen, J. B., Jensen, D. L., Grøn, C., Filip, Z., Christensen, T. H. *Water Res.* **1998**, *32*, 125. https://doi.org/10.1016/S0043-1354(97)00202-9

[2]Kjeldsen, P., Barlaz, M. A., Rooker, A. P., Baun, A., Ledin, A., Christensen, T. H. *Crit. Rev. Environ. Sci. Technol.*, **2002**, *32*, 297-336.https://doi.org/10.1080/10643380290813462

[3]Robinson, H. "The Composition of Leachates from Very Large Landfills: An International Review", *Proceedings of 10th International Waste Management and Landfill Symposium*, S. Margherita di Pula, Cagliari, Italy, October 3–7, **2005**. http://citeseerx.ist.psu.edu/viewdoc/summary?doi=10.1.1.458.4471

[4]Renou, S., Givaudan, J. G., Poulain, S., Dirassouyan, F., Moulin, P. *J. Hazard. Mater.*, **2008**, *150*, 468. https://doi.org/10.1016/j.jhazmat.2007.09.077

[5]Moody, C. M., Townsend, T. G. *Waste Manag.* **2017**, *63*, 267. https://doi.org/10.1016/j.wasman.2016.09.020

[6]Cataldo, F. *J. Radioanal. Nucl. Chem.*, **2012**, *293*, 119. https://doi.org/10.1007/s10967-012-1777-z

[7]Beaman, M. S., Lambert, S. D., Graham, N. J. D., Anderson, R. *Ozone Sci. Engin.* **1998**, *20*, 121. https://doi.org/10.1080/01919519808547281

[8]Haapea, P., Korhonen, S., Tuhkanen, T. *Ozone Sci. Eng.*, **2002**, *24*, 369. https://doi.org/10.1080/01919510208901627

[9]Wang, F., Smith, D. W., El-Din, M. G. *J. Environ. Eng. Sci.*, **2003**, *2*, 413-427. http://www.nrcresearchpress.com/doi/abs/10.1139/s03-058#.W-xKPNThC9I

[10]Orta de Velasquez, M. T., Monje-Ramirez, I. *Ozone Sci. Eng.*, **2006**, *28*, 309. https://doi.org/10.1080/01919510600900241

[11]Cui, Y., Wu, Q., Xiao, S., An, X., Sun, J., Cui, F. *Ozone Sci. Eng.*, **2014**, *36*, 427. https://doi.org/10.1080/01919512.2013.874276

[12]Cui, Y., Zhao, C., Wu, Q., Chen, N., Zhao, J., Bao, L., Sun, J., *Ozone Sci. Eng.*, **2016**, *38*, 367. https://doi.org/10.1080/01919512.2016.1179566

[13]Cataldo, F., Angelini, G. *Ozone Sci. Eng.*, **2013**, *35*, 55. https://doi.org/10.1080/01919512.2012.722045

[14]Amaral-Silva, N., Martins, R. C., Castro-Silva, S.,Quinta-Ferreira, R. M. *J. Environ. Chem. Eng.* **2016**, *4*, 527. https://doi.org/10.1016/j.jece.2015.12.002

[15]Chys, M., Oloibiri, V. A., Audenaert, W. T., Demeestere, K., Van Hulle, S. W. *Chem. Eng. J.* **2015**, *277*, 104. https://doi.org/10.1016/j.cej.2015.04.099

[16]Van Huu, T., Trinh Van, T. *Ozone Sci. Eng.* **2015**, *37*, 22. https://doi.org/10.1080/01919512.2014.940513

[17]Van, T. H., Trinh, T. V. *Ozone Sci. Eng.*, **2016**, *38*, 133. https://doi.org/10.1080/01919512.2015.1112725

[18]Qin, H., Dong, Q., Chen, H., Yang, G., Zhang, X. *Ozone Sci. Eng.* **2015**, *37*, 371. https://doi.org/10.1080/01919512.2015.1006725

[19]Cataldo, F. "Procedimento di purificazione dell'acqua da percolato di discarica," *Italian Patent N° 0001408458* granted on May 9, **2013**. https://patents.google.com/patent/ITRM20110585A1/en

[20]Cataldo, F. "Process for the purification of landfill leachate wastewater by active charcoal and photo-ozonolysis." *U.S. Patent Application No. 2014/0299549 A1*, granted Oct. 9, **2014**. https://patents.google.com/patent/US20140299549A1/en

[21]Cataldo, F., "Purification of landfill leachate wastewater by active charcoal and photo- ozonolysis." *WO2013068308A1*, granted on May 16, **2013**. (see also PCT/EP2012/071794)https://patents.google.com/patent/WO2013068308A1/en

[22]Calace, N., Liberatori, A., Petronio, B. M., Pietroletti, M., *Environ. Pollut.*, **2001**, *113*: 331. https://doi.org/10.1016/S0269-7491(00)00186-X

[23]Chai, X., Takayuki, S., Cao, X., Guo, Q., Zhao, Y. *Chemosphere* **2007**, *69*, 1446. https://doi.org/10.1016/j.chemosphere.2007.04.076

[24]Rodríguez, F. J., Schlenger, P., García-Valverde, M. *Sci. Total Environ.*, **2016**, *541*, 623. https://doi.org/10.1016/j.scitotenv.2015.09.127

[25]Mao, J., Chen, N., Cao, X. *Org. Geochem.* **2011**, *42*, 891. https://doi.org/10.1016/j.orggeochem.2011.03.023

[26]Al-Faiyz, Y. S. *Arabian J. Chem.* **2017**, *10*, S839. https://doi.org/10.1016/j.arabjc.2012.12.018

[27]Cataldo, F., G. Angelini. *J. Radioanal.Nucl. Chem.* **2012**, *293*, 141. https://doi.org/10.1007/s10967-012-1729-7

[28]Cataldo, F., Angelini, G. *Eur. Chem. Bull.*, **2013**, *2*, 592-597. http://dx.doi.org/10.17628/ecb.2013.2.592-597

[29]Colthup, N. B., Daly, L. H., Wiberley, S. E. "*Introduction to Infrared and Raman Spectroscopy*." 3rd edition, Academic Press, San Diego, **1990**.

Received: 15.11.2018.
Accepted: 11.10.2018.

DECARBAMOYLATION OF *N*-ALKOXY-*N*-(4-DIMETHYLAMINOPYRIDIN-1-IUM-1-YL)UREA CHLORIDES IN DIMETHYLSULFOXIDE AS A ROUTE TO 1-ALKOXYAMINO-4-DIMETHYLAMINOPYRIDINIUM CHLORIDES

Vasiliy Georgievich Shtamburg,[a] Victor Vasilievich Shtamburg,[a] Andrey Alexandrovich Anishchenko,[b] Svetlana Vladimirovna Kravchenko,[c] Alexander Vladimirovich Mazepa[d] and Evgeniy Alexandrovich Klots[e]

Keywords: *N*-alkoxy-*N*-(pyridin-1-ium-1-yl)urea chlorides; decarbamoylation; 1-alkoxyamino-4-dimethylaminopyridinium chlorides; structure; O-N-N geminal systems; dimethylsulfoxide.

Decarbamoylation of *N*-alkoxy-*N*-(4-dimethylaminopyridin-1-ium-1-yl)urea chlorides in dimethylsulfoxide takes place with the formation of 1-alkoxyaminopyridinium chlorides. The nature of *N*-alkoxy substituents has a great influence on decarbamoylation efficiency. Decarbamoylation of *N*-*n*-butyloxy-*N*-(4-dimethylaminopyridin-1-ium-1-yl)urea chloride at 20 ºC occurs with the selective formation of 1-*n*-butyloxyamino-4-dimethylaminopyridinium chloride. *N*-Methoxy-*N*-(4-dimethylaminopyridin-1-ium-1-yl)urea chloride is stable in dimethylsulfoxide at 20 ºC, but it forms selectively 1-methoxyamino-4-dimethylaminopyridinium chloride at 82 ºC in 1 h. *N*-Ethoxy-*N*-(4-dimethylaminopyridin-1-ium-1-yl)urea chloride is also stable in dimethylsulfoxide at 20 ºC, but it converts into 1-ethoxyamino-4-dimethylaminopyridinium chloride at 100 ºC under heating for 3 h.

* Corresponding Authors
Fax: +**380**-97-651-61-72
E-Mail: stamburg@gmail.com
[a] *49005 Ukraine, Dnepr, Gagarina st., 8. Ukrainian State University of Chemical Technology*
[b] *49050 Ukraine, Dnepr, Nauchnayast. 25. O. Gonchar Dnepropetrovsk National University*
[c] *49600 Ukraine, Dnepr, Efremovast., 25. Dnipro State Agrarian and Economic University*
[d] *65080 Odessa, Lyustdorfskaya Dorogast., 86. A.V. Bogatsky Physico-Chemical Institute of NAS of Ukraine*
[e] *25006 Ukraine, Kropivnitsky, Shevchenko st., 1. V. Vinnichenko Kirovograd State Pedagogical University*

INTRODUCTION

Five types of 1-alkoxyaminopyridinium salts are known: *N*-alkoxy-*N*-(pyridin-1-ium-1-yl)-*N*-*tert*-alkylamine salts (**1**),[1-3] *N*-alkoxy-*N*-(pyridin-1-ium-1-yl)urea salts (**2**),[3-6] *N*-alkoxy-*N*-(1-pyridinium)carbamate chlorides(**3**),[7] *N*-alkoxy-*N*-(pyridin-1-ium-1-yl)benzamide chlorides(**4**)[3] and unsubstituted 1-alkoxyamino-4-dimethylamino-pyridinium salts **5**[8,9] (Figure 1).

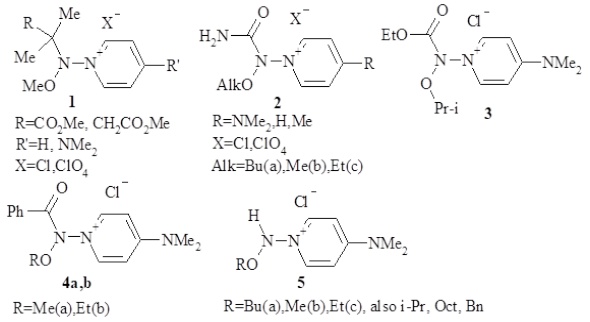

Figure 1. The known types of 1-alkoxyaminopyridinium salts **1-5**

Compounds **1**–**4** were synthesized by the interaction of appropriate *N*-alkoxy-*N*-chloroamines and *N*-alkoxy-*N*-chloroamides with pyridines[1-9] (Figure 2).

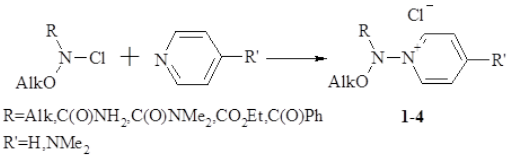

Figure 2. Synthesis of compounds **1** – **4**

1-Alkoxyamino-4-dimethylaminopyridinium salts **5** were synthesized by the reaction of methyl *N*-alkoxy-*N*-chlorocarbamates with 4-dimethylaminopyridine (DMAP).[8,9] Evidently, this reaction carries out via formation of unstable intermediates **3'** (Figure 3).[8]

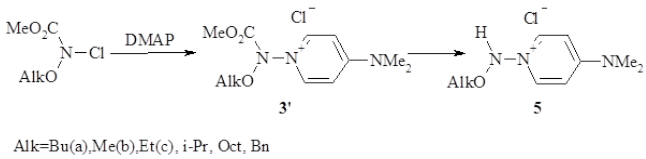

Figure 3. The most convenient synthesis of 1-alkoxyamino-4-dimethylaminopyridinium salts **5**.[8,9]

There are other synthesis methods for preparation of compounds **5,** for example, decarbamoylation of urea derivatives **2** with bases as sodium acetate and ammonia, or potassium fluoride [9]or the reaction of AcONa and benzamide **4a**[9] (Figure 4).

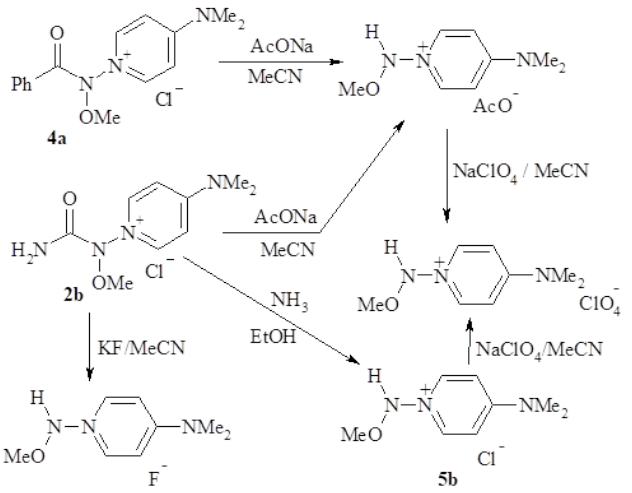

Figure 4. Other synthesis routes of 1-alkoxyaminopyridinium salts (**5**)

1-Alkoxyaminopyridinium salts **1**–**5** are relatively stable compounds contrary to *N*-alkoxy-*N*-aminoamides which are destabilized by $n_{N'} \rightarrow \sigma^*_{N\text{-}O(Alk)}$ orbital interaction ("anomeric effect").[10-13]

Our previous XRD studies confirmed that 4-dimethylamino substituted 1-alkoxyaminopyridinium salts (**1**–**3** and **5**) predominantly exist in their quinonoid form (**B**)[3,6-9] (Figure 5). In pyridinium moiety the N–C(2), the N–C(6), the C(3)–C(4) and the C(4)–C(5) bonds are elongated and the C(2)–C(3) and the C(5)–C(6) bonds are shortened comparably to the same bonds in pyridine and at 4-position unsubstituted 1-alkoxyaminopyridinium salts (**1**,**2**). In compounds **1**–**3** and **5** the C(4)–NMe_2 bond is strongly shortened and is near to the length of a C=N double bond.

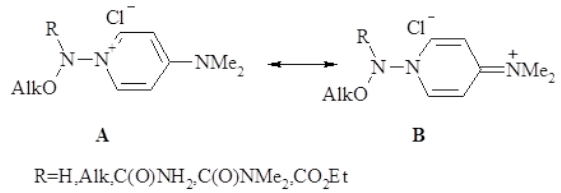

Figure 5. Quinonoid deformation of pyridine ring in 1-alkoxyamino-4-dimethylaminopyridinium salts

EXPERIMENTAL

300 MHz ^{1}H NMR spectra were recorded on a VARIAN VXR-300 spectrometer, 400 MHz ^{1}H NMR spectra were recorded on a VARIAN JEMINI 400 spectrometer with Me_4Si as an internal standard. Mass spectrum was recorded on VG 770-70EQ spectrometer in FAB regime. The solvents were purified and dried according to standard procedures. Dimethylsulfoxide (DMSO) was distilled *in vacuo* at 4 Torr. Benzene was dried by boiling and distillation over Na.

1-*n*-Butyloxyamino-4-dimethylaminopyridinium chloride (5a).

The solution of *N*-*n*-butyloxy-*N*-(4-dimethyl-aminopyridin-1-ium-1-yl)urea chloride[6] **2a** (0.238 mmol, 68.8 mg) in freshly distilled dimethylsulfoxide (1 mL) was kept at 16 °C during 150 h, then dry benzene (13 mL) was added. The benzene-phase was separated; the liquid residue was mixed with benzene (3 mL), then after 20 h the benzene-phase was separated. The obtained residue was dried *in vacuo* at 20 °C (2 Hgmm for 5 h), and then it was extracted by CH_2Cl_2 (8 mL). The CH_2Cl_2-extract was evaporated *in vacuo* giving 1-*n*-butyloxyamino-4-dimethylaminopyridinium chloride **5a** (50.6 mg, 80 %) as a white solid, which was identified by its ^{1}H NMR spectra and mass spectrum.[8]

^{1}H NMR (400 MHz, $CDCl_3$) δ = 0.901 (3H, t, ^3J= 7.4 Hz, $NO(CH_2)_3\underline{Me}$), 1.340 (2H, sex, ^3J=7.4 Hz, $NO(CH_2)_2\underline{CH_2}Me$), 1.573 (2H, quint, ^3J=7.4 Hz, $NOCH_2\underline{CH_2}CH_2Me$), 3.302 (6H, s, NMe_2), 3.807–3.843 (2H, m, $NOCH_2$), 6.877 (2H, d, ^3J=6.8 Hz, C(3,5)H Py), 8.530 (2H, d, ^3J= 6.8 Hz, C(2,6)H Py), 11.556 (1H, NH). ^{1}H NMR (400 MHz, CD_3OD) δ =0.858 (3H, t, ^3J=7.0 Hz, $NO(CH_2)_3\underline{Me}$), 1.293 (2H, sex, ^3J=7.0 Hz, $NO(CH_2)_2\underline{CH_2}Me$), 1.532 (2H, quint, ^3J=7.0 Hz, $NOCH_2\underline{CH_2}CH_2Me$), 3.302 (6H, s, NMe_2), 3.807–3.895 (2H, m, $NOCH_2$), 7.017 (2H, d, ^3J=8.0 Hz, C(3,5)H Py), 8.312 (2H, d, ^3J=8.0 Hz, C(2,6)H Py). ^{1}H NMR (300 MHz, $(CD_3)_2SO$) δ = 0.86 (3H, t, ^3J=7.5 Hz, $NOCH_2CH_2CH_2\underline{Me}$), 1.27 (2H, sex, ^3J=7.5 Hz, $NOCH_2CH_2\underline{CH_2}Me$), 1.51 (2H, quint, ^3J=7.5 Hz, $NOCH_2\underline{CH_2}CH_2Me$), 3.25 (6H, s, NMe_2); 3.79 (2H, t, ^3J=6.3 Hz, $NOCH_2$,); 7.05 (2H, d, ^3J=7.8 Hz, C(3,5)H Py); 8.46 (2H, d, ^3J=7.8 Hz, C(2,6)H Py), 11.00 (s, 1H, NHO). MS (FAB) *m/z* 210 M^+ (100), 152 (6), 137 (32), 123 (73).

b) The solution of *N*-*n*-butyloxy-*N*-(4-dimethyl-aminopyridin-1-ium-1-yl)urea chloride **2a** (0.242 mmol, 69.8 mg) in freshly distilled dimethylsulfoxide (2 mL) was kept at 80 °C for 30 min, then dimethylsulfoxide was distilled off at 70 °C and 2 Torr, then benzene (20 mL) was added to the obtained residue. The reaction mixture was kept under 6 °C for 20 h, and then, the benzene-phase (upper) was separated. The residue was dried at 20°C and 2 Torr for 4h, yielding compound **5a** (62.8 mg, 98%).

1-Methoxyamino-4-dimethylaminopyridinium chloride (5b).

a) The solution of *N*-methoxy-*N*-(4-dimethylaminopyridin-1-ium-1-yl)urea chloride[3,6] (**2b)** (0.361 mmol, 89.0 mg) in freshly distilled dimethylsulfoxide (5 mL) was kept at 82 °C for 1 h, then it was concentrated to a volume of 1 mL at 65–68 °C and 2 Torr. Benzene (20 mL) was added to the residue obtained. The reaction mixture was kept under 6 °C during 20 h, and then, the upper benzene-phase was separated. The lower liquid phase was extracted by benzene (2 mL) again, and the benzene-phase was separated, too. The lower liquid phase was dissolved in CH_2Cl_2 (4 mL), this CH_2Cl_2-solution was added to benzene (16 mL), this mixture was kept at 4 °C for 22 h. The obtained white precipitate was separated, dried *in vacuo* at 15 °C and 3 Torr for 5 h, yielding 1-methoxyamino-4-dimethyl-aminopyridium chloride **(5b)** (51.8 mg, 70 %), as colorless crystals, which were identified by ^{1}H NMR and mass spectra.[8]

^{1}H NMR (300 MHz, $CDCl_3$) δ=3.299 (6H, s, NMe_2), 3.599 (3H, s, NOMe), 6.923 (2H, d, ^3J= 8.1 Hz, C(3,5)H Py), 8.527 (2H, d, ^3J= 8.1 Hz, C(2,6)H Py), 11.669 (1H, NH). ^{1}H NMR (300 MHz, CD_3OD) δ = 3.304 (6H, s, NMe_2), 3.644 (3H, s, NOMe), 7.024 (2H, d, ^3J=8.1 Hz, C(3,5)H Py), 8.305 (2H, d, ^3J=8.1 Hz, C(2,6)H Py). MS (FAB) *m/z* 373 $2M^+ \bullet Cl^-$ (1), 371 $2M^+ \bullet Cl^-$ (4), 168 M^+ (100), 137 (41), 122 (22).

b) The solution of *N*-methoxy-*N*-(4-dimethylaminopyridin-1-ium-1-yl)urea chloride (**2b**) (0.147 mmol, 36.2 mg) in dimethylsulfoxide (2 mL) was kept at 19 °C for 22 h, then DMSO was distilled off at 65–68 °C and 2 Torr, then the obtained residue was washed twice by benzene (10 mL and 3 mL), yielding *N*-methoxy-*N*-(4-dimethyl-aminopyridin-1-ium-1-yl)urea chloride (**1b**) (34.0 mg, 92%) which was identified by its ^{1}H NMR spectrum. ^{1}H NMR (300 MHz, CD_3OD) δ =3.330 (6H, s, NMe_2), 3.892 (3H, s, NOMe), 7.074 (2H, d, ^3J= 6.6 Hz, C(3,5)H Py), 8.292 (2H, d, ^3J= 6.6 Hz, C(2,6)H Py).

Decarbamoylation of *N*-ethoxy-*N*-(4-dimethylaminopyridin-1-ium-1-yl)urea chloride (2c)

a) The solution of *N*-ethoxy-*N*-(4-dimethylaminopyridin-1-ium-1-yl)urea chloride[6] (**2c**) (0.1323 mmol, 34.5 mg) in dimethylsulfoxide (0.6 mL) was kept at 19 °C for 48 h, then benzene (20 mL) was added. The obtained white precipitate was filtered off, washed by benzene (5 ml), dried at 2 Torr, yielding *N*-ethoxy-*N*-(4-dimethylaminopyridin-1-ium-1-yl)-urea chloride (**2c**) (28,0 mg, 81%), which was identified by its ^{1}H NMR spectra. ^{1}H NMR (400 MHz, CD_3OD) δ= 1.313 (3H, t, ^3J=7.0 Hz, $NOCH_2\underline{Me}$), 3.334 (6H, s, NMe_2), 4.107 (2H, q, ^3J=7.0 Hz, $NO\underline{CH_2}Me$), 7.052 (2H, d, ^3J=8.0 Hz, C(3,5)H Py), 8.290 (2H, d, ^3J=8.0 Hz, C(2,6)H Py). ^{1}H NMR (400 MHz, $(CD_3)_2SO$) δ =1.218 (3H, t, ^3J=7.0 Hz, $NOCH_2\underline{Me}$), 3.268 (6H, s, NMe_2), 4.003 (2H, q, ^3J=7.0 Hz, $NO\underline{CH_2}Me$), 7.019 (2H, d, ^3J=7.2 Hz, C(3,5)H Py), 7.790 (1H, br. s, NH), 7.965 (1H, br. s, NH), 8.456 (2H, d, ^3J= 8.0 Hz, C(2,6)H Py).

b) The solution of *N*-ethoxy-*N*-(4-dimethylaminopyridin-1-ium-1-yl)urea chloride (**2c**) (0.1937 mmol, 50.5 mg) in dimethylsulfoxide (3 mL) was kept at 100 °C for 1 h, then DMSO was distilled off at 65 °C and 2 Torr, and benzene (10 mL) was added to the residue. The obtained white precipitate was filtered off, washed by benzene (3 mL), dried at 2 Torr, yielding 46.7 mg of mixture of unconverted *N*-ethoxy-*N*-(4-dimethylaminopyridin-1-ium-1-yl)urea chloride (**2c**) and 1-ethoxyamino-4-dimethylaminopyridinium chloride (**5c**)[8] in molar ratio 85:15 (according to ^{1}H NMR spectrum data).

c) The solution of *N*-ethoxy-*N*-(4-dimethylaminopyridin-1-ium-1-yl)urea chloride (**2c**) (0.2708 mmol, 70.6 mg) in DMSO (4 mL) was kept at 100 °C for 3 h, then DMSO was distilled off *in vacuo*, and purification following the emthdo given above yielded 67.7 mg of mixture of 1-ethoxyamino-4-dimethylaminopyridinium chloride (**5c**)[8] and 4-dimethylaminopyridine hydrochloride (DMAP•HCl) in molar ratio 75:25. ^{1}H NMR of compound **5c** (400 MHz, $(CD_3)_2SO$)δ= 1.120 (3H, t, ^3J=7.0 Hz, $NOCH_2\underline{Me}$), 3.235 (6H, s, NMe_2), 3.819 (2H, q, ^3J=7.0 Hz, $NO\underline{CH_2}Me$), 7.020 (2H, d, ^3J= 8.0 Hz, C(3,5)H Py), 8.432 (2H, d, ^3J= 8.0 Hz, C(2,6)H Py), 10.821 (1H, NHO).

RESULTS AND DISCUSSION

During registration of ^{1}H NMR spectrum of *N*-*n*-butyloxy-*N*-(4-dimethylaminopyridin-1-ium-1-yl)urea chloride (**2a**) in dimethylsulfoxide-d_6, a low field singlet peak appears nearby 11.00 ppm. After keeping the NMR sample in dimethylsulfoxide-d_6 for a longer time, the ^{1}H NMR spectrum of compound **2a** becomes similar to the spectrum of 1-*n*-butyloxyamino-4-dimethylaminopyridinium chloride **5a.** In ^{1}H NMR spectrum of compound **5a, a** low field singlet of NH-proton appears at 11.00 ppm.[8] The further study of **2a** decomposition in dimethylsulfoxide at room temperature during a long time has revealed that decarbamoylation of compound **2a** takes place with the selective forming of 1-*n*-butyloxyamino-4-dimethylaminopyridinium chloride **(5a)** (Figure 6). At 80°C, this reaction finishes in 30 min.

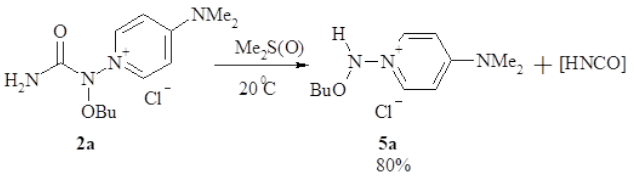

Figure 6. Decarbamoylation of *N*-*n*-butyloxy-*N*-(4-dimethylaminopyridin-1-ium-1-yl)urea chloride **2a** in dimethylsulphoxide

Contrary to the behavior of *N*-n-butyloxy-*N*-(4-dimethylaminopyridin-1-ium-1-yl)urea chloride **2a**, *N*-alkoxy-*N*-(4-dimethylaminopyridin-1-ium-1-yl)ureas salts **2b** and **2c** are stable in dimethylsulfoxide medium at room temperature. Compounds **2b** and **2c** could be recovered in unchanged form after keeping them in DMSO at room temperature. However, *N*-methoxy-*N*-(4-dimethylaminopyridin-1-ium-1-yl)urea chloride **2b,** has been converted in DMSO in 1-methoxy-4-dimethylaminopyridinium chloride (**5b**) on heating at 82 °C for 1 h (Figure 7).

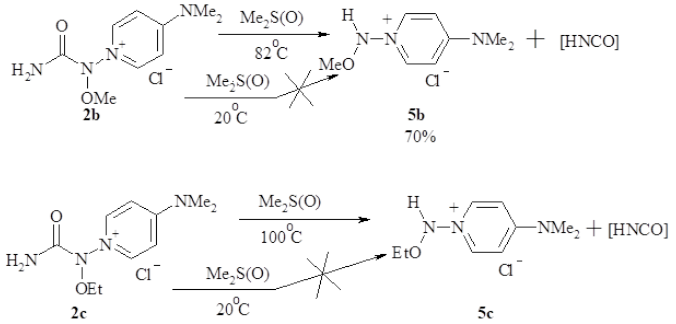

Figure 7. Decarbamoylation of *N*-alkoxy-*N*-(4-dimethylaminopyridin-1-ium-1-yl)ureas chlorides **2b**,**c** in dimethylsulfoxide

N-Ethoxy-*N*-(4-dimethylaminopyridin-1-ium-1-yl)urea chloride **2c** is more stable to decarbamoylation in DMSO solution.

Decarbamoylation of compound **2c** at6 82 °C occured very slow. Heating at 100 ºC for1 h with further DMSO removing yielded the mixture of compounds **2c** and **5c** in molar ratio 85:15. The heating of compound **2c** solution in DMSO at 100 ºC for 3 h yielded the mixture of compound **5c** and 4-dimethylaminopyridine hydrochloride (DMAP•HCl) in the molar ratio 3:1, the precursor **2c** was absent. Apparently, in this case, after the overall conversion of urea **2c**, the particular decomposition of product **5c** may be occurred.

Unfortunately, in our case, the mechanism of decarbamoylation of *N*-alkoxy-*N*-(4-dimethylaminopyridin-1-ium-1-yl)ureas salts (**2**) in the presence of base[9] is not known. It may be supposed, that dimethylsulfoxide as a weak base facilitates proton elimination at high temperatures (Figure 8).

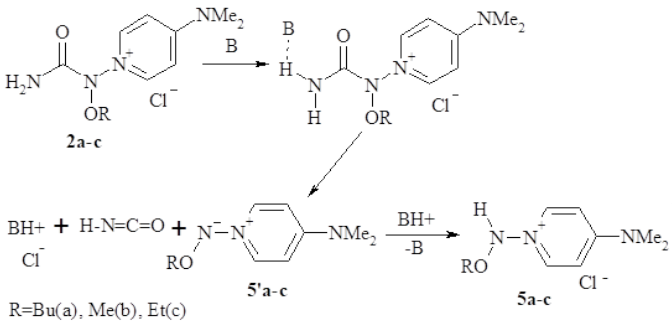

Figure 8. The possible mechanism of decarbamoylayion of ureas **2** by action base(AcO^-, F^-, NH_3) and DMSO

It is probable, that the differences of *N*-alkoxy-*N*-(4-dimethylaminopyridin-1-ium-1-yl)urea chlorides (**2**) activity in the decarbamoylation processes may be caused by the different degree of pyramidality of the central nitrogen atom of O–N–N^+ geminal system. As it is known for compounds containing (R)O–N–O(Ac) geminal systems, the growth of pyramidality of central nitrogen atom facilitates to increasing of action of $n_{O(R)} \rightarrow \sigma^*_{N-O(Ac)}$ anomeric effect thus causes of N–O(Ac) bond weakening.[10-13]

The pyramidality of the central nitrogen atom of O–N–O geminal systems of *N*-(4-chlorbenzoyloxy)-*N*-alkoxyureas (**6a** and **6b**, R= Bu^nO(**a**), EtO (**b**)) (Figure 9) depends on the nature of *N*-alkoxy moiety.[14] In *N*-4-chlorbenzoyloxy-*N*-*n*-butyloxyurea **6a**, the pyramidality of the central nitrogen atom is such as great (sum of bond angles is 323.8º) [5], as that was found in *N*-4-chlorbenzoyloxy-*N*-etoxyurea **6b** (sum of bond angles is 329.3º).[14]

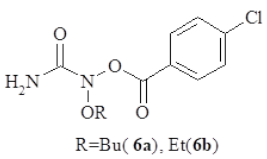

Figure 9. The family of *N*-4-chlorbenzoyloxy-*N*-alkoxyureas **6a**,**b**[5,14]

A similar influence of the nature of *N*-alkoxy substituent on the reactivity was found for the isopropanolysis of *N*-acetoxy-*N*-alkoxyureas **7a** and 7**b** (*N*-alkoxy group = Bu^nO (**a**), MeO(**b**)).[15] In isopropanol, *N*-acetoxy-*N*-*n*-butyloxyurea **7a** selectively forms *N*-*n*-butyloxy-*N*-isopropyloxyurea **8** at room temperature (Figure 10). At the same time, *N*-acetoxy-*N*-methoxyurea **7b** is stable towards isopropanolysis at room temperature. It was proposed[15] that the nitrogen pyramidality degree in *N*-acetoxy-*N*-*n*-butyloxyurea **7a** was higher than that in *N*-acetoxy-*N*-methoxyurea **7b** due to the influence of *N*-*n*-butyloxy moiety. Probably, this phenomenon facilitates the action of $n_{O(Bu)} \rightarrow \sigma^*_{N-OAc}$ anomeric effect and the more weakening of N−OAc bond. [15]

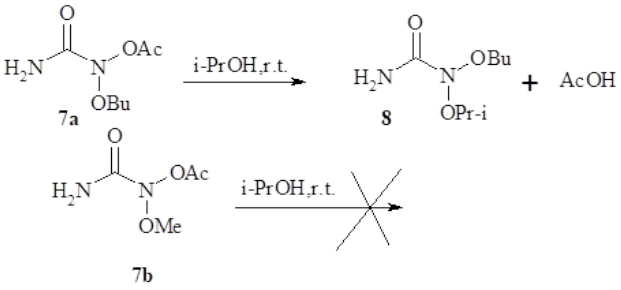

Figure 10. Isopropanolysis of *N*-acetoxy-*N*-alkoxyureas**7a**,**b** at room temperatures[15]

It may be proposed that similarly to *N*-alkoxy-*N*-(4-dimethylaminopyridin-1-ium-1-yl)urea salts (**2a-c),** compound **2a** has the largest nitrogen pyramidality degree which remains during forming intermediate **5a'** (Figure 8). Respectively, intermediate **5a'** may be more stable than intermediates **5b'** and **5c'**. It might cause the higher reactivity of *N*-*n*-butyloxyurea **2a** comparing to *N*-methoxyurea **2b** and *N*-ethoxyurea **2c**. But the structure parameters are known only for compound **2b,**[3] and further XRD study of the structure of compounds **2a** and **2c** is needed for correct mechanism proposition.

Conclusions

Decarbamoylation of *N*-alkoxy-*N*-(4-dimethylamino-pyridin-1-ium-1-yl)ureas chlorides in dimethylsulfoxide occurs with the formation of 1-alkoxyamino-4-dimethylaminopyridinium chlorides. The nature of *N*-alkoxy substituent's has a significant influence on easyness of the decarbamoylation reaction.

References

[1]Shtamburg, V.G., Rudchenko, V.F., Nasibov, Sh.S., Chervin, I.I., Pleshkova, A.P., Kostyanovsky, R.G., Geminal Systems. 16. Reactions of N-Chloro-N-alkoxy-N-alkylamines with Amines, *Bull.Acad.Sci.USSR.Div.Chem.Sci.*, **1981**, *30(10)*, 1914−1920. https://doi.org/10.1007/BF00963422

[2]Shtamburg, V.G., Tsygankov, A.V., Klots,E.A., Fedyanin, I.V., Lyssenko,vK.A., Kostyanovsky,vR.G.,N,N-Dimethoxy-N-tert.-alkylamines: New Synthesis Methods and Crystal Structure of Precursor, *Mendeleev Commun.*,**2006**,*16(2)*, 84–85.https://doi.org/10.1070/MC2006v016n02ABEH002222

[3]Shtamburg, V.G., Tsygankov, A.V., Shishkin, O.V., Zubatyuk, R. I., Shtamburg, V. V., Gerasimenko, M. V., Mazepa, A. V.,

Kostyanovsky, R. G., 1-Alkoxyamino-4-dimethylaminopyridinium derivatives as new representatives of O-N-N$^+$germinal systems and their structure, *Mendeleev Commun*., **2012**, *22(2)*, 92−94. https://doi.org/10.1016/j.men.com.2012.02.014

[4]Rudchenko, V.F., Shevchenko, V.I., Kostyanovsky, R. G., Geminal systems. Communication 29. A reaction of N-Chloro-N-methoxy-N',N'-dimethylurea with N-Nucleophiles, *Bull.Acad.Sci.USSR. Div.Chem.Sci.*, **1986**, *35(3)*,551–554.https://doi.org/10.1007/BF00953223

[5]Shtamburg, V.G., Shishkin, O.V., Zubatyuk, R.I., Kravchenko, S.V., Shtamburg,V.V., Distanov, V.B., Tsygankov, A.V., Kostyanovsky, R.G., Synthesis ,structure and properties of N-alkoxy-N-(1-pyridinium)urea salts, N-alkoxy-N-acyloxyureas and N,N-dialkoxyureas, *Mendeleev Commun*.,**2007**,*17(3)*, 178–180.https://doi.org/10.1016/j.men.com.2007.05.016

[6]Shtamburg, V.G., Shtamburg, V.V., Tsygankov, A.V., Anishchenko, A.A., Zubatyuk, R.I., Shishkina, S.V., Mazepa, A.V., Klots, E.A., Synthesis and Structure of New *N*-Alkoxy-*N*-(1-pyridinium)urea Chlorides, *Eur. Chem. Bull*.,**2016**,*5(4)*,142–146. https://doi.org/10.17628/BCB.2016.5.142

[7]Shtamburg, V.G., Anishchenko, A.A., Shishkina,S.V., Konovalova, I.S., Shtamburg, V.V., ., Mazepa, A.V., Kravchenko, S.V., 1-(N-Ethoxycarbonyl-N-isopropyloxy)amino-dimethylaminopyridinium Chloride. Synthesis and Structure, *Eur. Chem. Bull*.,**2017**,*6(10)*,470–474.https://doi.org/10.17628/ecb.2017.6.470-474

[8]Shtamburg, V.G., Shishkina, S.V., Shtamburg, V.V., Mazepa, A.V., Kadorkina, G.K., Kostyanovsky, R.G., 1-Alkoxyamino-4-dimethylaminopyridiniun Salts: Synthesis and Structure, *MendeleevCommun*.,**2016**,*26(2)*, 169–171.https://doi.org/10.1016/j.men.com.2016.03.030

[9]Shtamburg, V. G., Shtamburg, V. V., Kravchenko, S. V., Mazepa, A. V., Anishchenko, A. A., Posokhov, E. A., A New Synthesis of N-Alkoxyaminopyridinium Salts, *Bulletin of National University "KhPI". Series: New solutions in modern technology*,**2017**, *N 7*, 211−218. https://doi.org/10.20998/2413−4295.2017.07.30

[10]Glover, S.A., Anomeric Amides – Structure, Properties and Reactivity, *Tetrahedron*, **1998**, *54(26)*, 7229−7271. https://doi.org/10.1016/S0040-4020(98)00197-5

[11]Glover, S. A., Chapter 18. N-Heteroatom-substituted hydroxamic esters, in *The Chemistry of Hydroxylamines, Oximes and Hydroxamic Acids*, Eds Rappoport, Z., Liebman, J. F., John Wiley and Sons, New York. **2009**, 839–923. https://doi.org/10.1002/9780470741962ch18

[12]Glover, S.A., Rauk, A., Conformational Stereochemistry of the HERON Amide, *N*-Methoxy-*N*-dimethylaminoformamide: A Theoretical Study, *J. Org. Chem.*, **1999**, *64(7)*, 2340–2345. https://doi.org/10.1021/jo982048p

[13]Glover, S. A., White, J. M., Rosser, A. A., Digianantonio, K. M.. Structure of N,N-Dialkoxyamides: Pyramidal Anomeric Amides with Low Amidicity, *J. Org. Chem.*, **2011**, *76*, 9757−9763. https://doi.org/10.1021/jo201856u

[14]Shishkin, O.V., Shtamburg, V.G., Zubatyuk, R.I., Olefir, D.A., Tsygankov, A.V., Prosyanik, A.V., Mazepa, A.V., Kostyanovsky, R.G., Chiral Ureas with Two Electronegative Substituens at 1-*N* and Unusual Case of Coexisting a Pyramidal and Almost Planar 1-*N* in The Same Crystal, *Chirality*, **2009**, *21(7)*, 642–647. https://doi.org/10.1002/chir.20668

[15]Shtamburg, V.G., Kostyanovsky, R.G., Tsygankov, A.V., Shtamburg, V.V., Shishkin, O.V., Zubatyuk, R.I., Mazepa, A.V., Kravchenko, S.V., Geminal Systems. Communication 64. *N*-Alkoxy-*N*-chloroureas and *N*,*N*-Dialkoxyureas, *Russ. Chem. Bulletin. Intern. Ed.* ,**2015**, *64(1)*, 62–75. https://doi.org/10.1007/s11172-015-0822-9

Received: 24.10.2018.
Accepted: 13.12.2018.